2015

Functional silica-encapsulated photoactive nanocrystals

Chia-Cheng Lin
Iowa State University

Recommended Citation

Lin, Chia-Cheng, "Functional silica-encapsulated photoactive nanocrystals" (2015). *Graduate Theses and Dissertations*. 14409.
https://lib.dr.iastate.edu/etd/14409

Functional silica-encapsulated photoactive nanocrystals

by

Chia-Cheng Lin

A dissertation submitted to the graduate faculty

in partial fulfillment of the requirements for the degree of

DOCTOR OF PHILOSOPHY

Major: Chemistry

Program of Study Committee:

Javier Vela, Major Professor
Gordon Miller
Keith Woo
Ning Fang
Wenyu Huang

Iowa State University

Ames, Iowa

2015

TABLE OF CONTENTS

Page

CHAPTER 2 MICROSTRUCTURE EFFECTS ON THE WATER OXIDATION ACTIVITY OF Co_3O_4/POROUS SILICA NANOCOMPOSITES

CHAPTER 3 METAL OXIDE DEOXYSILYLATION: A GENERALIZED ROUTE FOR THE SINGLE POT SYNTHESIS AND ENCAPSULATION OF CHALCOGENIDE AND PNICTIDE NANOCRYSTALS

CHAPTER 4 MULTISHELL Au/Ag/SiO_2 NANORODS WITH TUNABLE OPTICAL PROPERTIES AS SINGLE PARTICLE ORIENTATION AND ROTATIONAL TRACKING PROBES

ACKNOWLEDGMENTS

This is a long and delightful journey. When it comes to the end, it is time to part away. I truly believe I could not complete this task without the company and assistance from people during the past five years. I would like to express my sincere gratitude to these people.

First, I want to thank my research advisor, Prof. Javier Vela, for his support and guidance. Under his instruction, I learned how to be a good chemist. I would also like to thank my committee members, Prof. Gordon Miller, Prof. Keith Woo, Prof. Ning Fang and Prof. Wenyu Huang for all the helpful and valuable suggestions. Equally importantly, I want to thank all the Vela group members for your company. I would also like to thank all my friends. With you, life in Ames is always interesting. Last, but not the least, I want to thank my family. Without their support, I could not accomplish this.

ABSTRACT

Silica-based nanocomposites with core/shell configurations have diverse functionalities and applications. We present the preparation and characterization of Co_3O_4/porous-SiO_2 nanocomposites with the examination of their catalytic activity in the dye sensitized water oxidation reaction; a generalized methodology to prepare metal chalcogenides/pnictides with one-pot and one-step manner; the synthesis of Au/Ag/SiO_2 multishell nanorods and their application as imaging probes in single particle tracking experiments.

Silica supported Co_3O_4 nanocomposites have recently drawn much attention due to their high catalytic ability in the water oxidation reaction. We have synthesized several Co_3O_4/porous silica nanocomposites to study the synergetic effects of the catalyst microstructure and local environment on water oxidation catalytic activity. The catalytic activity study of Co_3O_4/porous SiO_2 core/shell nanoparticles on oxygen evolution reaction reveals that the catalyst with a 19.8 ± 1.4 nm shell has superior activity than other catalysts due to two possible factors: the increased local concentration of $Ru(bpy)_3^{2+}$ near the active Co_3O_4 and/or the reduced reorganization energy due to the lower dielectric constant. However, further increasing shell thicknesses resulted in the deterioration of catalytic activity possibly due to slower diffusion of reactants. In the Co_3O_4/SBA-15 system, the unmodified sample is more active than the modified ones. This is could be due to local surface permittivities of surface-modified composites (e.g., −SiPh and $-SiMe_3$) being lower than those of the unmodified composites. Additionally, the loss of possible $Ru(bpy)_3^{2+}$ binding sites and pore blocking after surface modification may cause the loss of reactivity.

Late transition metal chalcogenides and pnictides are popular materials for their unique physical properties and various applications, such as hydroprocessing and water electrolysis catalysts. We demonstrate a generalized route using trimethylsilyl reagents (TMS_xE) to convert metal oxides into metal chalcogenides and pnictides through deoxysilylation reactions. The resulting nanocrystals are hollow (vesicle-like) and are surrounded by amorphous silica layer. The nonequivalent diffusion of ions induces the void formation inside the nanocrystals (nanoscale Kirkendall effect); simultaneous decomposition of the TMS_xE produces silica layers that can serve as the protection layer preventing particle agglomeration and thus increasing both the robustness and thermal stability of the composites.

Plasmonic metal nanocrystals are a type of label/probe in optical applications, such as bioimaging labels, biochemical sensors, photothermal therapy, surface enhanced Raman spectroscopy and surface plasmon enhanced solar cells. Single particle orientation and rotational tracking (SPORT) is one of the techniques that can explicit the biophysics in biological systems. We present the fabrication of $Au/Ag/SiO_2$ nanorods with well-controlled size, composition and shape for SPORT experiments. With the enhancement of the longitudinal dipolar LSPR due to the secondary silver coating, these multishell nanorods are able to provide sufficient sensitivity for detection at temporal resolution in millisecond range on both synthetic lipid bilayers and live cell membranes.

CHAPTER 1.

GENERAL INTRODUCTION

Silica-based core/shell nanocomposites

This thesis describes the preparation and utilization of several nanocrystal-core/silica -shell nanocomposites and a general methodology to synthesize nanoscale metal chalcogenides/pnictides. Silica coating on inorganic and organic nanomaterials can enhance the colloidal stability, lower the intrinsic toxicity (better biocompatibility), prevent particle aggregation, and increase the versatility and functionality.[1] Silica possesses several properties which make it a good candidate for synthesizing functional nanocomposites.[2] 1) The surface chemistry of silica is well studied, and the modification of the surface can be obtained by post-treatment (grafting) with functional silanes. 2) The relatively low van der Waal interactions and the strong affinity between positively charged species and the silica surface (isoelectric point ~ 2) provide both steric and electrostatic protection in aqueous solution. 3) Silica is transparent in the ultraviolent, visible and infrared regions, which allows the use of silica in optical applications. 4) Silica will not interfere with magnetic or electric fields. 5) Silica materials are relatively chemically inert and economically affordable.

Taking advantaging of these above listed properties, silica-based nanocomposites with core-shell geometry have been developed for several applications, including silica encapsulated magnetic particles as magnetic resonance imaging (MRI) contrast agents,[3] silica coated plasmonic nanocrystals in photothermal therapy and imaging in biological systems,[4] fluorescent dyes embedded in solid silica spheres as biomedical probes,[1] mesoporous silica nanoparticles as drug delivery cargos,[5] and porous silica coated metal nanoparticles for catalytic reactions at higher temperature.[6] Chapters 2, 3 and 4 demonstrate the preparation and utilization of Co_3O_4/SiO_2 in the water oxidation reaction, preparation of metal chalcogenides/pnictides via deoxysilylation and $AuAg/SiO_2$ in bioimaging applications respectively.

Co_3O_4 in photocatalytic water oxidation

The search for an alternate energy source to replace fossil fuels is of urgent demand. Solar to chemical energy conversion is one of the promising candidates for its advantages, such as less exhaust emission (compared to green house gas emission from consumption of fossil fuels), abundance and renewability. Among these solar to chemical energy conversions, photochemical water splitting is one way to produce hydrogen, which is a potentially valuable and clean fuel. However, water oxidation remains the biggest obstacle in the water splitting reaction because of the involvement of the four electron transfer and the formation of oxygen−oxygen bonds.

Efforts have been dedicated to develop efficient and economic water oxidation catalysts. For example, WO_3,[7] cobalt-phosphate (Co-Pi) combined α-Fe_2O_3,[8] ZnO and WO_3,[9] and polymorphs of manganese oxides [10] show enhanced stability and catalytic ability. Co_3O_4-modified Ta_3N_5 photoanodes demonstrate enhanced performance and stability. [11] Hard-templating mesoporous Co_3O_4 nanoparticles reveals increased stability and electrocatalytic ability. [12] Co(II)-modified, fluorine-doped tin oxide, as well as self-repairing cobalt phosphate films and diamond supported Co_2O_3 nanoparticles, [13] are highly active. Besides the aforementioned catalysts, various metal oxide-based photocatalytic systems, which require the employment of $[Ru(bpy)_3]^{2+}$ complex and $S_2O_8^{2-}$ as photosensitizer and sacrificial electron acceptor respectively, have been investigated, such as mesoporous silica supported Mn_3O_4, [14] colloidal IrO_2, [15] manganese oxide nanostructures, [16] and ternary metal oxides.[17] In addition to heterogeneous catalysts, several homogeneous cobalt-based molecular water oxidation catalysts have been developed.[18]

Recently, mesoporous silica supported Co_3O_4 nanoparticles have drawn much attention for their high catalytic activity on water oxidation.[19] Both the effect of the Co_3O_4 nanocrystal shapes, and the support have been investigated.[20] Co_3O_4/SBA-15 catalysts demonstrate higher activity than Co_3O_4/MCM41 catalysts due to their larger pore size, and three dimensionally connecting pore structures results in better performance. Doping Co_3O_4 with Mn can lead to better performance than just pure Co_3O_4. Grafting cobalt complexes onto SBA-15, zeolite-supported cobalt oxides (CoO_x), and Co_3O_4 particles with hollow morphology have also been developed. Beside the structural and morphological effects, the hole transport mechanism from $[Ru(bpy)_3]^{2+}$ to the surface of Co_3O_4 was studied in a Co_3O_4/SiO_2 core/shell system with hole conductive organic molecules embedded in the silica shell. Chapter 2 presents the microstructure effects of the Co_3O_4/porous-SiO_2 on water oxidation reaction.

Transition metal chacolgenide/pnictide silica nanocomposites

Transition metal chalcogenide and pnictide nanomaterials have draw much attention recently for their physical properties and interesting applications, such as hydroprocess catalysts (e.g. hydrodesulfurization, HDS, hydrodeoxygenation, HDO and hydrodenitrification, HDN, of oils), battery materials, biomass conversion and electrochemical catalysts.[21,22] Metal phosphides especially show excellent performance in HDS and HDN, with the most active Ni_2P catalyst competing with current industrially used Ni-Mo-S based-catalysts.[23] In addition to excellent hydrotreating catalytic properties, transition metal phosphides and chalcogenides are active catalysts for water electrolysis. For instance, FeS_2, $CoSe_2$, Co_9S_8, MoS_2, CoP and Ni_2P demonstrate improved performance in electrochemical hydrogen evolution reaction.[24]

Efforts have been dedicated to developing new synthetic methodologies that can produce nanoscale metal chalcogenides and pnictides with controllable size, shape and morphology in order to completely investigate and exploit metal chalcogenides and pnictides. Transition metal phosphide and chalcogenide nanomaterials are conventionally prepared by chemical vapor deposition, reduction of metal precursors, colloidal synthesis. Treating pre-formed metals/metal oxides with elemental sulfur/phosphorus or alkyl sulfides/phosphines also yields metal sulfides or metal phosphides.[25-29] In order to increase their stability and recyclability, these catalysts are subsequently immobilized onto high surface area solid supports (e.g. porous silica) to enhance their stability and recyclability.[30] We thus utilize highly reactive trimethylsilyl precursors (TMS_xE) as chalcogen or pnictogen sources and oxygen scavengers to react with pre-made metal oxide nanocrystals. Chapter 3 covers the synthesis of metal phosphide and chalcogenide nanocrystals surrounded by a simultaneously formed silica layer in a one-pot and one-step manner.

Plasmonic nanocrystals in single particle orientation and rotational tracking (SPORT)

Surface plasmon resonance, which is the coherent and collective oscillation of free electrons in the conduction band, causes the interesting tunable optical properties observed on noble metal nanocrystals, e.g. copper, silver and gold.[31] As revealed by Mie theory, when these noble metal nanocrystals are much smaller than the wavelength of light, they intensely absorb and scatter light. These two surface plasmon enhanced optical properties mainly depend on the composition, shape, size and the dielectric of the surrounding environment. The strong and tunable light absorption, combined with their scattering ability enables noble metal nanocrystals to be a new type of labels/probes in optical applications, including bioimaging labels, biochemical sensors, photothermal therapy,[32] surface enhanced Raman spectroscopy,[33] surface plasmon enhanced solar cells,[34] optical switches and lithography.[35]

Single particle tracking (SPT) is conventionally utilized to study biophysical phenomena by tracing the two-dimensional and three-dimensional movement of the probe molecules.[36,37] Plamonic nanocrystals are of interest for their strong light absorption and scattering nature. Anisotropic plasmonic metal nanocrystals are especially important because they can provide extra orientation and rotational information, which are essential in investigating biophysical mechanisms such as DNA polymerization and molecular motors.[38,39] Gold nanorods (AuNRs) have been employed extensively for rotational tracing and orientation sensing owing to their relatively high photostability, high biocompatibility, and the surface plamon enhanced absorption and scattering. A previously reported study reveals that the orientation and rotational information of AuNRs can be resolved under a differential interference contrast microscopy (DIC), and one can further use AuNRs to study various biophysical mechanisms. Chapter 4 presents gold/silver/silica multishell nanocomposites and their application in SPORT.

Thesis Organization

This thesis consists of five chapters. Chapter 1 is an overview of the core/shell type silica-based nanocomposites, including synthesis, properties and applications. Chapters 2 – 4 are journal articles. Chapter 2 has been published; Chapter 3 is in preparation and Chapter 4 is submitted. Chapter 5 gives the general conclusion of this work.

Chapter 2 was published in *ACS Catal.* in 2015 titled “*Microstructure Effects on the Water Oxidation Activity Of Co_3O_4/Porous Silica Nanocomposites.*” Chapter 2 illustrates how the microstructures of the Co_3O_4/SiO_2 composites influence the catalytic performance on water oxidation reaction.

Chapter 3 is a manuscript in preparation, titled “*Metal Oxide Deoxysilylation: A Generalized Route for the Single Pot Synthesis and Encapsulation of Chalcogenide and Pnictide Nanocrystals.*” Chapter 3 demonstrates a generalized method to prepare metal chacolgenide and metal pnictide nanocrystals by reacting premade metal oxides with trimethylsilyl reagents through deoxysilylation reaction.

Chapter 4 is a collaboration paper submitted to *Anal. Chem.* in 2015 titled “*Multishell Au/Ag/SiO_2 Nanorods with Tunable Optical Properties as Single Particle Orientation and Rotational Tracking (SPORT) Probes*” with Kuangcai Chen of Prof. Fang’s research group. Chapter 4 reports the preparation of multishell Au/Ag/SiO2 nanorods, and the utilization of the nanocomposites in single particle orientation and rotational tracking (SPORT) on both synthetic lipid bilayers and live cell membranes.

References

(1) Vivero-Escoto, J. L.; Huxford-Phillips, R. C.; Lin, W. *Chem. Soc. Rev*. 2012, *41*, 2673–2685.

(2) Guerrero-Martínez, A.; Pérez-Juste, J.; Liz-Marzán, L. M. *Adv.Mater*. **2010**, *22*, 1182–1195.

(3) Na, H. B., Song, I. C. and Hyeon, T. *Adv. Mater*. **2009**, *21*, 2133–2148.

(4) Zhang, Z.; Wang, L.; Wang, J.; Jiang, X.; Li, X.; Hu, Z.; Ji, Y.; Wu, X.; Chen, C. *Adv. Mater*. **2012**, *24*, 1418–1423.

(5) Slowing, I. I., Vivero-Escoto, J. L., Wu, C.-W. Lin, V. S. Y. *Adv. Drug Delivery Rev*. **2008**, *60*, 1278–1288.

(6) Joo, S. H., Park, J. Y., Tsung, C. K., Yamada, Y., Yang, P. D., Somorjai, G. A. *Nat. Mater*. **2009**, *8*, 126–131.

(7) Wang, H. L.; Lindgren, T.; He, J. J.; Hagfeldt, A.; Lindquist, S. E. *J. Phys. Chem. B* **2000**,*104*, 5686–5696.

(8) Sivula, K.; Formal, F. L.; Grätzel, M. *Chem. Mater.* **2009**, 21, 2862–2867.

(9) Ni, M.; Leung, M. K. H.; Leung, D. Y. C.; Sumathy, K. *Renewable Sustainable Energy Rev*. **2007**, *11*, 401–425.

(10) Robinson, D. M.; Go, Y. B.; Mui, M.; Gardner, G.; Zhang, Z.; Mastrogiovanni, D.; Garfunkel,E.; Li, J.; Greenblatt, M.; Dismukes, G. C. *J. Am. Chem. Soc*. **2013**, *135*, 3494–3501.

(11) Hou, J.; Wang, Z.; Yang, C.; Cheng, H.; Jiao, S.; Zhu, H. *Energy. Environ. Sci.* **2013**, *6*, 3322–3330.

(12) Tüysüz, H.; Hwang, Y.; Khan, S.; Asiri, A.; Yang, P. *Nano Res.* **2013**, *6*, 47–54.

(13) Wee, T. L.; Sherman, B. D.; Gust, D.; Moore, A. L.; Moore, T. A.; Liu, Y.; Scaiano, J. C. *J. Am. Chem. Soc.* **2011**, *133*, 16742–16745.

(14) Jiao, F. and Frei, H. *Chem. Commun.* **2010**, 46, 2920–2922.

(15) Hara, M.; Waraksa, C. C.; Lean, J. T.; Lewis, B. A.; Mallouk, T. E. *J. Phys. Chem. A* **2000**, *104*, 5275–5280.

(16) Hocking, R. K.; Brimblecombe, R.; Chang, L.-Y.; Singh, A.; Cheah, M. H.; Glover, C.; Casey, W. H.; Spiccia, L. *Nat. Chem.* **2011**, *3*, 461– 466.

(17) Hong, D.; Yamada, Y.; Nagatomi, T.; Takai, Y.; Fukuzumi, S. *J. Am. Chem. Soc.* **2012**, *134*, 19572–19575.

(18) Yin, Q.; Tan, J. M.; Besson, C.; Geletii, Y. V.; Musaev, D. G.; Kuznetsov, A. E.; Luo, Z.; Hardcastle, K. I.; Hill, C. L. *Science* **2010**, *328*, 342–345.

(19) Jiao, F.; Frei, H. *Angew. Chem., Int. Ed.* **2009**, *48*, 1841–1844.

(20) Grzelczak, M.; Zhang, J.; Pfrommer, J.; Hartmann, J.; Driess, M.; Antonietti, M.; Wang, X.*ACS Catal.* **2013**, 3, 383–388.

(21) Carenco, S.; Portehault, D.; Boissière, C.; Mézailles, N.; Sanchez, C. Nanoscaled Metal Borides and Phosphides: Recent Developments and Perspectives. *Chem. Rev.* **2013**, *113*, 7981−8065.

(22) Popczun, E. J.; McKone, J. R.; Read, C. G.; Biacchi, A. J.; Wiltrout, A. M.; Lewis, N. S.; Schaak, R. E. *J. Am. Chem. Soc.* **2013**, *135*, 9267−9270

(23) Prins, R.; Bussell, M. E. Metal Phosphides: Preparation, Characterization and Catalytic Reactivity. *Catal. Lett.* **2012**, *142*, 1413−1436.

(24) Lai, C.-H.; Lu, M.-Y.; Chen, L.-J. *J. Mater. Chem.* **2012**, *22*, 19–30.

(25) Panneerselvam, A.; Malik, M., A; Afzaal, M.; O'Brien, P.; Helliwell, M. *J. Am. Chem. Soc.* **2008**, *130*, 2420–2421.

(26) Wang, A. J.; Qin, M. L.; Guan, J.; Wang, L.; Guo, H. C.; Li, X.; Wang, Y.; Prins, R.; Hu, Y. K. *Angew. Chem., Int. Ed.* **2008**, *47*, 6052–6054.

(27) Henkes, A. E.; Vasquez, Y.; Schaak, R. E. *J. Am. Chem. Soc.* **2007**, *129*, 1896–1897.

(28) Park, J.; Koo, B.; Hwang, Y.; Bae, C.; An, K.; Park, J.-G.; Park, H. M.; Hyeon, T. *Angew. Chem., Int. Ed.* **2004**, *43*, 2282−2285.

(29) Qian, C.; Kim, F.; Ma, L.; Tsui, F.; Yang, P.; Liu, J. *J. Am. Chem. Soc.* **2004**, *126*, 1195−1198.

(30) Layan Savithra, G. H.; Bowker, R. H.; Carrillo, B. A.; Bussell, M. E.; Brock, S. L. *Chem. Mater.* **2013**, *25*, 825–833.

(31) Eustis, S.; El-Sayed, M. A. *Chem. Soc. Rev.* **2006**, *35*, 209–217.

(32) Huang, X.; Jain, P. K.; El-Sayed, I. H.; El-Sayed, M. A. *Lasers Med. Sci.* **2008**, *23*, 217–228

(33) Li, J. F.; Huang, Y. F.; Ding, Y.; Yang, Z. L.; Li, S. B.; Zhou, X. S.; Fan, F. R.; Zhang, W.; Zhou, Z. Y.; Wu, D. Y. *Nature* **2010**, *464*, 392–395.

(34) Pillai, S.; Catchpole, K. R.; Trupke, T.; Green, M. A. *J. Appl. Phys.* **2007**, 101, 093105.

(35) Maier, S. A.; Brongersma, M. L.; Kik, P. G.; Meltzer, S.; Requicha, A. A. G.; Atwater, H. A. *Adv. Mater.* **2001**, *13*, 1501−1505.

(36) Gu, Y.; Sun, W.; Wang, G.; Fang, N. *J. Am. Chem. Soc.* **2011**, *133*, 5720–5723.

(37) Gu, Y.; Ha, J. W.; Augspurger, A. E.; Chen, K.; Zhu, S.; Fang, N. *Nanoscale* **2013**, *5*, 10753–10764.

(38) Saxton, M. J.; Jacobson, K. *Annu. Rev. Biophys. Biomol. Struct.* **1997**, *26*, 373–399.

(39) Fujiwara, T.; Ritchie, K.; Murakoshi, H.; Jacobson, K.; Kusumi, A. *J. Cell Biol.* **2002**, *157*, 1071–1081.

CHAPTER 2.

MICROSTRUCTURE EFFECTS ON THE WATER OXIDATION ACTIVITY OF Co_3O_4/POROUS SILICA NANOCOMPOSITES

A paper Published in *ACS Catal.* **2015**, *5*, 1037−1044.

Chia-Cheng Lin,[‡] Yijun Guo,[†] Javier Vela[*]

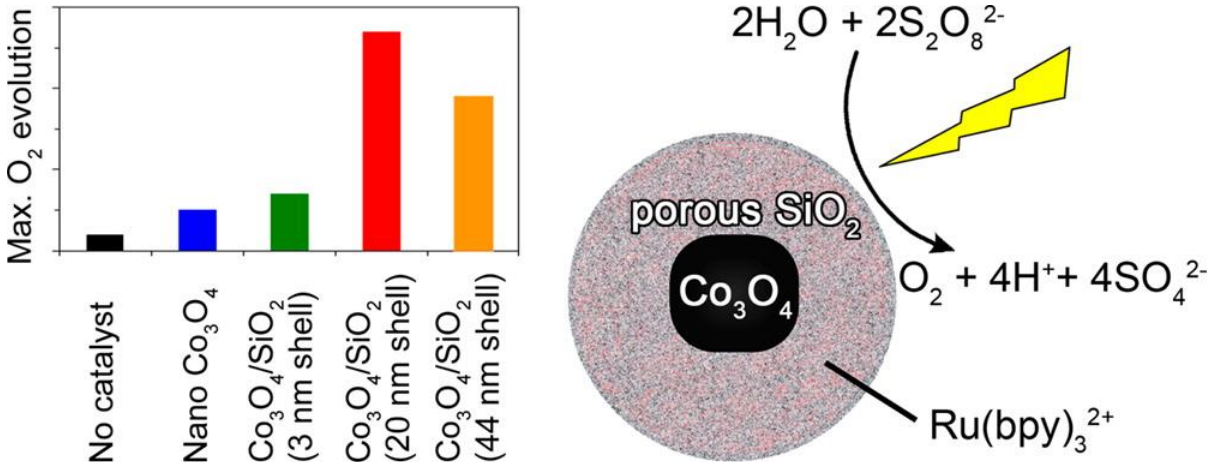

Abstract

We investigate the effect of microstructuring on the water oxidation (oxygen evolution) activity of two types of Co_3O_4/porous silica composites: Co_3O_4/porous SiO_2 core/shell nanoparticles with varying shell thicknesses and surface areas, and Co_3O_4/mesoporous silica nanocomposites with various surface functionalities. Catalytic tests in the presence of $Ru(bpy)_3^{2+}$ as a photosensitizer and $S_2O_8^{2-}$ as a sacrificial electron acceptor show that porous silica shells of up to ~20 nm in thickness lead to increased water oxidation activity. We attribute this effect to either (1) a combination of an effective increase in catalyst

---

[‡] Primary researcher and author
[†] Contributed to TEM image collection
[*] Author for correspondence

active area or consequent higher local concentration of $Ru(bpy)_3^{2+}$; (2) a decrease in the permittivity of the medium surrounding the catalyst surface and a consequent increase in the rate of charge transfer; or both. Functionalized Co_3O_4/ mesoporous silica nanocomposites show lower water oxidation activity compared with the parent nonfunctionalized catalyst, likely because of partial pore blocking of the silica support upon surface grafting. A more thorough understanding of the effects of microstructure and permittivity on water oxidation ability will enable the construction of next generation catalysts possessing optimal configuration and better efficiency for water splitting.

Introduction

Electrochemical and photochemical water splitting are ways to produce molecular hydrogen gas, H_2, a potentially valuable and clean-burning fuel. Water oxidation is the most difficult half reaction in water splitting, involving the transfer of four electrons and the formation of oxygen−oxygen bonds.[1−4] After many studies devoted to developing more efficient and economic water oxidation catalysts,[5] cobalt-based materials have been identified as some of the most promising due to their relative abundance, high activity, and stability.[2,6−8]

The synthesis and size-dependent properties of cobalt-based catalysts for electrochemical oxygen evolution have been examined previously.[9,10] A pH-dependent study of cobalt oxide electrocatalysts in fluoride buffer has been reported.[11] Cobalt oxide-decorated gold[12] or graphene[13] electrodes show some of the best catalytic performance in oxygen reduction and evolution reactions, whereas Co_3O_4-modified Ta_3N_5 photoanodes show enhanced performance and stability.[14,15] Co(II)-modified, fluorine-doped tin oxide has high catalytic activity,[16] as do self-repairing cobalt phosphate films[17] and diamondsupported Co_2O_3 nanoparticles.[18] Mesoporous Co_3O_4 prepared by hard-templating methods show increased stability and electrocatalytic ability.[19–21]

Several metal oxide-based photocatalytic systems in which the $[Ru(bpy)_3]^{2+}$ complex cation and $S_2O_8^{2-}$ serve as photosensitizer and sacrificial electron acceptor, respectively, have been developed. These include Mn_3O_4 embedded in mesoporous silica;[22,23] colloidal IrO_2;[24] MnO_2 nanotubes and wires;[25] amorphous manganese oxide;[26] MnO_2 on carbon nanotubes;[27] $LaCoO_3$, $CoWO_4$, $NdCoO_3$ and YCoO;[28] calcium manganese(III) oxide;[29] Mn−Ga−Co spinel;[30] cobalt/methylenediphosphonate;[31] $Li_2Co_2O_4$;[32] and $NiFe_2O_4$.[33]

Other than heterogeneous catalysts, homogeneous cobalt-based water oxidation catalysts that also require $[Ru(bpy)_3]^{2+}$ and $S_2O_8^{2-}$ have been developed. Carbon-free cobalt polytungstate complexes show improved stability and catalytic ability over traditional homogeneous water oxidation catalysts.[34-39] Water-soluble mononuclear cobalt complexes are converted into active $Co(OH)_x$ species during photocatalysis.[40] $Co(OH)_2$ derived from Co(II) adsorbed on silica shows high catalytic activity and stability.[41] Catalytic Co_4O_4 cubanes are known to mimic photosystem II.[42, 43]

Water oxidation over mesoporous silica-supported Co_3O_4 clusters has drawn much recent interest.[44] The photo- and electrochemical activities of ligand-free Co_3O_4 nanoparticles of different shapes on different supports have been studied.[45] Co_3O_4/SBA-15 catalysts show higher activity than Co_3O_4/MCM41 catalysts.[46] Smaller Co_3O_4 clusters and 3-D connecting pore structures lead to better performance.[47] Mn-doped mesoporous Co_3O_4 performs better than pure Co_3O_4.[48, 49] Cobalt complexes grafted on SBA-15, zeolite-supported CoO_x, and hollow Co_3O_4 particles have also been reported.[50-54] The mechanism of hole transport from

$[Ru(bpy)_3]^{2+}$ to the surface of Co_3O_4 was studied using Co_3O_4/SiO_2 core/shell catalysts impregnated with organic molecules as charge transfer media.[55, 56]

Fundamental studies on the microscopic mechanism of water oxidation using both homogeneous (molecular) Co complexes[57] and heterogeneous Co_3O_4 catalysts[58] provide useful leads for new catalyst design and optimization. Theoretical calculations have described the adsorption and oxidation of water molecules on the $Co_3O_4(110)$ surface.[59] Here, we present our study on the effect of porous silica shell thickness and different surface grafted groups on the water oxidation activity of Co_3O_4/SiO_2 core/shells and Co_3O_4/mesoporous silica composites, respectively.

Results and Discussion

Co_3O_4/Porous SiO_2 Core/Shells

Co_3O_4 nanocrystals were synthesized by thermal decomposition of cobalt(II) oxalate at 400 °C in air for 2 h (see the Experimental Section). As shown in Figure 1, the powder XRD pattern of the as-synthesized Co_3O_4 nanocrystals shows diffraction peaks that match those of the reference bulk spinel Co_3O_4 phase. In contrast, none of the experimentally observed diffraction peaks match those of bulk CoO, suggesting that the nanocrystals are made of highly phase-pure Co_3O_4. The diffuse reflectance spectrum of Co_3O_4 nanocrystals (Figure 2) shows two peaks at ~425 and 725 nm. This is consistent with the characteristic absorption of Co_3O_4, containing octahedral Co^{3+} and tetrahedral Co^{2+} ions.[66]

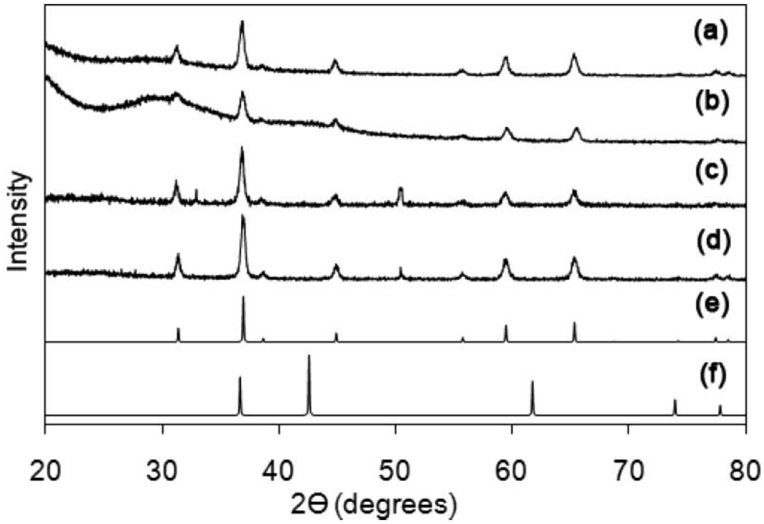

Figure 1. Wide-angle powder XRD data for 17.2 ± 3.8 nm Co_3O_4 nanocrystals (a); Co_3O_4/porous SiO_2 core/shell nanoparticles with different shell thicknesses of 3.1 ± 0.6 nm (b), 19.8 ± 1.4 nm (c), 44.1 ± 8.3 nm (d); and bulk Co_3O_4 (e) and CoO (f).

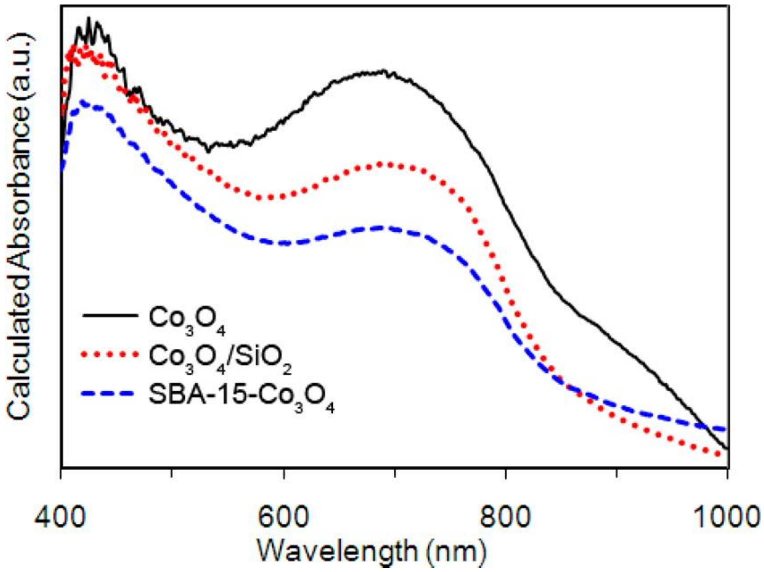

Figure 2. Diffuse reflectance spectra of bare (uncoated) Co_3O_4 nanocrystals (a), Co_3O_4/porous SiO_2 core/shell nanoparticles (19.8 ± 1.4 nm shell thickness) (b), and SBA-15-Co_3O_4 nanocomposites (4.4 ± 0.8 nm Co_3O_4 particle size) (c).

As shown in Figure 3, TEM shows that the Co_3O_4 nanocrystals have truncated polyhedral shapes with an average size (diameter) of 17.2 ± 3.8 nm. This is consistent with the grain size of 16 nm estimated from XRD peak widths using the Scherrer equation. Nitrogen physisorption analysis shows the specific surface area of Co_3O_4 nanocrystals is 38 m^2/g (Table 1), which is consistent with a surface area of 49 m^2/g estimated from a spherical particle model calculation. These Co_3O_4nanocrystals were coated with porous silica (SiO_2) shells via CTAB-templated sol–gel condensation of tetraethylorthosilicate (TEOS) with NH_4OH as catalyst in ethanol solvent. TEM shows different amounts of TEOS resulted in different Co_3O_4/porous SiO_2 core/shell nanoparticles with various shell thicknesses (3.1 ± 0.6, 19.8 ± 1.4, and 44.1 ± 8.3 nm, Figures 1 and 3 and Table1). The organic template, CTAB, was removed via calcination at 550 °C under air for 6 h.

Table 1. Structural parameters of Co_3O_4/SiO_2 core/shell nanoparticles with different shell thicknesses.

Sample	Core size (nm)[a]	Shell thickness (nm)[a]	S_{BET} $(m^2/g)^b$	Pore size (nm)[c]	Pore volume (cm^3/g)
Co_3O_4	17.2 ± 3.8	0	38	N/A	0.15
Co_3O_4/SiO_2 (3 nm)	19.1 ± 3.1	3.1 ± 0.6	130	N/A	0.15
Co_3O_4/SiO_2 (20 nm)	19.9 ± 3.0	19.8 ± 1.4	210	3.8	0.15
Co_3O_4/SiO_2 (44 nm)	24.1 ± 3.5	44.1 ± 8.3	390	3.9	0.22

[a]Determined by TEM. [b]Obtained by the BET method. [c]Obtained by the BJH method.

Representative powder XRD, diffuse reflectance, and TEM data of Co_3O_4/porous SiO_2 core/shell nanoparticles are summarized in Figures 1, 2, and 3. As the silica shell becomes thicker, no significant peak shifts or new peaks are observed. The XRD patterns also reveal that the phase and grain size of the Co_3O_4 nanocrystals remain the same after silica coating, suggesting that the basic environment employed for silica coating does not affect the nanoparticles' Co_3O_4 cores. Similarly, no significant peaks appear in the low-angle XRD region (data not shown) of the Co_3O_4/porous SiO_2 core/shell nanoparticles. This implies that the porous silica shell may not be as ordered as other reported porous silica-coated materials that also use CTAB as a template or surfactant. In agreement with these XRD observations, diffuse reflectance and TEM confirm that the optical structure and size of the Co_3O_4 nanocrystals did not change appreciably through the silica shell growth process (Figure 3).

The average core size and shell thicknesses for different Co_3O_4/porous SiO_2 core/shell nanoparticles are summarized in Table 1. Increasing amounts of TEOS clearly resulted in larger shell thickness. This suggests that consecutive addition of TEOS resulted in the growth of (more) silica on pre-existing particles via heterogeneous nucleation, rather than forming new silica nuclei via homogeneous nucleation.

TEM reveals a foam-like surface structure is present atop the Co_3O_4/porous SiO_2 core/shell nanoparticles (Figure 3b–d). Nitrogen physisorption experiments were also performed to characterize the pore structure and surface area of the Co_3O_4/porous SiO_2 particles and their shells. The particles with 19.8 ± 1.4 and 44.1 ± 8.3 nm silica shells have calculated pore sizes of 3.8 and 3.9 nm, respectively, as obtained by the BJH method (see the Experimental Section, and Table 1). Core/shell particles with thinner silica layers did not show significant peaks by the BJH method. Across all samples studied, the specific surface area increased as the shell thickness increased. The pores in the silica shell are produced after the removal of CTAB molecules; the diameter of the pores is thus dictated by the size of the CTAB micelles formed during the sol gel process. Because the concentrations of CTAB, EtOH, and H_2O were the same in each run, the increase in surface area is consistent with increasing shell thickness while the pore size remains constant.

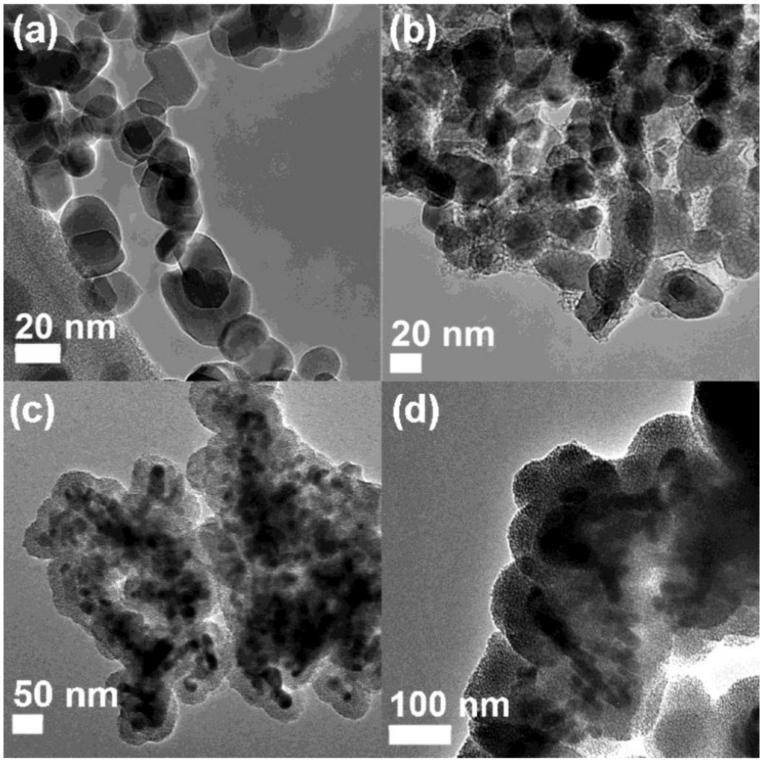

Figure 3. TEM of 17.2 ± 3.8 nm Co_3O_4 nanocrystals (a) and Co_3O_4/porous SiO_2core/shell nanoparticles with different shell thicknesses of 3.1 ± 0.6 nm (b), 19.8 ± 1.4 nm (c), and 44.1 ± 8.3 nm (d).

Probing Pore Accessibility by NMR

We then turned our attention to assessing the accessibility of the catalytically active Co_3O_4surface to small molecules. While infrared spectroscopy provides one way to assess the degree of surface coverage by a silica shell,[67, 68] we specifically sought to probe pore accessibility using nuclear magnetic resonance (NMR). NMR measurements of two chemically related molecules with very different sizes, ethylene glycol (EG) and polyethylene glycol tridecamer (EG_{13} or Poly600), were used to examine the pore accessibility of the Co_3O_4/porous SiO_2 core/shell nanoparticles. For all measurements, the concentration of ethoxyl protons ($-O\underline{CH_2CH_2}O-$) in both EG and Poly600 were kept the same (confirmed by chemical integration), as was the concentration of (bare or coated) Co_3O_4 nanocrystals (confirmed by Co_3O_4 optical density or absorbance). Thus, only the thickness of the porous silica shells varied in different specimens.

Figure 4 shows the longitudinal (T_1) and transverse (T_2) relaxation times for the ethoxyl protons ($-O\underline{CH_2CH_2}O-$) in EG and Poly600 in the absence and presence of Co_3O_4/porous SiO_2core/shells. As expected, the T_1 values of EG and Poly600 do not change significantly with added Co_3O_4/porous SiO_2, regardless of the thickness of the silica shell (Figure 4a); however, the T_2values for both EG and Poly600 progressively increase with increasing shell thickness (Figure 4b). Magnetic particles have been shown to be T_2 relaxers.[69] Studies with Fe_2O_3/SiO_2 core/shells showed that the thinnest shells have the strongest T_2 shortening effect.[70] A polymer-coated Fe_2O_3 composite shows enhanced T_2 shortening near the particle surface.[71]

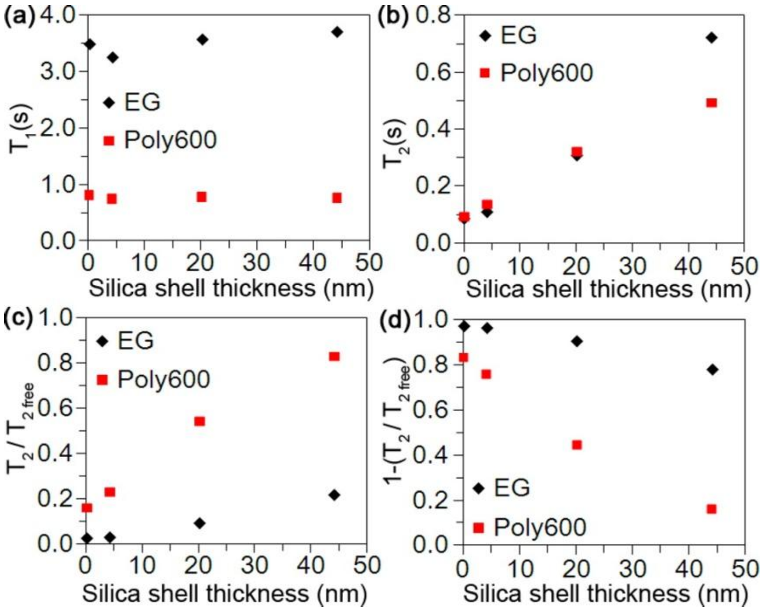

Figure 4. Longitudinal (T_1) (a) and transverse (T_2) (b, c, d) relaxation times for the ethoxyl protons ($-O\underline{CH_2CH_2}O-$) in EG and Poly600 in the absence or presence of Co_3O_4/porous SiO_2 core/shell nanoparticles with different shell thicknesses in D_2O ($T_{2free} = T_2$ in the complete absence of Co_3O_4).

Naturally, this shortening of the T_2 suggests that the magnetic Co_3O_4 core has a much larger influence on helping relax those protons that can get closer to the magnetic surface. It follows that thicker silica shells should increasingly separate and minimize the magnetic screening of protons by the magnetic Co_3O_4 core. Because the silica shells have a definite pore size (~4 nm), we hypothesized that the smaller EG monomer molecules should be able to penetrate the shell and continue to be impacted to a greater degree compared to the much larger Poly600 tridecamer molecules. To investigate this idea, the measured T_2 values were parametrized by dividing them over the unaffected, natural T_2 values (T_{2free}) of EG and Poly600 (measured in the absence of Co_3O_4; T_2/T_{2free} and $1 - T_2/T_{2free}$ in Figures 4c and 4d, respectively). After parametrization, it is clear that although the protons in both EG and Poly are relaxed by Co_3O_4, those in Poly600 are much more sensitive to the thickness of the silica shell.

We explain these observations as follows: With a hydrodynamic diameter of ~1 nm,[72, 73] the larger Poly600 molecules have much greater difficulty diffusing through the longer, more tortuous pathway needed to reach the magnetic Co_3O_4 core surface as the SiO_2 shell increases. In contrast, because the EG molecules are much smaller than the SiO_2 pores, thicker SiO_2 shells only slightly hinder the diffusion of EG molecules closer to the core. This results in a stronger T_2 shortening effect for EG.

Shorter diffusion pathways in Co_3O_4/porous SiO_2 particles with thinner shells allow molecular probes to move closer to the magnetic core. For the thinnest shells and the bare (uncoated) Co_3O_4 nanocrystals, small and large molecules are able to reach the magnetic surface and are affected equally. Together with the physisorption and TEM measurements presented above, these NMR experiments strongly suggest that that the surface of Co_3O_4 nanocrystals is accessible by small molecular substrates and reagents through a vast network of well-defined, ~4 nm pores. In contrast, the diffusion of large molecules such as Poly600 into the core region is hindered as their size becomes comparable with that of the pores. The porous silica shell thus serves as a sieve or filter for larger molecules.

Co_3O_4/SBA-15 Nanocomposites

Co_3O_4/SBA-15 nanocomposites were prepared by the sol–gel reaction between TEOS and H_2O, using HCl as catalyst and the block copolymer P123 as a structure-directing agent. The organic template was removed by calcination at 550 ℃ under air. Wet impregnation of cobalt(II) nitrate and calcination at 400 ℃ in air yielded Co_3O_4/SBA-15 nanocomposites with a nominal Co_3O_4loading of 4 wt %. Further modification of the silica surface was conducted by postgrafting with various functional silanes (see the Experimental Section).

Low-angle XRD measurements show three peaks at 1.03°, 1.77°, and 2.01° corresponding to the (100), (110), and (200) planes in 2-D hexagonally packed SBA-15, respectively (Figure 5). The intensity of these three peaks remained unchanged after introduction of cobalt oxide, which suggests that the mesostructure of the SBA-15 support remained mostly intact. Wide-angle XRD measurements show that all modified (surface grafted) and unmodified Co_3O_4/SBA-15 nanocomposites contain standard spinel Co_3O_4 nanocrystals with a similar Scherrer particle size of 4.4 ± 0.8 nm (Figure 5). Nitrogen physisorption measurements show that, after the introduction of Co_3O_4, the surface area of Co_3O_4/SBA-15 nanocomposites dropped from 734 to 570 m^2/g, while the pore size remained nearly identical, from 6.5 to 6.4 nm. Post-synthetic grafting with silanes slightly decreased the surface area and also the pore size of the composites by up to 140 m^2/g and 0.6 nm, respectively (Table 2). It is noteworthy that the most dramatic decrease in surface area, pore size, and pore volume occurred in the amino ($-CH_2CH_2CH_2NH_2$)-modified specimen; however, no other significant changes in pore structure were observed in these surface modified Co_3O_4/SBA-15 composites. DP-MAS ^{29}Si NMR measurements were conducted to confirm the surface modification (Figure 6). New T bands (T^3 and T^2) are observed for sites derived from $NH_2CH_2CH_2CH_2Si(OSi)_3/NH_2CH_2CH_2CH_2Si(OH)(OSi)_2$ and $PhSi(OSi)_3/PhSi(OH)(OSi)_2$ groups. A peak at ~15 ppm is observed for $Me_3Si(OSi)_3$ groups.[74-76]

Table 2. Structural data of SBA-15 and Co_3O_4-SBA-15 nanocomposites.

Sample	S_{BET} (m^2/g)	Pore size (nm)[a]	Pore volume (cm^3/g)
SBA-15	730	6.5	0.95
Co_3O_4-SBA-15	570	6.4	0.91
Co_3O_4-SBA-15-$SiMe_3$	550	6.3	0.79
Co_3O_4-SBA-15-$SiCH_2CH_2CH_2NH_2$	430	5.8	0.70
Co_3O_4-SBA-15-SiPh	520	6.4	0.74

[a] Obtained by the BJH method.

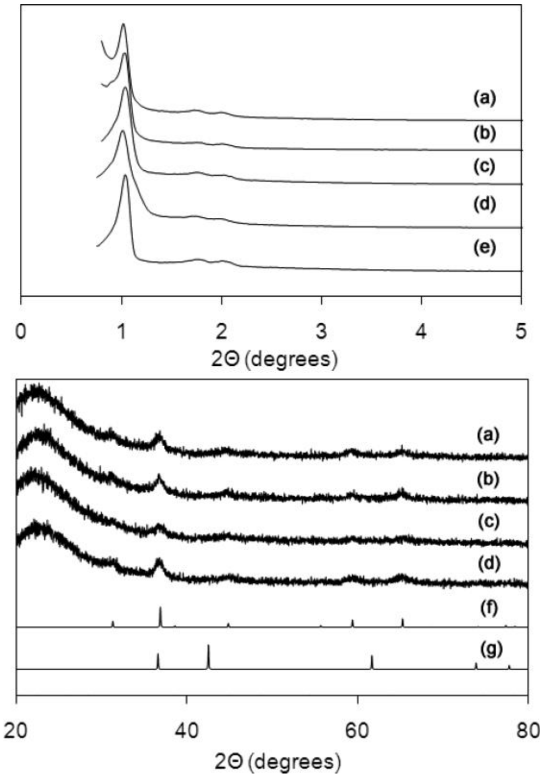

Figure 5. Low-angle (top) and wide-angle (bottom) powder XRD data for Co_3O_4/SBA-15 nanocomposites (4.4 ± 0.8 nm Co_3O_4 particle size): Co_3O_4/SBA-15/SiPh (a), Co_3O_4/SBA-15/$SiCH_2CH_2CH_2NH_2$ (b), Co_3O_4/SBA-15/$SiMe_3$ (c), Co_3O_4/SBA-15 (d), and SBA-15 (e). Bulk Co_3O_4 (f) and CoO (g) are shown for reference.

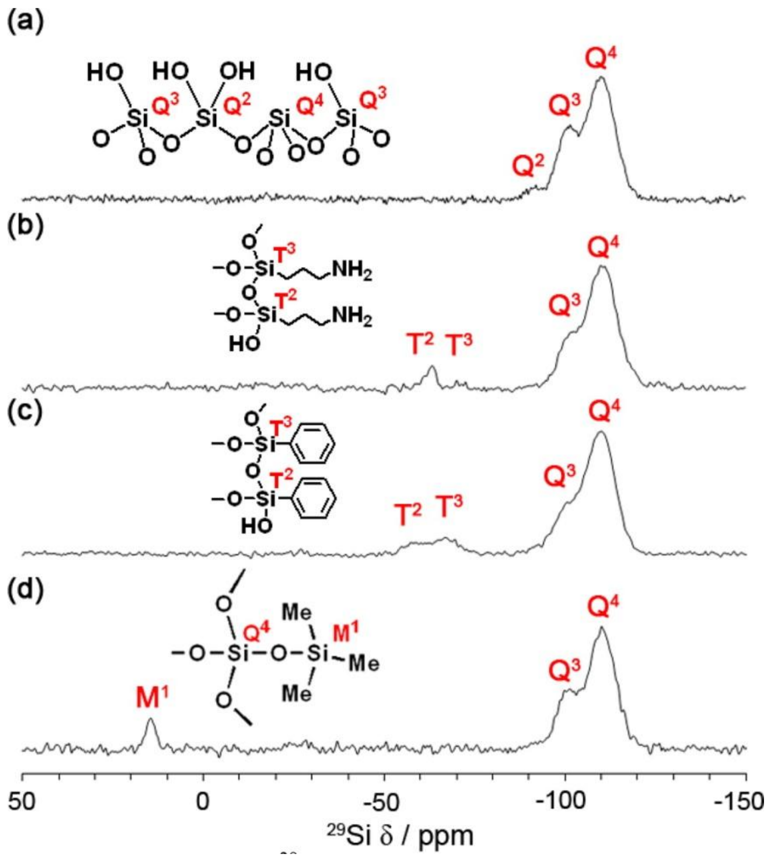

Figure 6. DP-MAS ^{29}Si NMR spectra of Co_3O_4/SBA-15 nanocomposites before (a) and after surface functionalization (by grafting) with $-(CH_2)_3NH_2$ (b), −Ph (c), and $-SiMe_3$ (d) groups.

The catalytic activity of Co_3O_4/porous SiO_2 core/shell nanoparticles toward water oxidation was measured using a photosensitizer ($Ru[(bpy)_3]Cl_2 \cdot 6H_2O$), a sacrificial electron acceptor ($Na_2S_2O_8$–Na_2SO_4), and an aqueous buffer (pH 5.8, $NaSiF_6$–$NaHCO_3$) medium. Reactions were conducted under continuous irradiation by 575 ± 100 nm lamps while taking aliquots of the headspace and injecting them into a GC equipped with a TCD detector to measure the oxygen (O_2) produced. Our setup (septum, etc.) was independently tested under similar conditions to ensure that there was no leakage or other noncatalytic sources of O_2.

The overall cycle for water oxidation under these conditions is shown in Scheme 1. $Ru(bpy)_3^{2+}$ is first excited by the incident radiation to form an excited state, $Ru(bpy)_3^{2+}*$. Subsequent electron transfer from $Ru(bpy)_3^{2+}*$ to $S_2O_8^{2-}$ yields $Ru(bpy)_3^{3+}$ and $SO_4^{\bullet-}$. $SO_4^{\bullet-}$ further oxidizes another equivalent of $Ru(bpy)_3^{2+}$ to $Ru(bpy)_3^{3+}$. This $Ru(bpy)_3^{3+}$ reacts with water and oxidizes it on the surface of the Co_3O_4 catalyst, producing molecular oxygen (O_2). The free energy of the full process is calculated to be negative (exergonic or "downhill") and equal to −280 kJ/mol.

$$2H_2O \rightarrow O_2 + 4H^+ + 4e^- \qquad E_{red} = -1.23\ V$$

$$S_2O_8^{2-} + 4e^- \rightarrow 2SO_4^{2-} \qquad E_{ox} = 1.96\ V$$

$$2H_2O + 2S_2O_8^{2-} \rightarrow O_2 + 4H^+ + 4SO_4^{2-} \qquad E_{rxn} = 0.73\ V$$

$$\Delta G° = -nFE = -4 \times 96485\ C/mol \times 0.73\ V = -280\ kJ/mol$$

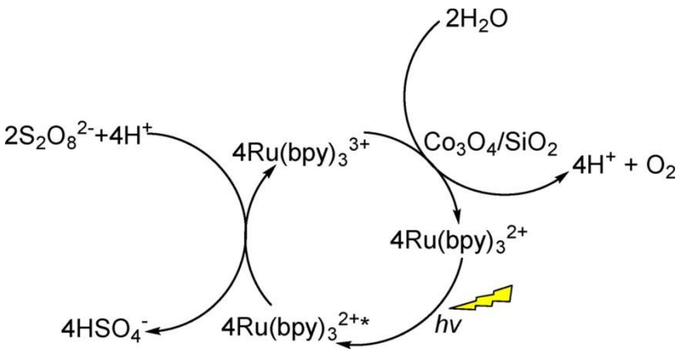

Scheme 1. Water Oxidation by $S_2O_8^{2-}$ Catalyzed by Co_3O_4/SiO_2 and $Ru(bpy)_3^{2+}$ (chloride salt) as Photosensitizer

Figure 7 and Table 3 show the experimentally observed oxygen evolution activities of different Co_3O_4/porous SiO_2 nanocatalysts. In all cases, the amount of O_2 in the reactor headspace increased until reaching a plateau after 40–90 min. We interpret this plateau as the point at which the maximum yield of O_2 production in each case was achieved. Among the Co_3O_4/porous SiO_2nanocatalysts studied, the bare, uncoated Co_3O_4 had the lowest activity. O_2 production then increased with increasing silica shell thickness up to a point; activity reached a maximum for Co_3O_4/porous SiO_2 with a 19.8 ± 1.4 nm shell, then decreased with a thicker shell (O_2 production activity was negligible in the absence of the nanocatalyst). We speculatively attribute this behavior to either one or both of two possible factors: (i) The positively charged $Ru(bpy)_3^{2+}$ photosensitizer may have a high affinity toward the negatively polarized SiO_2 surface. Thicker shells provide for a much larger SiO_2 surface (Table 1), increasing the effective concentration (and activity) of $Ru(bpy)_3^{2+}$ near or at the catalytically active Co_3O_4 surface. (ii) The porous silica coating could increase the effectiveness (rate of) electron transfer steps necessary for catalysis due to the lower permittivity (dielectric constant) of silica (3.9) compared with pure water (80). The lower permittivity could decrease the reorganizational energy term as described by Marcus theory, increasing the overall rate of electron transfer. The carrier mobility in 1-D and 2-D semiconductor nanostructures is sensitive to permittivity,[77] as is that of single-layer graphene transistors in different dielectric environments.[78, 79]

The catalytic activities of surface-modified and unmodified Co_3O_4/SBA-15 nanocomposites were also measured for comparison (Figure 8 and Table 3). The concentration of O_2 produced using Co_3O_4/SBA-15 nanocomposites reached a maximum yield within 50–60 min, which is consistent with the aforementioned and with prior reports.[22, 44] Interestingly, among the composite catalysts, it is the unmodified sample that possesses the best performance, whereas the other three modified samples possessed lower, similar activities. The composites containing the most hydrophobic surface groups (−SiPh and

−$SiMe_3$) and thus, a low permittivity, show relatively low activity, arguing against factor ii, above. More generally, however, we believe that the decrease in activity in the surface-grafted composites is most likely attributable to a decrease in the SiO_2surface available for binding by the $Ru(bpy)_3^{2+}$ photosensitizer (roughly opposite to factor i, mentioned above), as indicated by physisorption measurements (Table 2); albeit, this could be compensated somewhat by the introduction of surface −NH_2 groups in one of the nanocomposites.

Table 3. Oxygen evolution performance of Co_3O_4/SiO_2 core/shell nanoparticles with different shell thicknesses and Co_3O_4-SBA-15 nanocomposites.

Sample	Oxygen evolved (μmol)	Yield (%)
Co_3O_4	5.2	3.8
Co_3O_4/SiO_2 (3 nm)[a]	8.7	6.4
Co_3O_4/SiO_2 (20 nm)[a]	26.7	19.6
Co_3O_4/ SiO_2 (44 nm)[a]	19.8	14.5
Co_3O_4-SBA-15	28.5	20.8
Co_3O_4-SBA-15-$SiMe_3$	20.4	15.0
Co_3O_4-SBA-15-$SiCH_2CH_2CH_2NH_2$	15.4	11.3
Co_3O_4-SBA-15-SiPh	19.4	14.2

[a] Approximate shell thickness (as in Table 1).

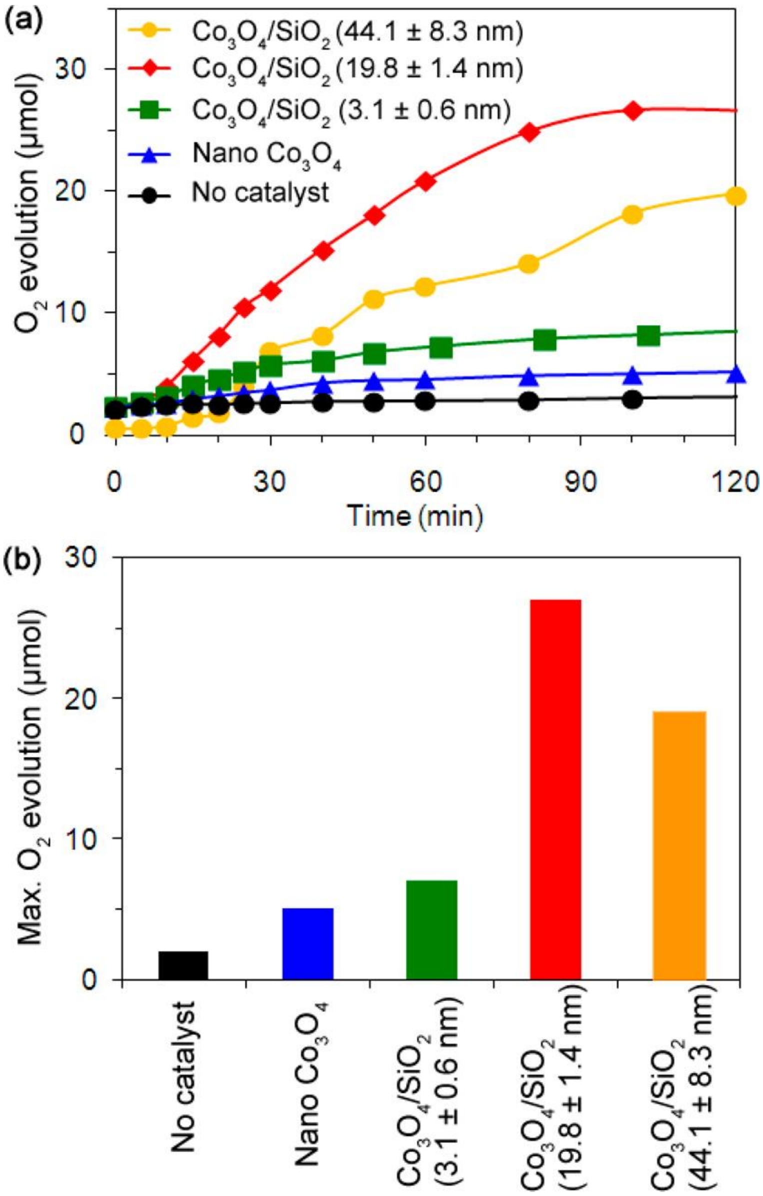

Figure 7. Oxygen evolution (a) and maximum O_2 yields (measured between 90 and 120 min, b) from the reaction of water with persulfate in the presence of $[Ru(bpy)_3]Cl_2$sensitizer and Co_3O_4/SiO_2 core/shells under 575 ± 100 nm lamp illumination (the total Co_3O_4 loading and concentration were maintained constant).

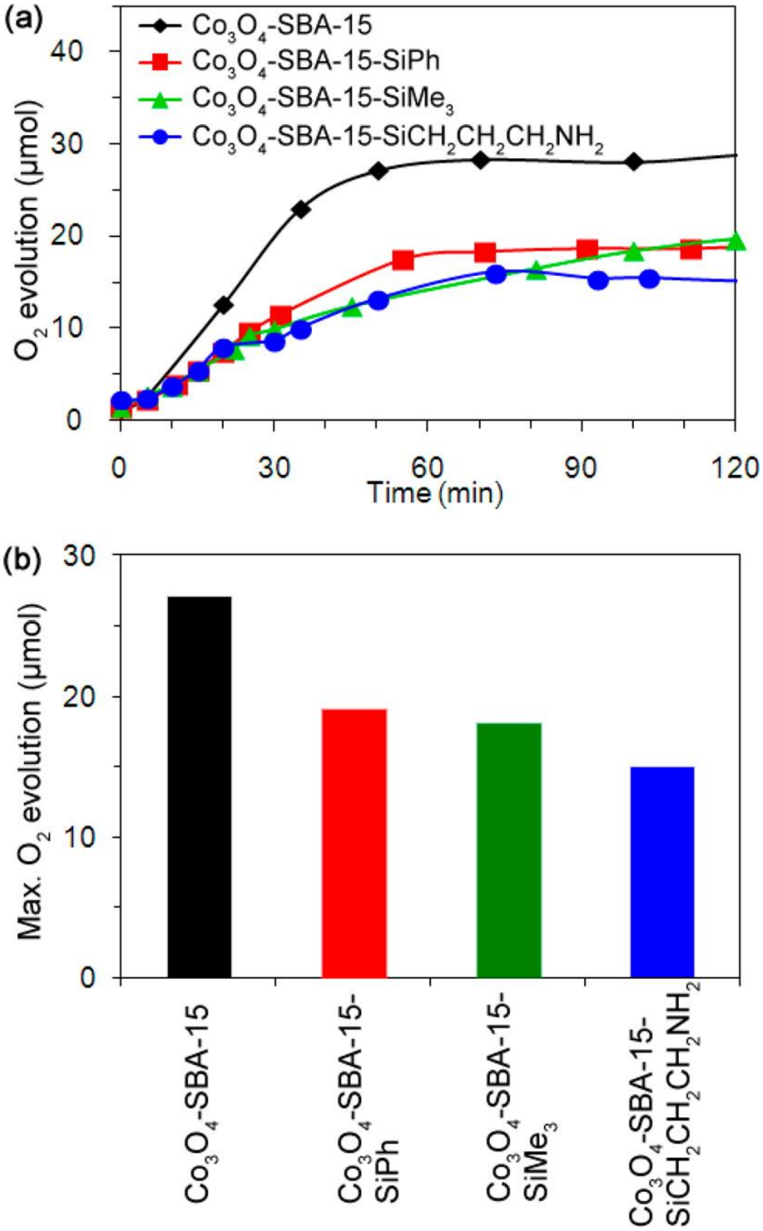

Figure 8. Oxygen evolution (a) and maximum O_2 yields (measured between 60 and 120 min, b) from the reaction of water with persulfate in the presence of $[Ru(bpy)_3]Cl_2$sensitizer and Co_3O_4/SBA-15 nanocomposites under 575 ± 100 nm lamp illumination (the total Co_3O_4 loading and concentration were maintained constant).

Conclusion

We have prepared several Co_3O_4/porous silica nanocomposites to investigate the effect of catalyst microstructure and its local environment on water oxidation activity. We have also utilized NMR relaxation time measurements of two different probe molecules (EG and Poly600) to study the pore accessibility of Co_3O_4/porous SiO_2 core/shell nanoparticles with different shell thicknesses (but similar pore size and structure).

In our study of catalytic activity of Co_3O_4/porous SiO_2 core/shell nanoparticles toward water oxidation (oxygen evolution reaction), the catalyst with a 19.8 ± 1.4 nm shell had superior activity over the uncoated, thinner, and thicker silica shell catalysts as a result of two possible factors: First, the higher surface area of the thicker porous silica shell helps to increase the local $Ru(bpy)_3^{2+}$ concentration near the active Co_3O_4 surface. Second, the reduced reorganization energy due to the lower dielectric constant of silica might also facilitate the charge transfer rate. Increasing shell thicknesses were detrimental to catalytic activity, possibly because of slower diffusion of reactant molecules in and out of the SiO_2 pores.

In the case of Co_3O_4/SBA-15 nanocomposites, the unmodified sample possesses better activity than the modified samples. Surface-modified composites (e.g., −SiPh and $-SiMe_3$) have relatively low local surface permittivity compared with the unmodified composites; however, the loss of possible $Ru(bpy)_3^{2+}$ binding sites (hydroxyl group) and a measurable amount of pore blocking upon surface grafting results in the loss of reactivity. A more thorough understanding of the effects of microstructure and permittivity on water oxidation ability will enable the construction of next generation catalysts possessing optimal configuration and better efficiency for water oxidation and water splitting.

Experimental Section

Materials

Cobalt acetate tetrahydrate ($Co(OAc)_2 \cdot 4H_2O$), tetraethylorthosilicate (TEOS), Pluronic 123 (P-123, $HO(CH_2CH_2O)_{20}(CH_2CH(CH_3)O)_{70}(CH_2CH_2O)_2OH$), ammonium hydroxide ($NH_4OH$ 28 wt % aqueous solution), oxalic acid ($H_2C_2O_4$), cobalt(II) nitrate hexahydrate ($Co(NO_3)_2 \cdot 6H_2O$), poly(ethylene glycol) tridecamer ($HO(CH_2CH_2O)_{13}H$ (EG_{13} or PEG600), M_n = 600 g/mol), aminopropyltriethoxysilane ($H_2NCH_2CH_2CH_2Si(OEt)_3$), trimethylsilyl chloride (Me_3SiCl), tris(2,2′-bipyridyl)ruthenium(II) dichloride hexahydrate ($[Ru(bpy)_3]Cl_2 \cdot 6H_2O$), and deuterium oxide ($D_2O$) were purchased from Sigma-Aldrich; ethanol (absolute, 200 proof), ethylene glycol ($HOCH_2CH_2OH$; EG), and hydrochloric acid (HCl, concentrated) were from Fisher; cetyltrimethylammonium bromide (CTAB) was from Alfa Aesar; and phenyltrimethoxysilane ($PhSi(OMe)_3$) was from Gelest. All chemicals were used as received unless specified otherwise.

Synthesis

Co_3O_4 nanocrystals were prepared by a slightly modified procedure involving the thermal decomposition of cobalt(II) oxalate.[60] A solution of 0.3 M cobalt acetate in ethanol (50 mL) was heated and kept at 50 °C for 30 min, followed by quick addition of oxalic acid (1.07 g, 11.9 mmol). After 2 h at 50 °C, the cobalt(II) oxalate product was collected by concentration under vacuum at 80 °C. Heating cobalt(II) oxalate powder to 400 °C in a crucible in air for 2 h yielded Co_3O_4nanocrystals.

Co_3O_4/porous SiO_2 core/shells. Co_3O_4 nanocrystals were coated with porous SiO_2 shells of varying thicknesses by modified literature procedures.[61-63] Co_3O_4 (50 mg, 0.21 mmol) was added to a mixture of CTAB (0.22 g, 0.60 mmol), 28 wt % aqueous NH_4OH (4.2

mL, 62.3 mmol), and ethanol (50 mL). After 15 min of sonication and 15 min of vigorous stirring, TEOS (25 μL, 0.11 mmol for 3 nm shell; 150 μL, 0.67 mmol for 20 nm shell; 600 μL, 2.64 mmol for 44 nm shell) was introduced in multiple small additions (<50–100 μL/h). The solution was stirred for 19 h at room temperature (RT). Solids were collect by centrifugation (5000 rpm, 10 min), and the surfactant was removed by calcination at 550 °C in air for 6 h.

Co_3O_4/SBA-15 nanocomposites. SBA-15[64] and Co_3O_4/SBA-15 nanocomposites[47, 65] were prepared by modified literature procedures. P-123 (33 g, 5.69 mmol), concentrated HCl (16.6 g, 0.17 mol), and deionized water (517 g) were mixed by stirring vigorously at 35 °C for 30 min. TEOS (62.0 g, 0.30 mol) was added. After 1 day of stirring, the mixture was moved to an oven preheated to 90 °C and kept at this temperature for 1 day. Solids were collected by filtration and dried at 90 °C. The template was removed by calcination at 550 °C in air for 6 h. SBA-15 (0.2 g) was added to a 0.022 M cobalt(II) nitrate solution in ethanol (5 mL, 0.11 mmol), and the resulting pink slurry was stirred overnight until the solvent completely evaporated. This cobalt salt-impregnated SBA-15 was heated to 400 °C in air for 3 h. For surface grafting, Co_3O_4/SBA-15 composite (0.5 g) was degassed under vacuum at 110 °C for 2 h. Toluene (100 mL) and functional silane (44 mg of $H_2NCH_2CH_2CH_2Si(OEt)_3$, 40 mg of $PhSi(OMe)_3$, or 22 mg of Me_3SiCl; 2 mmol) were added. The mixture was refluxed at 78 °C under a dry N_2 atmosphere for 6 h. Solids were collected by filtration, washed with toluene (200 mL), and dried at 90 °C.

Structural Characterization

Powder X-ray diffraction (XRD) data were recorded with a Rigaku Ultima IV diffractometer with a Cu Kα radiation source (40 kV, 44 mA). Nitrogen physisorption was measured on a Micromeritics ASAP 2020 surface area and porosimetry system. Samples were degassed at 100 ℃ under vacuum overnight before analysis. The surface area was calculated with the Brunauer–Emmett–Teller (BET) method in the relative pressure range of 0.005–0.25 of adsorption data. Pore size distribution was calculated with the Barret–Joyber–Halenda (BJH) method. Transmission electron microscopy (TEM) was measured on an FEI Tecnai G^2 F20 field emission scanning transmission electron microscope (S/TEM) at 200 kV (point-to-point resolution < 0.25 nm, line-to-line resolution < 0.10 nm).

Spectroscopic Characterization

UV–vis absorption spectra were collected with a photodiode-array Agilent 8453 UV–vis spectrophotometer. Diffuse reflectance spectra were collected with a SL1 Tungsten halogen lamp (vis−IR), a SL3 Deuterium lamp (UV), and a BLACK-Comet C-SR-100 Spectrometer from StellarNet Inc.

Pore accessibility study. Co_3O_4/porous SiO_2 core/shell samples were examined by ^1H NMR spectroscopy using EG and polyethylene glycol ($HO(CH_2CH_2O)_{13}H$; Poly600). Experiments were conducted on a Varian MR-400 spectrometer equipped with a OneNMR pulse-field-gradient probe operating at a ^1H frequency of 399.80 MHz. EG (233 mg, 3.75 mmol) and Poly600 (317 mg, 0.53 mmol) were mixed in D_2O (5 g). A fraction of this EG/Poly600/D_2O solution (50 μL) and a solution of Co_3O_4/porous SiO_2 in D_2O (0.067 mM, 450 μL; 7.5 μg or 0.03 μmol of Co_3O_4) were mixed. NMR measurements of ethylene glycol and polyethylene glycol (Poly6oo) proton longitudinal (T_1) relaxation were conducted using the inverse recovery pulse sequence, and the transverse relaxation (T_2) was measured using a two-pulse spin echo sequence.

Solid state NMR spectra were measured with a Bruker Avance II 600 Spectrometer operating at 119.2 MHz for ^{29}Si equipped with a 4 mm Bruker MAS probe spinning at 10 kHz. ^{29}Si direct polarization magic angle spinning (DP-MAS) NMR spectra were recorded with a pulse width of 4 μs and a recycling delay of 1 min. ^{29}Si chemical shifts are referenced to TMS ($\delta = 0$ ppm).

Water Oxidation

A buffer solution of weakly coordinating ions was prepared from $NaHCO_3$ (0.353 g, 4.20 mmol) and Na_2SiF_6 (0.619 g, 3.30 mmol) in deionized water (150 mL).[31]The pH was adjusted to 5.8 with added $NaHCO_3$. Buffer (20 mL), Na_2SO_4 (0.195 g, 1.37 mmol), $Na_2S_2O_8$ (65 mg, 0.27 mmol), $[Ru(bpy)_3]Cl_2 \cdot 6H_2O$ (22.5 mg, 0.03 mmol), and Co_3O_4/silica sample (1 mg or 4.2 μmol of Co_3O_4 for Co_3O_4/porous SiO_2 core/shells, determined by optical density in solution; 2 mg or 8.4 μmol of Co_3O_4 for Co_3O_4/SBA-15 nanocomposites, determined by dry weight) were added to a 25 mL flask. The mixture was kept in the dark overnight and degassed by bubbling with dry N_2. O_2evolution was unobserved by GC prior to illumination. Water oxidation experiments were conducted inside a Rayonet photoreactor under illumination with 16 × 575 ± 100 nm side-on lamps. Headspace samples (100 μL) were directly analyzed each time using an Agilent 7890A GC system equipped with a HP-Molesieve column and a TCD detector.

Acknowledgment

We gratefully acknowledge the National Science Foundation for funding of this work through the Division of Materials Research, Solid State and Materials Chemistry program

(NSF-DMR-1309510). We thank Sarah Cady for assistance with NMR, Jeneé Jacobs and Sam Houk for assistance with ICP-MS, and Michelle Thompson for comments.

References

(1) Yan, Y.; Xia, B. Y.; Xu, Z.; Wang, X. *ACS Catal.* **2014**, 4, 1693–1705.

(2) Deng, X.; Tüysüz, H. *ACS Catal.* **2014**, 4, 3701– 371410.

(3) Maeda, K.; Domen, K. *J. Phys. Chem. Lett.* **2010**, 1, 2655– 2661.

(4) Cook, T. R.; Dogutan, D. K.; Reece, S. Y.; Surendranath, Y.; Teets, T. S.; Nocera, D. G. *Chem. Rev.* **2010**, 110, 6474– 6502.

(5) Inoue, H.; Shimada, T.; Kou, Y.; Nabetani, Y.; Masui, D.; Takagi, S.; Tachibana, H. *ChemSusChem* **2011**, 4, 173– 179.

(6) Nocera, D. G. *Acc. Chem. Res.* **2012**, 45, 767– 776.

(7) Reece, S. Y.; Hamel, J. A.; Sung, K.; Jarvi, T. D.; Esswein, A. J.; Pijpers, J. J. H.; Nocera, D. G. *Science* **2011**, 334, 645– 648.

(8) Artero, V.; Chavarot-Kerlidou, M.; Fontecave, M. *Angew. Chem., Int. Ed.* **2011**, 50, 7238–7266.

(9) Chou, N. H.; Ross, P. N.; Bell, A. T.; Tilley, T. D. *ChemSusChem* **2011**, 4, 1566–1569.

(10) Esswein, J.; McMurdo, M. J.; Ross, P. N.; Bell, A. T.; Tilley, T. D. *J. Phys. Chem. C* **2009**,113, 15068– 15072.

(11) Gerken, J. B.; McAlpin, J. G.; Chen, J. Y. C.; Rigsby, M. L.; Casey, W. H.; Britt, R. D.; Stahl,S. S. *J. Am. Chem. Soc.* **2011**, 133, 14431– 14442.

(12) Yeo, B. S.; Bell, A. T. *J. Am. Chem. Soc.* **2011**, 133, 5587– 5593.

(13) Liang, Y.; Li, Y.; Wang, H.; Zhou, J.; Wang, J.; Regier, T.; Dai, H. *Nat. Mater.* **2011**, 10, 780–786.

(14) Liao, M.; Feng, J.; Luo, W.; Wang, Z.; Zhang, J.; Li, Z.; Yu, T.; Zou, Z. *Adv. Funct. Mater.***2012**, 22, 3066– 3074.

(15) Hou, J.; Wang, Z.; Yang, C.; Cheng, H.; Jiao, S.; Zhu, H. *Energy Environ. Sci.* **2013**, 6,3322– 3330.

(16) Kent, C. A.; Concepción, J. J.; Dares, C. J.; Torelli, D. A.; Rieth, A. J.; Miller, A. S.; Hoertz, P. G.; Meyer, T. J. *J. Am. Chem. Soc.* **2013**, 135, 8432– 8435.

(17) Surendranath, Y.; Lutterman, D. A.; Liu, Y.; Nocera, D. G. *J. Am. Chem. Soc.* **2012**, 134,6326– 6336.

(18) Wee, T.-L.; Sherman, B. D.; Gust, D.; Moore, A. L.; Moore, T. A.; Liu, Y.; Scaiano, J. C. *J. Am. Chem. Soc.* **2011**, 133, 16742– 16745.

(19) Sa, Y. J.; Kwon, K.; Cheon, J. Y.; Kleitz, F.; Joo, S. H. *J. Mater. Chem. A* **2013**, 1, 9992–10001.

(20) Grewe, T.; Deng, X.; Weidenthaler, C.; Schüth, F. *Chem. Mater.* **2013**, 25, 4926–4935.

(21) Grewe, T.; Deng, X.; Tüysüz, H. *Chem. Mater.* **2014**, 26, 3162–3168.

(22) Jiao, F.; Frei, H. *Chem. Commun.* **2010**, 46, 2920– 2922.

(23) Jiao, F.; Frei, H. *Energy Environ. Sci.* **2010**, 3, 1018– 1027.

(24) Hara, M.; Waraksa, C. C.; Lean, J. T.; Lewis, B. A.; Mallouk, T. E. *J. Phys. Chem. A* **2000**,104, 5275– 5280.

(25) Boppana, V. B. R.; Jiao, F. *Chem. Commun.* **2011**, 47, 8973–8975.

(26) Iyer, A.; Del-Pilar, J.; King'ondu, C. K.; Kissel, E.; Garces, H. F.; Huang, H.; El-Sawy, A. M.; Dutta, P. K.; Suib, S. L. *J. Phys. Chem. C* **2012**, 116, 6474– 6483.

(27) Wei, J.; Liu, Y.; Ding, Y.; Luo, C.; Du, X.; Lin, J. *Chem. Commun.* **2014**, 50, 11938–11941.

(28) Yamada, Y.; Yano, K.; Hong, D.; Fukuzumi, S. *Phys. Chem. Chem. Phys.* **2012**, 14, 5753–5760.

(29) Najafpour, M. M.; Ehrenberg, T.; Wiechen, M.; Kurz, P. *Angew. Chem., Int. Ed.* **2010**, 49,2233– 2237.

(30) Conrad, F.; Bauer, M.; Sheptyakov, D.; Weyeneth, S.; Jaeger, D.; Hametner, K.; Car, P.-E.; Patscheider, J.; Günther, D.; Patzke, G. R. *RSC Adv.* **2012**, 2, 3076–3082.

(31) Shevchenko, D.; Anderlund, M. F.; Thapper, A.; Styring, S. *Energy Environ. Sci.* **2011**, 4,1284– 1287.

(32) Gardner, G. P.; Go, Y. B.; Robinson, D. M.; Smith, P. F.; Hadermann, J.; Abakumov, A.; Greenblatt, M.; Dismukes, G. C. *Angew. Chem., Int. Ed.* **2012**, 51, 1616–1619.

(33) Hong, D.; Yamada, Y.; Nagatomi, T.; Takai, Y.; Fukuzumi, S. *J. Am. Chem. Soc.* **2012**, 134,19572– 19575.

(34) Yin, Q.; Tan, J. M.; Besson, C.; Geletti, Y. V.; Musaev, D. G.; Kuznetsov, A. E.; Luo, Z.; Hardcastle, K. I.; Hill, C. L. *Science* **2010**, 328, 342–345.

(35) Huang, Z.; Luo, Z.; Geletii, Y. V.; Vickers, J. W.; Yin, Q.; Wu, D.; Hou, Y.; Ding, Y.; Song, J.; Musaev, D. G.; Hill, C. L.; Lian, T. *J. Am. Chem. Soc.* **2011**, 133, 2068–2071.

(36) Vickers, J. W.; Lv, H.; Sumliner, J. M.; Zhu, G.; Luo, Z.; Musaev, D. G.; Geletii, Y. V.; Hill, C. L. *J. Am. Chem. Soc.* **2013**, 135, 14110– 14118.

(37) Lv, H.; Song, J.; Geletii, Y. V.; Vickers, J. W.; Sumliner, J. M.; Musaev, D. G.; Kögerler, P.; Zhuk, P. F.; Bacsa, J.; Zhu, G.; Hill, G. L. *J. Am. Chem. Soc.* **2014**, 136, 9268–9271.

(38) Stracke, J. J.; Finke, R. G. *J. Am. Chem. Soc.* **2011**, 133, 14872–14875.

(39) Stracke, J. J.; Finke, R. G. *ACS Catal.* **2014**, 4, 79– 89.

(40) Hong, D.; Jung, J.; Park, J.; Yamada, Y.; Suenobu, T.; Lee, Y.-M.; Nam, W.; Fukuzumi, S.*Energy Environ. Sci.* **2012**, 5, 7606– 7616.

(41) Zidki, T.; Zhang, L.; Shafirovich, V.; Lymar, S. V. *J. Am. Chem. Soc.* **2012**, 134, 14275–14278.

(42) McCool, N. S.; Robinson, D. M.; Sheats, J. E.; Dismukes, G. C. *J. Am. Chem. Soc.* **2011**,133, 11446– 11449.

(43) Berardi, S.; La Ganga, G.; Natali, M.; Bazzan, I.; Puntoriero, F.; Sartorel, A.; Scandola, F.; Campagna, S.; Bonchio, M. *J. Am. Chem. Soc.* **2012**, 134, 11104–11107.

(44) Jiao, F.; Frei, H. *Angew. Chem., Int. Ed.* **2009**, 48, 1841–1844.

(45) Grzelczak, M.; Zhang, J.; Pfrommer, J.; Hartmann, J.; Driess, M.; Antonietti, M.; Wang, X.*ACS Catal.* **2013**, 3, 383– 388.

(46) Yang, C.-C.; Eggenhusien, T. M.; Wolters, M.; Agiral, A.; Frei, H.; de Jongh, P. E.; de Jong,K. P.; Mul, G. *ChemCatChem.* **2013**, 5, 550– 556.

(47) Yusuf, S.; Jiao, F. *ACS Catal.* **2012**, 2, 2753– 2760.

(48) Rosen, J.; Hutchings, G. S.; Jiao, F. *J. Am. Chem. Soc.* **2013**, 135, 4516–4521.

(49) Zhang, Y.; Rosen, J.; Hutchings, G. S.; Jiao, F. *Catal. Today* **2014**, 225, 171–176.

(50) Ahn, H. S.; Yano, J.; Tilley, T. D. *Energy Environ. Sci.* **2013**, 6, 3080–3087.

(51) Del Pilar-Albaladejo, J.; Dutta, P. K. *ACS Catal.* **2014**, 4, 9– 15.

(52) Armandi, M.; Hernandez, S.; Vankova, S.; Zaranilli, S.; Boneli, B.; Garrone, E. *ACS Catal.* **2013**, 3, 1272– 1278.

(53) Zhao, J.; Zou, Y.; Zou, X.; Bai, T.; Liu, Y.; Gao, R.; Wang, D.; Li, G.-D. *Nanoscale* **2014**, 6,7255– 7262.

(54) Zhou, L.-J.; Zou, Y.; Li, G.-D.; Zou, X.; Zhao, J.; Fan, M.; Liu, Y.; Wang, D. *RSC Adv.* **2014**,4, 22951– 22954.

(55) Soo, H. S.; Agiral, A.; Bachmeier, A.; Frei, H. *J. Am. Chem. Soc.* **2012**, 134, 17104–17116.

(56) Agiral, A.; Soo, H. S.; Frei, H. *Chem. Mater.* **2013**, 25, 2264– 2273.

(57) Mavros, M. G.; Tsuchimochi, T.; Kowalczyk, T.; McIsaac, A.; Wang, L.-P.; Van Voorhis, T.*Inorg. Chem.* **2014**, 53, 6386– 6397.

(58) Kwapien, K.; Piccinin, S.; Fabris, S. *J. Phys. Chem. Lett.* **2013**, 4, 4223–4230.

(59) Chen, J.; Selloni, A. *J. Phys. Chem. Lett.* **2012**, 3, 2808– 2814.

(60) Luisetto, I.; Pepe, F.; Bemporad, E. *J. Nanopart. Res.* **2008**, 10, 59– 67.

(61) Meng, Y.; Chen, D.; Jiao, X. *J. Phys. Chem. B* **2006**, 110, 15212–15217.

(62) Deng, Y.; Qi, D.; Deng, C.; Zhang, X.; Zhao, D. *J. Am. Chem. Soc.* **2008**, 130, 28–29.

(63) Deng, Y.; Cai, Y.; Sun, Z.; Liu, J.; Liu, C.; Wei, J.; Li, W.; Liu, C.; Wang, Y.; Zhao, D. *J. Am. Chem. Soc.* **2010**, 132, 8466– 8473.

(64) Choi, M.; Heo, W.; Kleitz, F.; Ryoo, R. *Chem. Commun.* **2003**, 1340–1341.

(65) Sharma, K. K.; Buckley, R. P.; Asefa, T. *Langmuir* **2008**, 24, 14306–14320.

(66) Xu, R.; Zeng, H. C. *Langmuir* **2004**, 20, 9780– 9790.

(67) Olguin, G.; Yacou, C.; Smart, S.; da Costa, J. C. D. *Sci. Rep.* **2013**, 3, 2449-1–5.

(68) Khodakov, A. Y.; Chu, W.; Fongarland, P. *Chem. Rev.* **2007**, 107, 1692–1744.

(69) Gillis, P.; Moiny, F.; Brooks, R. A. *Magn. Reson. Med.* **2002**, 47, 257–263.

(70) Pinho, S. L. C.; Pereira, G. A.; Voisin, P.; Kassem, J.; Bouchaud, V.; Etienne, L.; Peters, J. A.; Carlos, L.; Mornet, S.; Geraldes, C. F. G. C.; Rocha, J.; Delville, M.-H. *ACS Nano* **2010**, 4, 5339– 5349.

(71) Paquet, C.; de Haan, H. W.; Leek, D. M.; Lin, H.-Y.; Xiang, B.; Tian, G.; Kell, A.; Simard, B.*ACS Nano* **2011**, 5, 3104– 3112.

(72) Armstrong, J. K.; Wenby, R. B.; Meiselman, H. J.; Fisher, T. C. *Biophys. J.* **2004**, 87, 4259–4270.

(73) Dohmen, M. P. J.; Pereira, A. M.; Timmer, J. M. K.; Benes, N. E.; Keurentjes, J. T. F. *J. Chem. Eng. Data* **2008**, 53, 63– 65.

(74) Díaz, U.; García, T.; Velty, A.; Corma, A. *J. Mater. Chem.* **2009**, 19, 5970–5979.

(75) Williams, E. A. In *The Chemistry of Organic Silicon Compounds*; Patai, S.; Rappoport, Z., Eds.; John Willey & Sons: New York, **1989**; p 511.

(76) Uhlig, F.; Marsmann, H. C. In *Gelest Catalog: Silicon Compounds, Silanes & Silicones*, 2nd ed.; Arkles, B.; Larson, G., Eds.; Gelest: Morrisville, PA, **2008**; p 208.

(77) Jena, D.; Konar, A. *Phys. Rev. Lett.* **2007**, 98, 136805.

(78) Konar, A.; Fang, T.; Jena, D. *Phys. Rev. B* **2010**, 82, 115452.

(79) Hollander, M. J.; LaBella, M.; Hughes, Z. R.; Zhu, M.; Trumbull, K. A.; Cavalero, R.; Snyder,D. W.; Wang, X. J.; Hwang, E.; Datta, S.; Robinson, J. A. *Nano Lett.* **2011**, 11, 3601–3607.

CHAPTER 3.

METAL OXIDE DEOXYSILYLATION: A GENERALIZED ROUTE FOR THE SINGLE POT SYNTHESIS AND ENCAPSULATION OF CHALCOGENIDE AND PNICTIDE NANOCRYSTALS

A manuscript submitted to *Chem. Mater*.

Chia-Cheng Lin,[‡] Shannon Junle Tan,[†] Javier Vela[*]

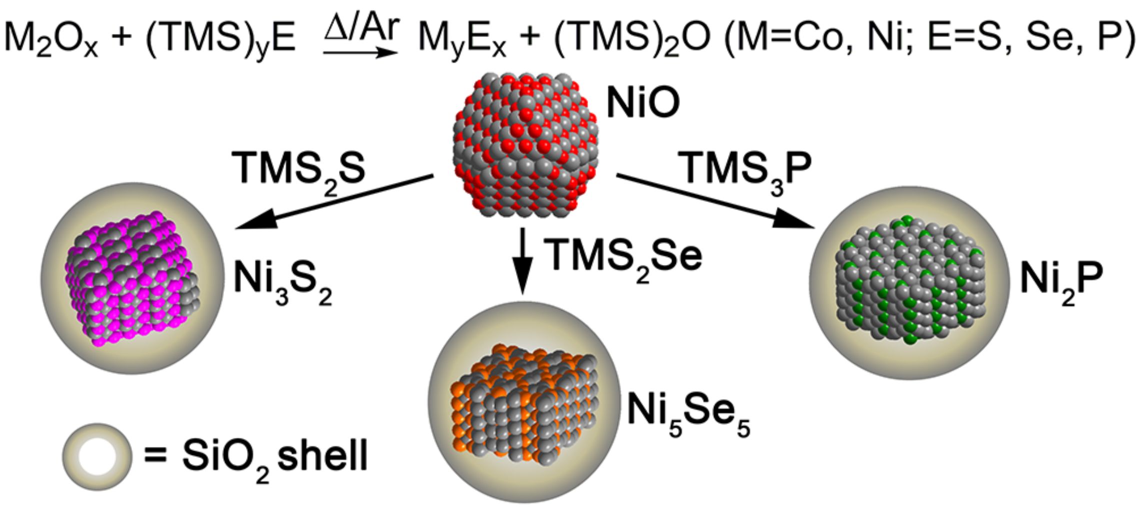

Abstract

Transition metal chalcogenides and pnictides are known catalysts for hydrogen evolution and hydrotreating reactions (hydrodesulfurization, hydrodeoxygenation, hydrodenitrification). To improve their stability and recyclability, low dimensional (nanostructured) versions of these compounds are often supported in porous silica or another

---

[‡] Primary researcher and author
[†] Contributed to synthesis of Co_9S_8 at higher temperature
[*] Author for correspondence

high surface oxide material. Here, we present a generalized synthetic route for transforming preformed metal oxide nanocrystals into chalcogenide (sulfides, selenides) or pnictide nanocrystals *via* deoxysilylation with highly reactive main group trimethylsilyl reagents. Nanocrystalline phases produced in this way include Ni_3S_2, Ni_5Se_5, Ni_2P, Co_9S_8, Co_3Se_4, CoP, Co_2P and $Ni_xCo_yS_8$ ($x + y = 9$). Nickel and cobalt chalcogenide nanocrystals produced by deoxysilylation are hollow, likely as a consequence of differential ion diffusion rates between the reactant and product phases (Kirkendall effect). Nickel and cobalt phosphides produced by deoxysilylation do not have such voids, likely due to the higher temperatures required for deoxysilylation. In all deoxysilylation reactions studied, simultaneous formation of an amorphous silica layer produces chalcogenide and pnictide nanocrystals that are already protected against sintering and degradation.

Introduction

Transition metal chalcogenides and pnictides continue to attract much research interest due to their interesting catalytic and opto-electronic properties and applications.[1] In particular, transition metal sulfides and phosphides are active catalysts for the upgrading of both conventional and bio-derived oils through hydrodesulfurization (HDS), hydrodeoxygenation (HDO), and hydrodenitrification (HDN) reactions.[2] Specific examples include silica-supported Ni_2P and Co_2P for HDO.[3,4] Metal phosphides also have excellent performance in HDS and HDN reactions,[5] with the most active Ni_2P catalysts having comparable activity to the industrial Ni-Mo-S catalysts currently in use.[6]

Besides having excellent hydrotreating properties, transition metal chalcogenides and phosphides are active catalysts for the electrolysis of water. Late transition metal sulfides are used for electrochemical oxygen evolution.[7,8] FeS_2,[9] $CoSe_2$,[10,11] Co_9S_8,[12] MoS_2,[13] CoP[14] and Ni_2P[15] have been utilized for electrochemical hydrogen evolution. Ni_7S_6 has selective chloronitrobenzene hydrogenation activity.[16] Furthermore, metal sulfides[17] and phosphides are employed in lithium ion batteries,[18] alkaline aqueous batteries, solar cells,[19] and in other electro-optical devices and applications.[1]

To fully understand and utilize the properties of metal chalcogenides and pnictides, efforts have been devoted to developing synthetic strategies that can generate nanoscale versions of these materials with controlled phase, morphology and size. Currently, transition metal chalcogenides and phosphides are most often made by chemical vapor deposition,[20-21] hydrogen plasma reduction,[22] metal phosphate reduction,[23] reaction of metal chlorides with phosphorous,[24-26] and from solution phase decomposition of suitable molecular precursors, including metal-trioctylphosphine complexes[27-30] and metal carbonyl- or acetylacetonate-alkyl phosphine and phosphide complexes.[31-39]

Treatment of preformed metals and metal oxides with elemental sulfur and phosphorus, or with alkyl sulfides and phosphines also yields metal sulfides[40-44] and phosphides.[45-48] Subsequently, these catalytic materials are often immobilized onto a high surface area, porous solid support in order to increase their stability and recyclability. Silica is a common support that features increased performance, as demonstrated recently for metal phosphides[49] such as Pd_5P_2[50] or Ni_2P on silica supports.[51-53]

Defluoro- and deoxysilylation reactions are often used in the synthesis and deprotection of molecular inorganic and organic compounds.[54] For example, they have been used in stoichiometric and catalytic C-F bond activation and hydrodefluorination reactions.[55-57] These reactions are driven by the formation of very strong Si-X bonds between silicon and a highly electronegative element, such as F (Si-F, 576 kJ/mol) or O (Si-O, 800 kJ/mol).[58] Here, we explore the use of deoxysilylation reactions between preformed metal oxide nanocrystals and trimethylsilyl precursors (TMS_xE, where TMS = Me_3Si and $_xE$ = $_2S$, $_2Se$, $_3P$) in order to synthesize nanocrystalline metal chalcogenides and phosphides (Scheme 1). Parallel in situ decomposition of excess trimethylsilyl precursors create a protecting silica shell around the newly formed nanocrystals. Thus, this new methodology results in silica-immobilized, high surface area metal chalcogenide and phosphide nanocrystals in a simple, one pot synthetic process.

Scheme 1. Metal oxide deoxysilylation.

$$M_2O_x + (TMS)_yE \xrightarrow{\Delta/Ar} M_yE_x + (TMS)_2O \text{ (M=Co, Ni; E=S, Se, P)}$$

Results and Discussion

Deoxysilylation of bare metal oxide nanocrystals: NiO. We began our investigation with cubic, rock salt NiO nanocrystals made by the thermal decomposition of nickel(II) oxalate (see Experimental). Deoxysilylation of NiO with TMS_2S in trioctylphosphine (TOP) at 130 °C under Ar for 20 h (equation 1) results in a noticeable color change from light gray to black, which is roughly consistent with the appearance of a broad hump between 400-1000 nm in the absorption spectrum (Figure 1a). The powder X-ray diffraction (XRD) pattern of the product of this reaction is consistent with the formation of Ni_3S_2 (Figure 1). The average Ni_3S_2 single crystalline domain size calculated from XRD peak widths using the Scherrer equation is 13 ± 3 nm, which would appear to consistent with the 14.1 ± 0.4 nm size observed for the original NiO nanocrystals (Table 1). However, transmission electron microscopy (TEM) and high-angle annular dark-field scanning transmission electron microscopy (HAADF-STEM) show that the newly formed Ni_3S_2 nanocrystals possess a distinct hollow morphology, with an average particle diameter 36 ± 7 nm and an average "shell" thickness of 8 ± 2 nm (Figure 2c).

$$\mathrm{NiO + TMS_2S \xrightarrow[TOP]{\Delta\ /\ Ar} Ni_3S_2/SiO_2} \tag{1}$$

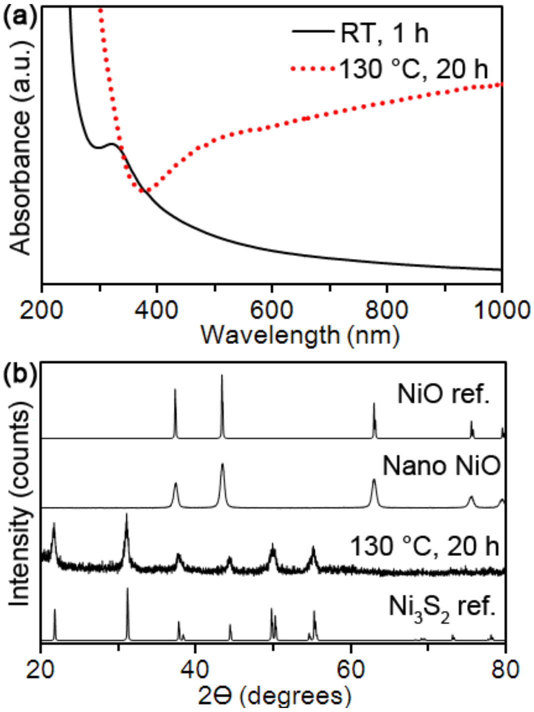

Figure 1. Solution-phase optical absorption spectra (a) and powder XRD patterns of NiO nanocrystals and their deoxysilylation product upon reaction with TMS_2S (reported XRD patterns for bulk rock salt NiO and heazlewoodite Ni_3S_2 are shown for comparison).

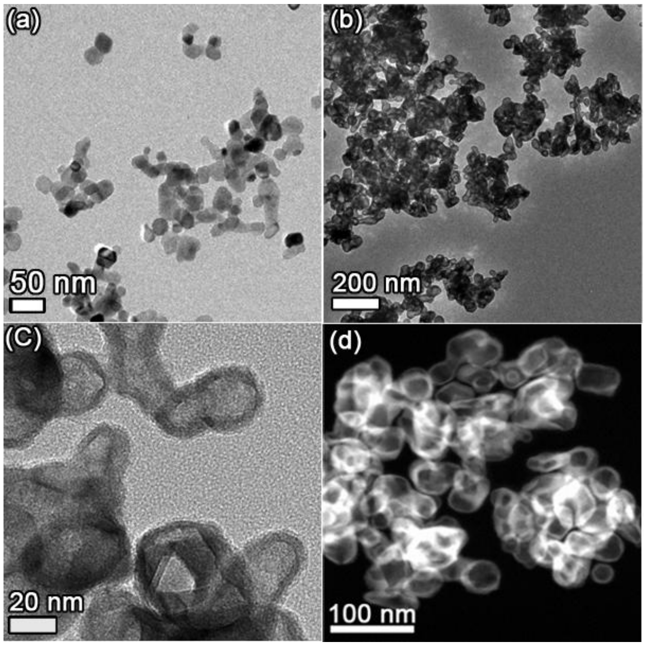

Figure 2. Representative bright field TEM images of NiO (a) and its deoxysilylation product with TMS_2S, Ni_3S_2 (b, c), and HAADF-STEM image of the latter (d).

Formation of vesicle-like nanoparticles is consistent with the Kirkendall effect.[15,27,28,34,40,42,46,48,64-67] Reactions at solid liquid interfaces are known to be affected by the relative diffusion rates of the different atoms or ions involved. When the diffusion rate of the reacting (“inner”) material (NiO) is greater than that of the newly produced (“outer”) material (Ni_3S_2), this results in a net outward mass flow accompanied by an inward void or “vacancy” flow. Here, it is reasonable to assume that the smaller oxide anion (O^{2-}) diffuses out of the reacting nanocrystal and onto its surface much faster than does the heavier and larger sulfide anion (S^{2-}) going into the new forming lattice.[46] Furthermore, the highly oxophilic Si center in TMS_2Si is expected to act as an avid oxide sponge at the surface of the original NiO nanoparticles, accelerating the outward mass flow.

Deoxysilylation of NiO nanocrystals with TMS_2Se in TOP at 130 °C under Ar for 20 h (equation 2) results in a color change from light gray to black (Figure 3a). Powder XRD data of the reaction product reveal the formation of small, 7 ± 2 Ni_5Se_5 nanocrystals, along with some residual NiO (Figure 3b). Electron microscopy shows the resulting Ni_5Se_5 particles are also hollow, with average size and shell thickness of 36 ± 7 nm and 7 ± 2 nm, respectively (Figure 4). As in the sulfide case, these hollow Ni_5Se_5 particles appear to form due to an ion diffusion rate differential or Kirkendall mechanism.

$$\mathrm{NiO} + \mathrm{TMS_2Se} \xrightarrow[\mathrm{TOP}]{\Delta\ /\ \mathrm{Ar}} \mathrm{Ni_5Se_5/SiO_2} \qquad (2)$$

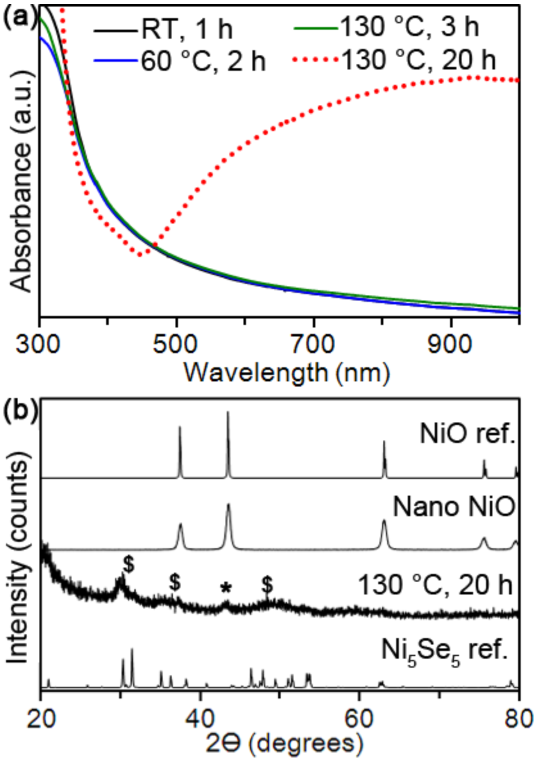

Figure 3. Solution-phase optical absorption spectra (a) and powder XRD patterns of NiO nanocrystals and their deoxysilylation product upon reaction with TMS_2Se (reported XRD patterns for bulk rock salt NiO (*) and Ni_5Se_5 ($) are shown for comparison).

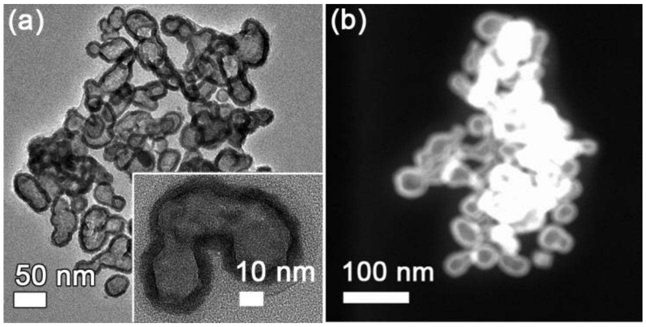

Figure 4. Representative bright field TEM (a) and HAADF-STEM (b) images of Ni_5Se_5 nanocrystals produced by deoxysilylation of NiO with TMS_2Se (inset shows a magnified image of one hollow particle).

Deoxysilylation of NiO nanocrystals with TMS_3P in TOP at 250 °C under Ar for 17 h (equation 3) results in a color change from light gray to dark gray, as evidenced by the appearance of a broad absorption between 500-900 nm (Figure 5a). Control experiments in the absence of TMS_3P unambiguously showed that TOP does NOT act as a source of phosphide under these exact reaction conditions. When TMS_3P was added, powder XRD and TEM analyses confirm the formation of "solid" (not void or hollow) Ni_2P nanocrystals with Scherrer and microscopy diameters of 11 ± 1 nm and 12 ± 2 nm (Figures 5b and 6). As in the previous two cases, TEM and HAADF-STEM reveal that the Ni_2P nanocrystals are embedded inside an amorphous silica matrix.

$$\mathrm{NiO} + \mathrm{TMS_3P} \xrightarrow[\mathrm{TOP}]{\Delta\ /\ \mathrm{Ar}} \mathrm{Ni_2P/SiO_2} \qquad (3)$$

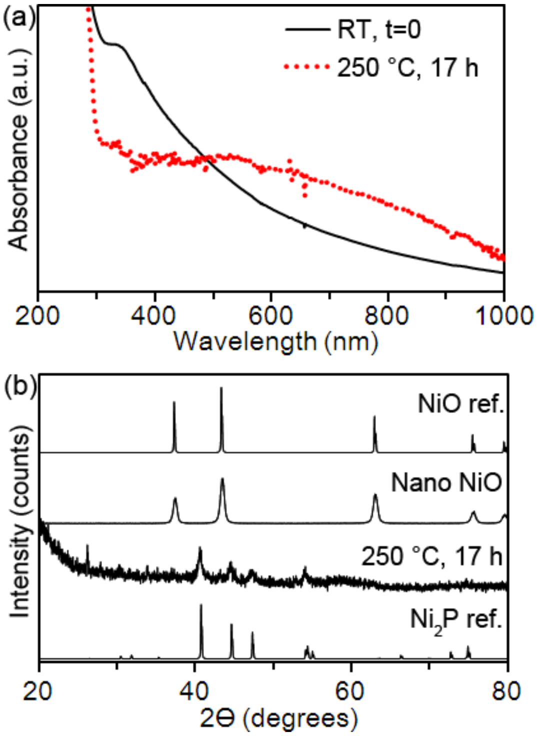

Figure 5. Solution-phase optical absorption spectra (a) and powder XRD patterns of NiO nanocrystals and their deoxysilylation product upon reaction with TMS_3P (reported XRD patterns for bulk rock salt NiO and Mn_2P-type Ni_2P are shown for comparison).

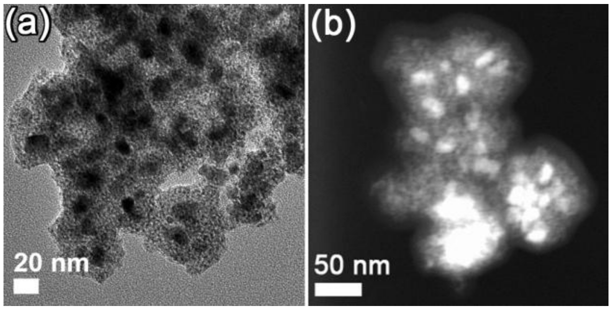

Figure 6. Representative bright field TEM (a) and HAADF-STEM (b) images of Ni_2P nanocrystals produced by deoxysilylation of NiO with TMS_3P.

The presence of voids in (hollow) nickel sulfide and selenide nanocrystals and the absence of similar voids in Ni_2P nanocrystals could be discussed in the context of several factors, including relative (an)ion charge, size, polarizability, temperature, and specific lattice entropy.[68] It is well known that diffusion of ions in solids increases as both ionic size and charge decrease. Thus, formation of voids in hollow nickel sulfides and selenides can be explained on the basis of the expected relative diffusion rates: $O^{2-} > S^{2-} > Se^{2-}$. However, the absence of voids in nickel phosphide is counterintuitive based on the expected relative diffusion rates: $O^{2-} > S^{2-} > P^{3-}$ (this would imply the nickel phosphide particles should have the most pronounced voids, which is not observed). The higher reaction temperatures required for deoxysilylation may explain the lack of voids in Ni_2P. Higher reaction temperatures could help minimize or cancel out any differential between the diffusion rates of both outward-bound O^{2-} ions and inward-bound P^{3-} across the solid-liquid interface. Alternatively, a higher reaction temperature could cause any initially formed (and otherwise observable) voids to collapse due to melting and coalescence of nanosized particles.[69] The higher reaction temperature may also be responsible for the formation of a much thicker, more distinct silica layer, due to increased thermal decomposition of excess trimethylsilyl reagent (when using TMS_3P *vs.* TMS_2S and TMS_2Se).

Deoxysilylation of bare cobalt oxide nanoparticles. Deoxysilylation of Co_3O_4 nanocrystals (17±4 nm by TEM) with TMS_2S in TOP at 130 °C under Ar for 25 h (equation 4) resulted in no significant color change (the reaction mixture remained black, see Supporting Information). Powder XRD and TEM data showed the sample consisted of a mixture of CoO and hollow Co_9S_8 nanocrystals with Scherrer sizes of 15 ± 1 nm and 5.9 ± 0.4 nm, respectively (see Supporting Information).

$$\mathrm{Co_3O_4 + TMS_2S \xrightarrow[TOP]{\Delta\ /\ Ar} CoO/Co_9S_8/SiO_2} \tag{4}$$

In contrast, deoxysilylation of CoO nanocrystals with TMS_2S in TOP at 130 °C under Ar for 20 h (equation 5) resulted in a color change from dark brown to black, as evidenced by the loss of the two 600 nm and 700 nm peaks in the solution-phase absorption spectrum (Figure 7a). Powder XRD shows the formation of Co_9S_8 with a small, 6 ± 1 nm average single crystalline domain (Scherrer) size, which is slightly smaller than that of the starting CoO nanocrystals (13 ± 2 nm). TEM indicates the Co_9S_8 nanocrystals are hollow. The average particle diameter is 20 ± 3 nm, and the average shell thickness is 5 ± 1 nm (in agreement with the aforementioned, single crystalline domain size observed by XRD).

$$\mathrm{CoO + TMS_2S \xrightarrow[TOP]{\Delta\ /\ Ar} Co_9S_8/SiO_2} \tag{5}$$

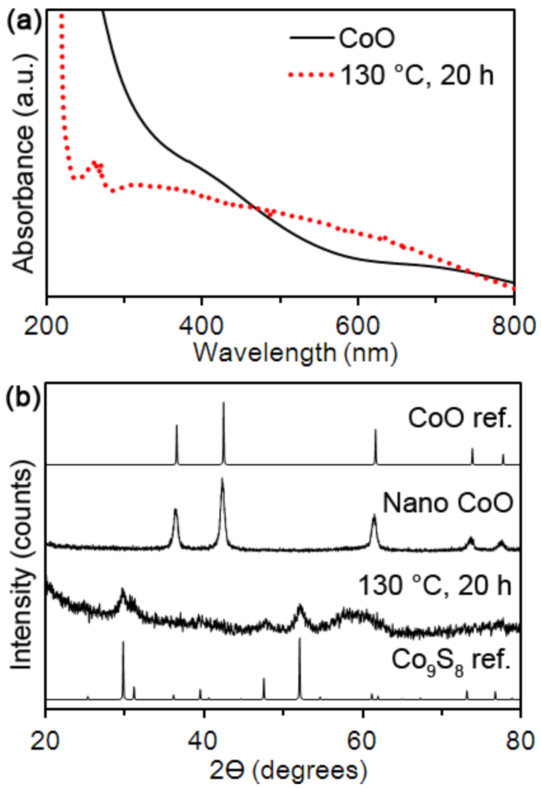

Figure 7. Solution-phase optical absorption spectra (a) and powder XRD patterns of CoO nanocrystals and their deoxysilylation product upon reaction with TMS_2S (reported XRD patterns for bulk rock salt CoO and cobaltpentlandite Co_9S_8 are shown for comparison).

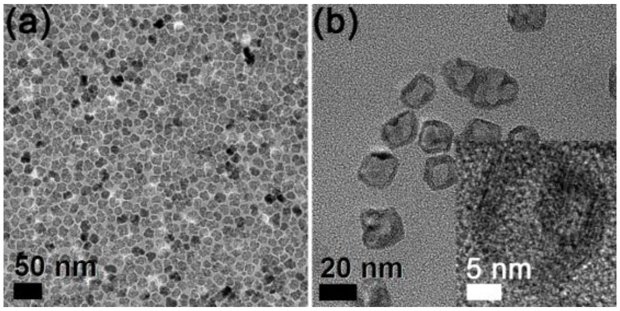

Figure 8. Representative TEM images of CoO (a) and Co_9S_8 nanocrystals (after the deoxysilylation with TMS_2S, b).

Similar to the sulfide case, deoxysilylation of Co_3O_4 nanocrystals with TMS_2Se in TOP at 130 °C under Ar (equation 6) did not result in a significant color change (black). Powder XRD analysis of the sample after 20 h also consists of both CoO and Co_3Se_4 nanocrystals with single crystalline domain (Scherrer) sizes of 15 ± 3 nm (which is close to that of the starting Co_3O_4, 17 ± 4 nm) and 2.8 nm, respectively. TEM images confirmed the hollow morphology of the $Co_3Se_4/CoO/SiO_2$ particles (see Supporting Information).

$$Co_3O_4 + TMS_2Se \xrightarrow[TOP]{\Delta / Ar} CoO/Co_3Se_4/SiO_2 \qquad (6)$$

Deoxysilylation of Co_3O_4 with TMS_3P in TOP at 250 °C under Ar for 17 h (equation 7) results in a color change from black to dark gray, as evidenced by the disappearance of the 500 nm and 800 nm absorption peaks (Figure 9) (at lower temperatures, only CoO is produced). Powder XRD peaks of the sample after 17 h match those of the bulk CoP reference with an estimated grain size of 6 ± 1 nm. As in the nickel case above, TEM and selected area electron diffraction pattern reveal the formation of solid (not hollow) CoP nanocrystals (11 ± 3 nm) embedded in an amorphous silica layer (Figure 10), the latter being likely due to accompanying thermal decomposition of excess silyl precursors to form an amorphous silica shell (see below). In contrast to the lower temperature sulfide and selenide reactions above, no CoO is observed here (CoO was observed when deoxysilylation with TMS_3P was conducted at a lower, 130 °C temperature, suggestion it may be an intermediate phase). Interestingly, low Co to P ratios yield CoP, while higher Co to P ratios yield a mixture of Co_2P, CoP, and some residual CoO (Figure 9b and Table 1). As in the nickel case above, no phosphide phase was observed in the absence of TMS_3P, demonstrating that TOP is not a source of phosphide under this set of reaction conditions.

$$Co_3O_4 + TMS_3P \xrightarrow[\text{TOP}]{\Delta\ /\ \text{Ar}} CoP/SiO_2 \qquad (7)$$

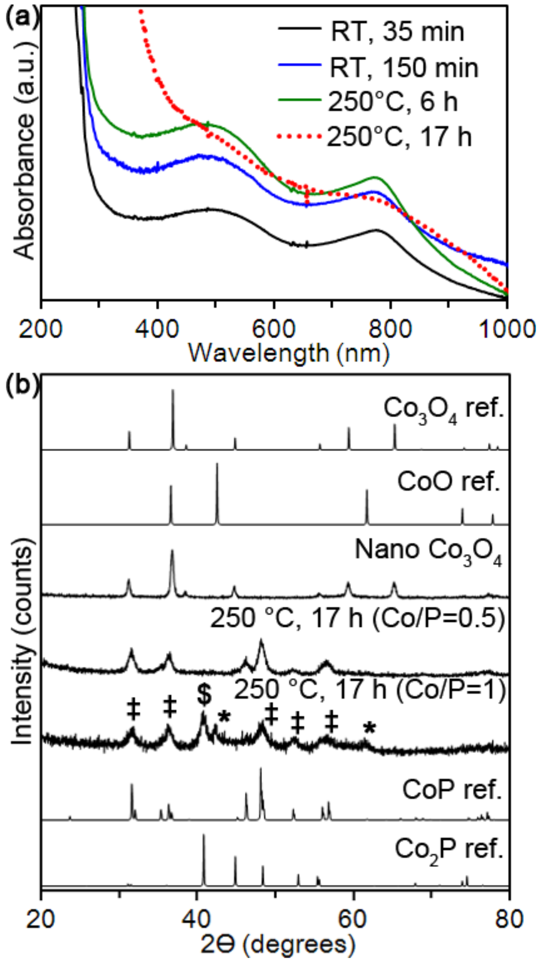

Figure 9. Solution-phase optical absorption spectra (a) and powder XRD patterns of CoO nanocrystals and their deoxysilylation product upon reaction with TMS_2S (reported XRD patterns for bulk rock salt CoO (*), MnP-type CoP (‡), and MnP-type Co_2P ($) are shown for comparison; also shown is the synthetic Co/P ratio, determined by dividing three times the chemical amount (in moles) of Co_3O_4 over that of TMS_3P).

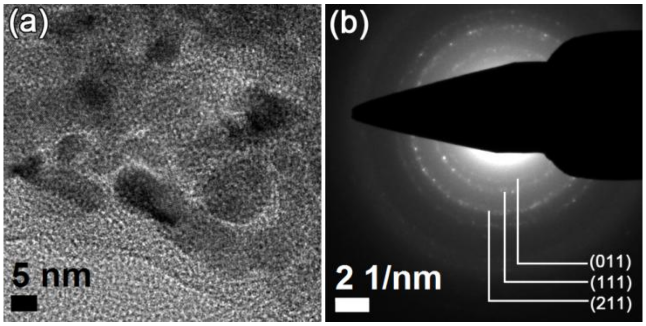

Figure 10. Representative TEM image (a) and selected area electron diffraction pattern (b) of CoP/SiO_2 nanocrystals produced by deoxysilylation of Co_3O_4 with TMS_3P.

Deoxysilylation of mixed metal oxide nanocrystals. Having established the generality of deoxysilylation reactions to nickel and cobalt oxide nanocrystals, we asked whether this reaction could also be applied to mixed metal oxides. We specifically questioned whether deoxysilylation would proceed at similar or different rates for certain metal ions, perhaps leading to phase segregation. To test this idea, we performed the deoxysilylation of $NiCo_2O_4$ nanocrystals with TMS_2S in TOP at 130 °C under Ar for 16 h (equation 8), which resulted in a color change from dark gray to black, as evidence by the loss of 500 nm and 800 nm peaks in the solution-phase absorption spectrum (Figure 11a). Powder XRD, TEM and HAADF-STEM data confirm the formation of hollow (Kirkendall) nanocrystals with general composition $Ni_xCo_yS_8$ ($x + y = 9$) (Figures 11b and 12). To gain a deeper insight into the composition of the product, we performed energy dispersive X-ray spectroscopy (EDS) mapping, which reveals Co (K- and L-edge), Ni (K- and L-edge) and S (K-edge) are distributed homogeneously across particles. EDS elemental analysis of different areas containing several nanocrystals showed the Co to Ni ratio varies between 8.2 and 5.3, suggesting that the product is Co-rich, which agrees with the two main mixed metal sulfide phases known $NiCo_8O_8$ and $Ni_3Co_6O_8$ (Figures 11b and 12, and Table 1)

$$\mathrm{NiCo_2O_4 + TMS_2S \xrightarrow[TOP]{\Delta\ /\ Ar} (Ni,\ Co)_9S_8/Si(} \qquad (8)$$

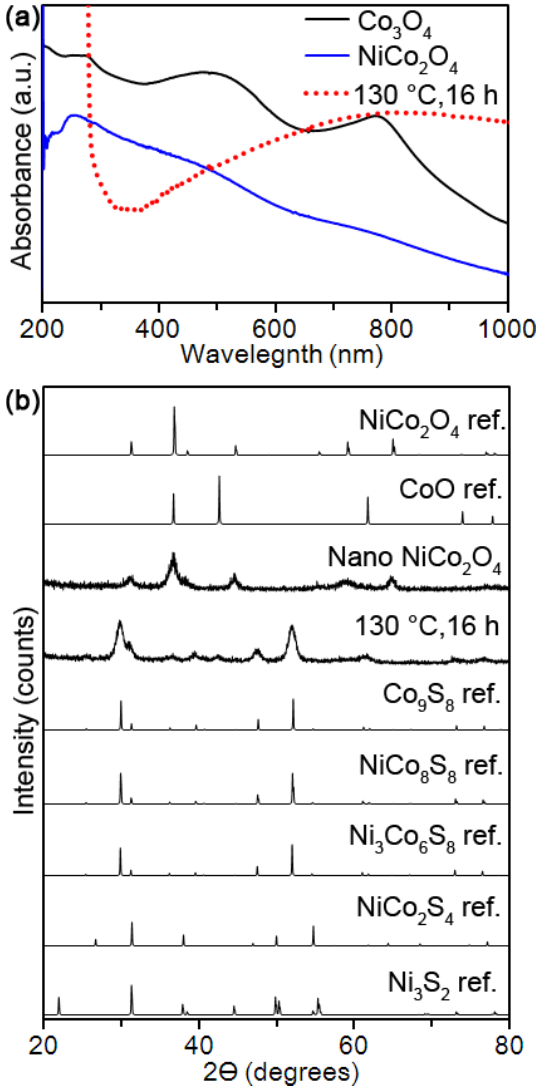

Figure 11. Solution-phase optical absorption spectra (a) and powder XRD patterns (b) of $NiCo_2O_4$ nanocrystals before and after deoxysilylation with TMS_2S (reported/standard data for several relevant oxides and sulfides are shown for comparison).

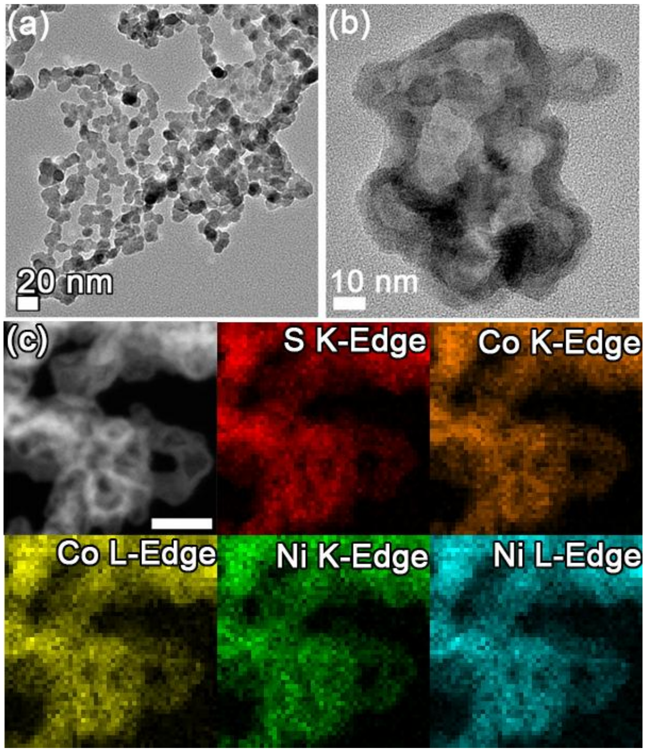

Figure 12. Representative TEM (a, b), and registered HAADF-STEM/EDS images (c) of $NiCo_2O_4$ nanocrystals (a) and its deoxysilylation product with TMS_2S (b, c) (the scale bar in c corresponds to 50 nm).

Concomitant formation of a silica shell. As noted above, in addition to their overall (hollow *vs.* solid) morphology, TEM of all sulfide, selenide and phosphide nanocrystals produced by deoxysilylation reveals the presence of a lower contrast layer surrounding the particles, which originates from decomposition of excess trimethylsilyl reagents into amorphous silica (SiO_2) (insets of Figures 4a, 8b, and Figures 2c, 6a, 10a, and 12b). ^{29}Si solid state (ss) NMR measurements on highly purified nanoparticles confirmed that this is due to the presence of a silica layer. For example, the ^{29}Si ssNMR spectra of Ni_3S_2/SiO_2 and Co_9S_8/SiO_2 show a broad hump around -100 ppm consistent with convoluted (partly merging) Q bands (Q^2, Q^3 and Q^4) (see Supporting Information available).[63]

Deoxysilylation of silica-coated metal oxides. We further tested the feasibility of performing deoxysilylation of nanocrystalline metal oxides that were already present in a protective silica matrix. NiO nanocrystals embedded in porous silica capsules ($NiO\subset SiO_2$) reacted with TMS_2S in TOP at 130 °C for 70 h (equation 9) to give a mixture of Ni_3S_2 and Ni_9S_8 (see Supporting Information).

$$NiO \subset SiO_2 + TMS_2S \xrightarrow[\text{TOP}]{\Delta\ /\ \text{Ar}} Ni_xS_y \subset SiO_2 \qquad (9)$$

Similarly, reaction of Co_3O_4/porous-SiO_2 core/shell nanoparticles with TMS_2S in TOP, as suggested by loss of the 500 nm and 800 nm peaks and appearance of a new hump in the optical absorption spectrum (Figure 14a). Powder XRD shows the formation of both CoO and Co_9S_8, in 3:7 ratio (Figure 14b and Table 1). The average particle sizes of CoO and Co_9S_8 calculated from the Scherrer equation are 10 ± 1 nm and 5.7 ± 0.3 nm, respectively. TEM confirmed the hollow structure of the product. Despite the presence of the residual (intermediate) CoO phase, this and the previous (Ni) results confirm that it is possible to transform nanocrystalline metal oxides to other phases through a pre-existing silica shell *via* deoxysilylation.

$$Co_3O_4/SiO_2 + TMS_2S \xrightarrow[\text{TOP}]{\Delta\ /\ \text{Ar}} CoO/Co_9S_8/SiO_2 \qquad (10)$$

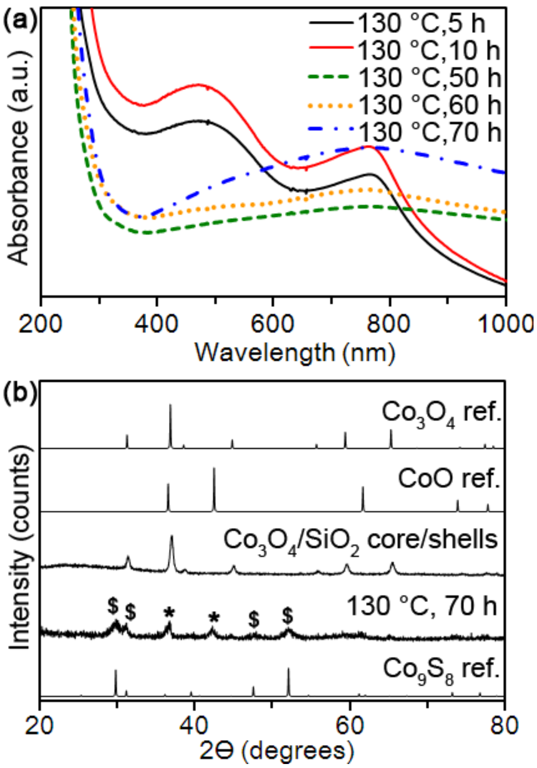

Figure 14. UV-Vis absorption spectra of aliquots during the deoxysilylation of Co_3O_4/SiO_2 with TMS_2S (Scheme 8) (a) and powder XRD data for Co_3O_4/SiO_2, product and bulk references. (The time refers to the overall reaction time.) (* = CoO, \$ = Co_9S_8.)

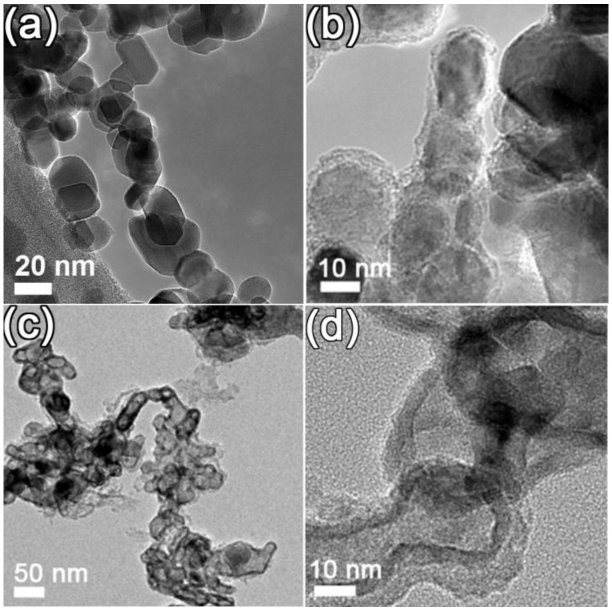

Figure 15. Representative TEM images of Co_3O_4 (a), Co_3O_4/porous-SiO_2 (3 nm-thick shell) (b), and its deoxysilylation product with TMS_2S, Co_9S_8/SiO_2 (c, d).

Conclusion

In summary, we have successfully shown the versatility of utilizing trimethylsily reagents (TMS_xE) to transform preformed, nanocrystalline metal oxides (NiO, Co_3O_4, CoO, and $NiCo_2O_4$) into nanocrystalline metal chalcogenides and pnictides. Nanocrystalline phases produced via this deoxysilylation reaction include Co_9S_8, Co_3Se_4, CoP, Co_2P, Ni_3S_2, Ni_5Se_5 and Ni_2P. Nanocrystalline chalcogenide (sulfides, selenides) resulting from deoxysilylation possess hollow, vesicle like morphologies, whereas the nanocrystalline pnictides (phosphides) are not. Hollow morphologies can be explained on the basis of the nanoscale Kirkendall effect, and arise from unbalanced ion diffusion rates between reactant and product phases. All nanocrystalline chalcogenides and pnictides produced by deoxysilylation are surrounded by amorphous silica shells, which can serve as protective layers against particle agglomeration and degradation. Successful deoxysilylation of the ternary, mixed metal oxide

$NiCo_2O_4$ with TMS_2S helps to demonstrate that deoxysilylation can be performed without phase segregation. Similarly, successful deoxysilylation of silica-encapsulated metal oxides demonstrates the potential for this reaction for use in catalyst recycling and regeneration protocols.

Experimental Section

Materials. Cobalt(II) acetylacetonate ($Co(acac)_2$), cobalt(II) acetate tetrahydrate ($(CH_3COO)_2Co \bullet 4H_2O$), Brij 58 (poly(ethylene glycol)hexadecyl ether), tetraethylorthosilicate ($Si(OC_2H_5)_4$, TEOS), hexamethyldisilazane ($(CH3)_3SiNHSi(CH_3)_3$, HMDS) and bis(trimethylsilyl) sulfide ($((CH_3)_3Si)_2S$, TMS_2S) were purchased from Sigma-Aldrich; methanol, ethanol (absolute, 200 proof), isopropanol (2-propanol), cyclohexane, aqueous ammonium hydroxide (28.54 wt%) and diethylamine from Fisher; nickel chloride hexahydrate ($NiCl_2 \bullet 6H_2O$), trioctylphosphine (TOP), bis(trimethylsilyl)selenide ($((CH_3)_2Si)_2Se$, TMS_2Se) and tris(trimethylsilyl)phosphine ($((CH_3)_3Si)_3P$, TMS_3P, 10 wt% in hexane) from Strem; oxalic acid from Alfa Aesar; oleylamine ($CH_3(CH_2)_7CH{=}CH(CH_2)_7CH_2NH_2$), hydrazine monohydrate ($N_2H_4 \bullet H_2O$) and sodium borohydride ($NaBH_4$, $\geq 98\%$) from Acros. All chemicals were used as received unless specified otherwise.

Synthesis. *NiO nanocrystals* were synthesized according to a slightly modified procedure involving the thermal decomposition of nickel(II) oxalate.[59] An ethanolic 0.3 M oxalic acid solution (25 mL) was gradually added to an ethanolic 0.3 M nickel(II) chloride solution (25 mL) at 50 °C, while stirring for 2 h. Nickel(II) oxalate was collected by concentration under vacuum at 80 °C. Heating nickel oxalate to 400 °C in air for 2 h yielded gray NiO nanocrystals. *$NiO \subset SiO_2$ nanocomposites* were prepared following a procedure we previously reported.[60] *$NiCo_2O_4$ nanocrystals*. A 0.2 M ethanolic solution of nickel(II) acetate (25 mL) was slowly added to a 0.4 M ethanolic solution of cobalt(II) acetate (25 mL). After 2 h of stirring, the transparent solution became cloudy. The solid was collected via vacuum filtration, and dried in an oven at 80 ℃. Heating nickel cobalt acetate to 400 ℃ in air and held for 2 h produced dark $NiCo_2O_4$ nanocrystals. *CoO nanocrystals* were prepared following a slightly modified reported procedure.[61] Briefly, cobalt(II) acetylacetonate (0.14 g, 0.54 mmol), de-ionized water (0.05 g, 2.78 mmol) and oleylamine (7.30 g, 27.3 mmol) were added to a single neck 100 mL round bottom flask connected to a condenser with a glass stopcock adapter. After purging the system with Ar for 20 min, the solution was heated to 210 ℃ for 1 h. After cooling to room temperature, particles were precipitated by adding excess methanol (several mL) and separated by centrifugation (5,000 rpm, 10 min). The solid (particles) was (were) redispersed in hexane and re-precipitated by adding excess amount of ethanol (several mL) followed by centrifugation (5,000 rpm, 10 min). This washing cycle was repeated three times. *Co_3O_4 nanocrystals* were prepared by a slightly modified procedure involving the thermal decomposition of cobalt(II) oxalate.[62] A solution of 0.3 M cobalt acetate in ethanol (50 mL) was heated to 50 ℃ for 30 min, followed by quick addition of oxalic acid (1.07 g, 11.9 mmol). After 2 h at 50 ℃, cobalt(II) oxalate was collected by concentration under vacuum at 80 ℃. Heating cobalt(II) oxalate powder to 400 ℃ in air for 2 h yielded Co_3O_4 nanocrystals. Porous Co_3O_4/SiO_2 core/shell nanoparticles (5 nm thick) were prepared followed a previously reported procedure.[63]

***Deoxysilylation with bis(trimethylsilyl)sulfide* (TMS$_2$S).** Deoxysilylation of metal oxide nanocrystals was performed in a Schlenk line under dry Ar at designated temperatures (see below). An oven-dried three-neck round bottom flask equipped with a PTFE-coated magnetic stir bar, a glass stopcock adapter and a condenser were cooled down and assembled inside a glovebox. Metal oxide nanocrystals (10 mg, 134-142 μmol), TMS_2S (0.1 mL, 0.47 mmol) and TOP (2 mL, 4.5 mmol) were added into the flask. After connecting it to the Schlenk line, the flask was evacuated under vacuum and refilled with Ar. The mixture was heated to 130 °C for at least 16 h. During reaction, aliquots (*ca.* 0.2 mL) were taken, washed by precipitation and redispersion cycles (see above), and the solid products were analyzed by XRD and optical absorption (below). *Deoxysilylation with bis(trimethylsilyl)selenide* (TMS_2Se). Deoxysilylation was performed under identical conditions as mentioned above for TMS_2S. *Deoxysilylation with tris(trimethylsilyl)phosphine* (TMS_3P). Deoxysilylation was performed under similar conditions as mentioned above for TMS_2S, except that, due to the increased reactivity of TMS_3P, all glassware had to be surface passivated. Briefly, the oven dried Schlenk tube was allowed to cool down under vacuum, and surface silanol groups were passivated by exposure to hexamethyldisilazane (HMDS) in a low-pressure chamber or desiccator.

Structural Characterization. *Powder X-ray diffraction* (XRD) data were measured using a Rigaku Ultima IV diffractometer with a Cu Kα radiation source (40 kV, 44 mA). Sample percent composition was determined using PowderCell 2.4 (PCW) refined against standard XRD patterns. *Nitrogen physisorption* was measured on a Micromeritics ASAP 2020 surface area and porosimetry system. Samples were degassed at 100 °C under vacuum overnight prior to the analysis. Surface area was calculated with the Brunauer-Emmett-Teller (BET) method in the relative pressure range of 0.005 to 0.25 of adsorption data. Pore size distribution was calculated with the Barret-Joyber-Halenda (BJH) method. *Transmission Electron Microscopy* (TEM) was measured on an FEI Tecnai G^2 F20 field emission scanning transmission electron microscope (S/TEM) at 200 kV (point-to-point resolution <0.25 nm, line-to-line resolution <0.10 nm).

Spectroscopic Characterization. Optical absorption spectra (UV-Vis) were collected with a photodiode-array Agilent 8453 UV−Vis spectrophotometer. Solid state NMR data were collected with a Bruker Avance II 600 spectrometer operating at 119.2 MHz for ^{29}Si equipped with a 4 mm Bruker MAS probe spinning at 10 KHz. ^{29}Si DP-MAS NMR spectra were recorded with a pulse width of 4 μs and a recycling delay of 1 min. ^{29}Si isotropic chemical shifts are referenced to TMS ($\delta = 0$ ppm).

Supporting Information

Table S1. Optoelectronic properties of select Ni and Co chalcogenides and pnictides.

Material	**Character**
NiO	Semiconducting (4.0 eV)[70]
Ni_3S_2	Metallic
Ni_5Se_5	unknown[a]
Ni_2P	Metallic
CoO	Semiconducting (3.4,[i] 4.5 eV[d])[71]
Co_3O_4	Semiconducting (2.13, 3.95 eV)[72]
Co_9S_8	Metallic
Co_9S_8	Metallic
Co_3Se_4	unknown[a]
CoP	Metallic
Co_2P	Metallic
$NiCo_2O_4$	Semiconducting (2.06, 3.63 eV)[73]
$Ni_xCo_yS_8$ $x+y = 9$	unknown[a]
[i] = indirect, [d] = direct	

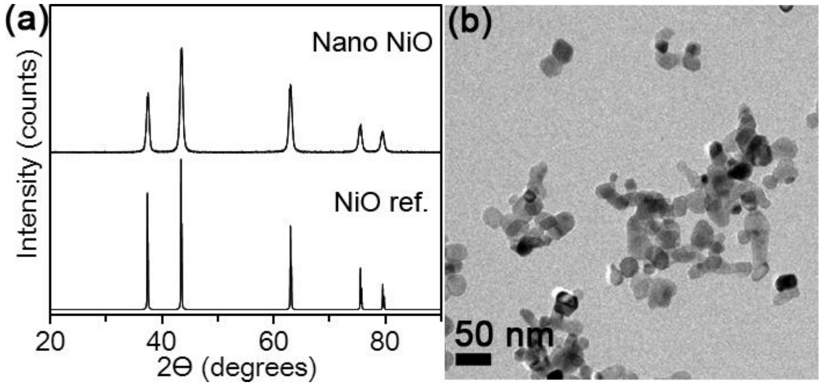

Figure S1. Powder XRD data for NiO nanocrystals (Scherrer: 14.1±0.4 nm), bulk NiO reference (a) and representative TEM image of NiO nanocrystals (18±4 nm) (b).

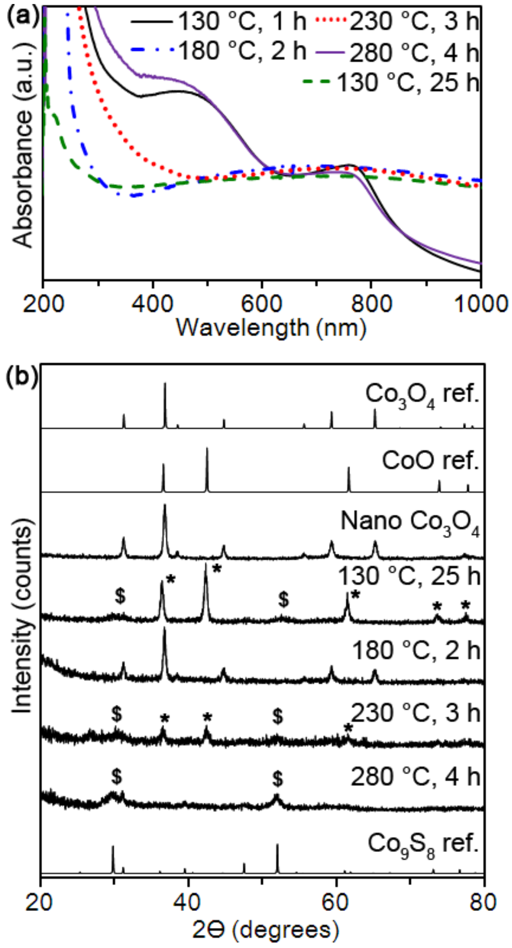

Figure S2. UV-Vis absorption spectra of aliquots during the reaction (a) and powder XRD data of Co_3O_4 nanocrystals, products the deoxysilylation of Co_3O_4 with TMS_2S (equation 4) and bulk references (b). (* = CoO, $ = Co_9S_8.)

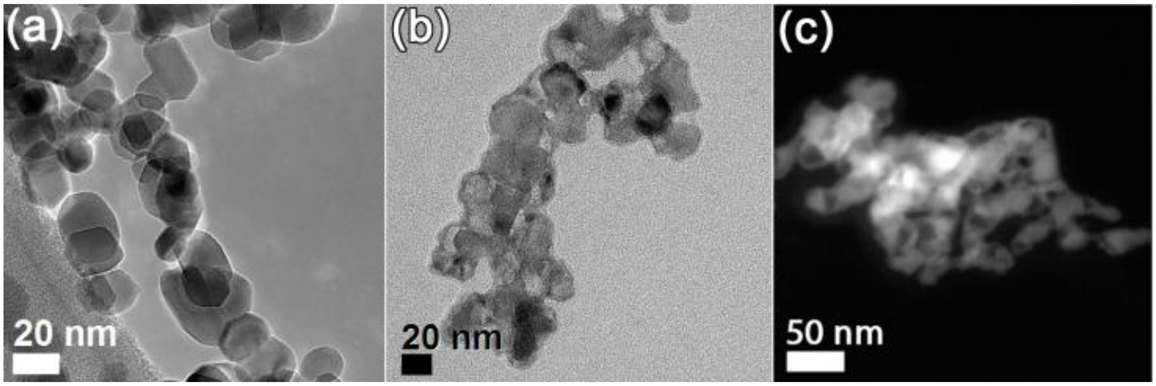

Figure S3. Representative TEM images of Co_3O_4 nanocrystals (a), bright field image (b) and HAADF-STEM image (c) of product after 25 h of deoxysilylation of Co_3O_4 with TMS_2S (equation 4).

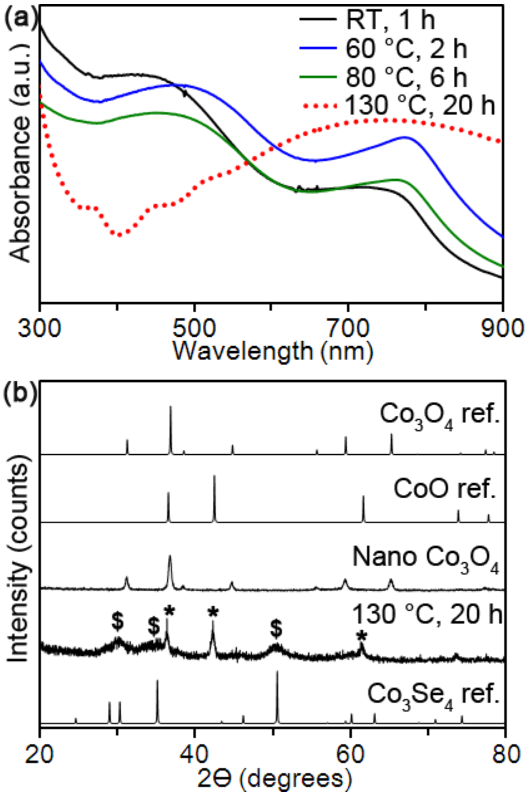

Figure S4. UV-Vis absorption spectra of aliquots during the deoxysilylation of Co_3O_4 with TMS_2Se (equation 6) reaction (a) and wide angle powder XRD data for Co_3O_4 nanocrystals, product after 20 h of reaction and bulk references (b). (* = CoO, $ = $MgAl_2O_4$ spinel-type Co_3Se_4.)

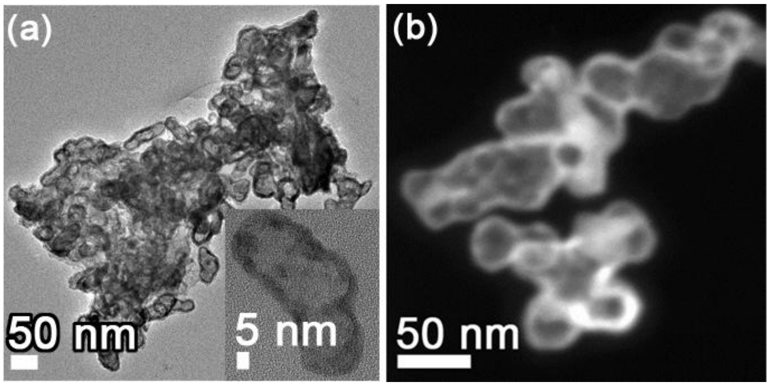

Figure S5. Representative TEM images of Co_3Se_4 nanocrystals after the deoxysilylation of Co_3O_4 with TMS_2Se (equation 6) (inset in (a) shows a high magnification image of one particle with hollow morphology) and HAADF-STEM image (b).

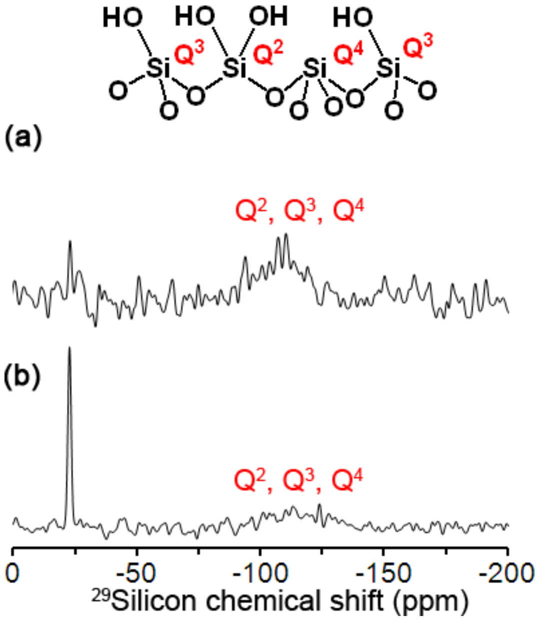

Figure S6. DP-MAS ^{29}Si NMR spectra of Co_9S_8 (a) and Ni_3S_2 (b).

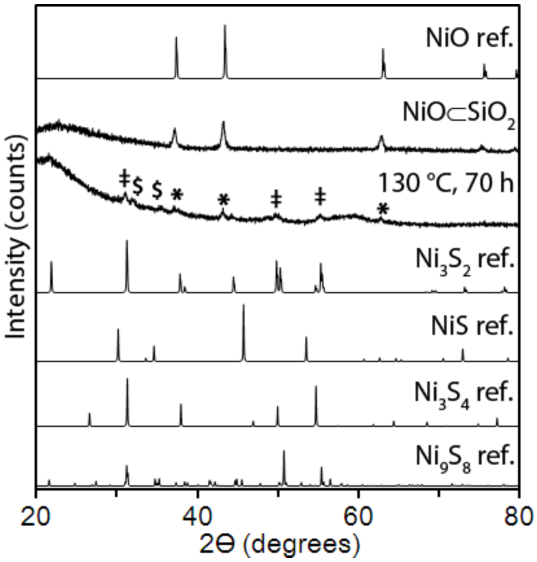

Figure S7. Powder XRD data for deoxysilylation of $NiO \subset SiO_2$ with TMS_2S (equation 9), product and bulk references. (* = NiO, ‡ = Ni_3S_2, $ = Ni_9S_8.)

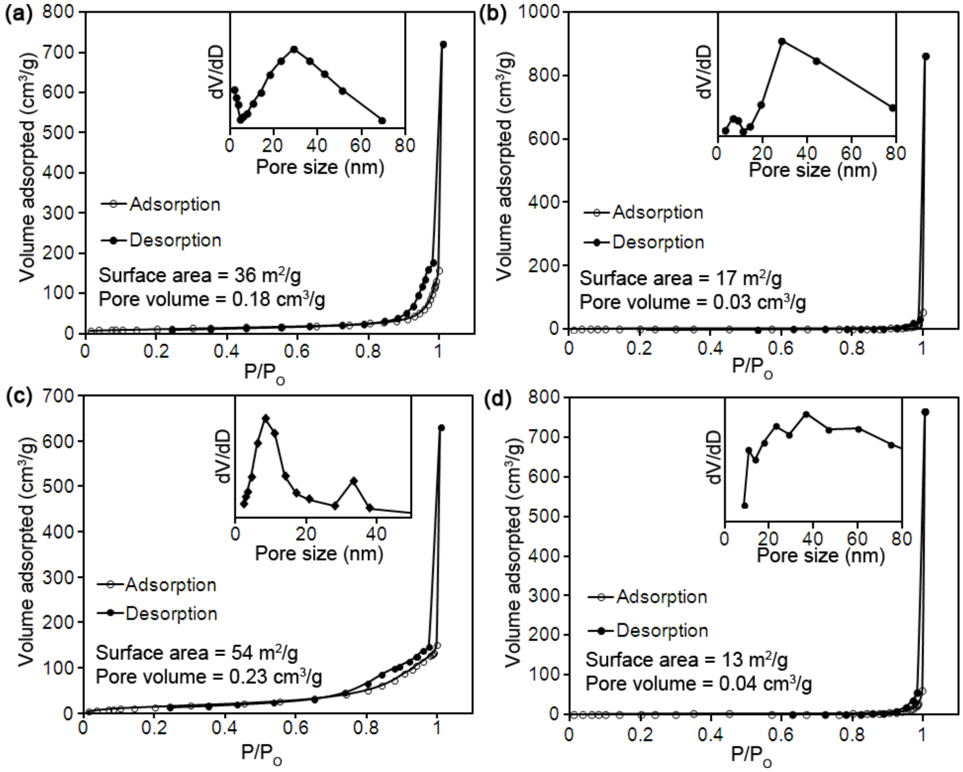

Figure S8. Nitrogen physisorption isotherms and BJH pore size distributions of NiO (a), Ni_3S_2 (b), CoO (c) and Co_9S_8 (d). The low surface area measurements indicate the resulting silica shells are not significantly porous.

Acknowledgment

We gratefully acknowledge the National Science Foundation for funding of this work through the Division of Materials Research, Solid State and Materials Chemistry program (NSF-DMR-1309510). The authors thank Bryan Rosales for comments.

References

(1) Carenco, S.; Portehault, D.; Boissière, C.; Mézailles, N.; Sanchez, C. Nanoscaled Metal Borides and Phosphides: Recent Developments and Perspectives. *Chem. Rev.* **2013**, *113*, 7981−8065.

(2) Prins, R.; Bussell, M. E. Metal Phosphides: Preparation, Characterization and Catalytic Reactivity. *Catal. Lett.* **2012**, *142*, 1413−1436.

(3) Zhao, H. Y.; Li, D.; Bui, P.; Oyama, S. T. Hydrodeoxygenation of Guaiacol as Model Compound for Pyrolysis Oil on Transition Metal Phosphide Hydroprocessing. Catalysts. *Appl. Catal., A* **2011**, *391*, 305–310.

(4) Wu, S.-K.; Lai, P.-C.; Lin, Y.-C.; Wan, H.-P.; Lee, H.-T.; Chang, H.-T. Atmospheric Hydrodeoxygenation of Guaiacol over Alumina-, Zirconia-, and Silica-Supported Nickel Phosphide Catalysts. *ACS Sustainable Chem. Eng.* **2013**, *1*, 349−358.

(5) Burns, A. W.; Layman, K. A.; Bale, D. H.; Bussell, M. E. Understanding the Relationship between Composition and Hydrodesulfurization Properties for Cobalt Phosphide Catalysts. *Appl. Catal., A* **2008**, *343*, 68–76.

(6) Oyama, T., S.; Gott, T.; Zhao, H.; Lee, Y.-K. Transition Metal Phosphide Hydroprocessing Catalysts: A Review. *Catal. Today* **2009**, *143*, 94–107.

(7) Gao, M. R.; Jiang, J.; Yu, S. H. Solution-Based Synthesis and Design of Late Transition Metal Chalcogenide Materials for Oxygen Reduction Reaction (ORR). *Small* **2012**, 8, 13–27.

(8) Sidik, R. A.; Anderson, A. B. Co_9S_8 as a Catalyst for Electroreduction of O_2: Quantum Chemistry Predictions. *J. Phys. Chem. B* **2006**, *110*, 936–941.

(9) Di Giovanni, C.; Wang, W.-A.; Nowak, S.; Grenèche, J.-M.; Lecoq, H.; Mouton, L.; Giraud, M.; Tard, C. Bioinspired Iron Sulfide Nanoparticles for Cheap and Long-Lived Electrocatalytic Molecular Hydrogen Evolution in Neutral Water. *ACS Catal.* **2014**, *4*, 681–687.

(10) Xu, Y.; Gao, M.; Zheng, Y.; Jiang, J.; Yu, S. Nickel/Nickel(II) Oxide Nanoparticles Anchored onto Cobalt(IV) Diselenide Nanobelts for the Electrochemical Production of Hydrogen. *Angew. Chem., Int. Ed.* **2013**, *33*, 8546−8550.

(11) Kong, D.; Wang, H.; Lu, Z.; Cui, Y. $CoSe_2$ Nanoparticles Grown on Carbon Fiber Paper: An Efficient and Stable Electrocatalyst for Hydrogen Evolution Reaction. *J. Am. Chem. Soc.* **2014**, *136*, 4897–4900.

(12) Sun, Y.; Liu, C.; Grauer, D. C.; Yano, J.; Long, J. R.; Yang, P.; Chang, C. J. Electrodeposited Cobalt-Sulfide Catalyst for Electrochemical and Photoelectrochemical Hydrogen Generation from Water. *J. Am. Chem. Soc.* **2013**, *135*, 17699−17702.

(13) Xie, J.; Zhang, J.; Li, S.; Grote, F.; Zhang, X.; Zhang, H.; Wang, R.; Lei, Y.; Pan, B.; Xie, Y. Controllable Disorder Engineering in Oxygen-Incorporated MoS_2 Ultrathin Nanosheets for Efficient Hydrogen Evolution. *J. Am. Chem. Soc.* **2013**, *135*, 17881–17888.

(14) Tian, J.; Liu, Q.; Asiri, A.; Sum, X. Self-Supported Nanoporous Cobalt Phosphide Nanowire Arrays: An Efficient 3D Hydrogen-Evolving Cathode over the Wide Range of pH 0−14. *J. Am. Chem. Soc.* **2014**, *136*, 7587–7590.

(15) Popczun, E. J.; McKone, J. R.; Read, C. G.; Biacchi, A. J.; Wiltrout, A. M.; Lewis, N. S.; Schaak, R. E. Nanostructured Nickel Phosphide as an Electrocatalyst for the Hydrogen Evolution Reaction. *J. Am. Chem. Soc.* **2013**, *135*, 9267−9270.

(16) Cao, F.; Lin, R. X.; Zhou, L.; Song, S. Y.; Lei, Y. Q.; Shi, W. D.; Zhao, F. Y.; Zhang, H. J. One-Pot Synthesis of Flowerlike Ni_7S_6 and its Application in Selective Hydrogenation of Chloronitrobenzene. *J. Mater. Chem.* **2010**, *20*, 1078−1085.

(17) Lai, C.-H.; Lu, M.-Y.; Chen, L.-J. Metal Sulfide Nanostructures: Synthesis, Properties and Applications in Energy Conversion and Storage. *J. Mater. Chem.* **2012**, *22*, 19–30.

(18) Yang, D.; Zhu, J.; Rui, X.; Tan, H.; Cai, R.; Hoster, H. E.; Yu, D. Y. W.; Hng, H. H.; Yan, Q. Synthesis of Cobalt Phosphides and Their Application as Anodes for Lithium Ion Batteries *ACS Appl. Mater. Interfaces* **2013**, *5*, 1093−1099.

(19) Chang, S.-H.; Lu, M.-D.; Tung, Y.-L.; Tuan, H.-Y. Gram-Scale Synthesis of Catalytic Co_9S_8 Nanocrystal Ink as a Cathode Material for Spray-Deposited, Large-Area Dye-Sensitized Solar Cells. *ACS Nano* **2013**, *7*, 9443−9451.

(20) Panneerselvam, A.; Malik, M., A; Afzaal, M.; O'Brien, P.; Helliwell, M. The Chemical Vapor Deposition of Nickel Phosphide or Selenide Thin Films from a Single Precursor. *J. Am. Chem. Soc.* **2008**, *130*, 2420–2421.

(21) Maneeprakorn, W.; Malik, M. A.; O'Brien, P. The Preparation of Cobalt Phosphide and Cobalt Chalcogenide (CoX, X = S, Se) Nanoparticles from Single Source Precursors. *J. Mater. Chem.* **2010**, *20*, 2329–2335.

(22) Wang, A. J.; Qin, M. L.; Guan, J.; Wang, L.; Guo, H. C.; Li, X.; Wang, Y.; Prins, R.; Hu, Y. K. The Synthesis of Metal Phosphides: Reduction of Oxide Precursors in a Hydrogen Plasma. *Angew. Chem., Int. Ed.* **2008**, *47*, 6052–6054.

(23) Stamm, K. L.; Garno, J. C.; Liu, G.-y.; Brock, S. L. A General Methodology for the Synthesis of Transition Metal Pnictide Nanoparticles from Pnictate Precursors and Its Application to Iron-Phosphorus Phases. *J. Am. Chem. Soc.* **2003**, *125*, 4038–4039.

(24) Xie, Y.; Su, H. L.; Qian, X. F.; Liu, X. M.; Qian, Y. T. A Mild One-Step Solvothermal Route to Metal Phosphides (Metal = Co, Ni, Cu). *J. Solid State Chem.* **2000**, *149*, 88−91.

(25) Barry, B. M.; Gillan, E. G. A General and Flexible Synthesis of Transition-Metal Polyphosphides *via* PCl_3 Elimination. *Chem. Mater.* **2009**, *21*, 4454−4461.

(26) Carenco, S.; Hu, Y.; Florea, I.; Ersen, O.; Boissière, C.; Mézailles, N.; Sanchez, C. Metal-Dependent Interplay between Crystallization and Phosphorus Diffusion during the Synthesis of Metal Phosphide Nanoparticles. *Chem. Mater.* **2012**, *24*, 4134−4145.

(27) Henkes, A. E.; Vasquez, Y.; Schaak, R. E. Converting Metals into Phosphides: A General Strategy for the Synthesis of Metal Phosphide Nanocrystals. *J. Am. Chem. Soc.* **2007**, *129*, 1896–1897.

(28) Chiang, R. K.; Chiang, R. T. Formation of Hollow Ni_2P Nanoparticles Based on the Nanoscale Kirkendall Effect. *Inorg. Chem.* **2007**, *46*, 369–371.

(29) Park, J.; Koo, B.; Hwang, Y.; Bae, C.; An, K.; Park, J.-G.; Park, H. M.; Hyeon, T. Novel Synthesis of Magnetic Fe_2P Nanorods from Thermal Decomposition of Continuously Delivered Precursors Using a Syringe Pump. *Angew. Chem., Int. Ed.* **2004**, *43*, 2282−2285.

(30) Park, J.; Koo, B.; Yoon, K.-Y.; Hwang, Y.; Kang, M.; Park, J.-G.; Hyeon, T. Generalized Synthesis of Metal Phosphide Nanorods via Thermal Decomposition of Continuously Delivered Metal-Phosphine Complexes Using a Syringe Pump. *J. Am. Chem. Soc.* **2005**, *127*, 8433−8440.

(31) Qian, C.; Kim, F.; Ma, L.; Tsui, F.; Yang, P.; Liu, J. Solution-Phase Synthesis of Single-Crystalline Iron Phosphide Nanorods/Nanowires. *J. Am. Chem. Soc.* **2004**, *126*, 1195−1198.

(32) Gregg, K. A.; Perera, S. C.; Lawes, G.; Shinozaki, S.; Brock, S. L. Controlled Synthesis of MnP Nanorods: Effect of Shape Anisotropy on Magnetization. *Chem. Mater.* **2006**, *18*, 879−886.

(33) Wang, J.; Johnston-Peck, A. C.; Tracy, J. B. Nickel Phosphide Nanoparticles with Hollow, Solid, and Amorphous Structures. *Chem. Mater.* **2009**, *21*, 4462–4467.

(34) Muthuswamy, E.; Savithra, G. H. L.; Brock, S. L. Synthetic Levers Enabling Independent Control of Phase, Size, and Morphology in Nickel Phosphide Nanoparticles. *ACS Nano* **2011**, *5*, 2402–2411.

(35) Mandel, K.; Dillon, F.; Koos, A. A.; Aslam, Z.; Jurkschat, K.; Cullen, F.; Crossley, A.; Bishop, H.; Moh, K.; Cavelius, C.; Arzt, E.; Grobert, N. Facile, Fast, and Inexpensive Synthesis of Monodisperse Amorphous Nickel-Phosphide Nanoparticles of Predefined Size. *Chem. Commun.* **2011**, *47*, 4108−4110.

(36) Zhang, H.; Ha, D.-H.; Hovden, R.; Kourkoutis, L. F.; Robinson, R. D. Controlled Synthesis of Uniform Cobalt Phosphide Hyperbranched Nanocrystals Using Tri-n-octylphosphine Oxide as a Phosphorus Source. *Nano Lett.* **2011**, *11*, 188−197.

(37) Perera, S. C.; Tsoi, G.; Wenger, L. E.; Brock, S. L. Synthesis of MnP Nanocrystals by Treatment of Metal Carbonyl Complexes with Phosphines: A New, Versatile Route to Nanoscale Transition Metal Phosphides. *J. Am. Chem. Soc.* **2003**, *125*, 13960–13961.

(38) Harris, D. K.; Bawendi, M. G. Improved Precursor Chemistry for the Synthesis of III−V Quantum Dots. *J. Am. Chem. Soc.* **2012**, *134*, 20211–20213.

(39) Joung, S.; Yoon, S.; Han, C.-S.; Kim, Y.; Jeong, S. Facile Synthesis of Uniform Large-Sized InP Nanocrystal Quantum Dots Using Tris(tertbutyldimethylsilyl)phosphine. *Nanoscale Res. Lett.* **2012**, *7*, 93.

(40) Yin, Y. D.; Erdonmez, C. K.; Cabot, A.; Hughes, S.; Alivisatos, A. P. Colloidal Synthesis of Hollow Cobalt Sulfide Nanocrystals. *Adv. Funct. Mater.* **2006**, *16*, 1389–1399.

(41) Chen, C. J.; Chiang, R. K. Sulfidation of Rock-Salt-Type Transition Metal Oxide Nanoparticles as an Example of a Solid State Reaction in Colloidal Nanoparticles. *Dalton Trans.* **2011**, *40*, 880−885.

(42) Park, J.; Zheng, H. M.; Jun, Y. W.; Alivisatos, A. P. Hetero-Epitaxial Anion Exchange Yields Single-Crystalline Hollow Nanoparticles. *J. Am. Chem. Soc.* **2009**, *131*, 13943–13945.

(43) Zhang, H.; Solomon, L. V.; Ha, D. H.; Honrao, S.; Hennig, R. G.; Robinson, R. D. $(NH_4)_2S$, a Highly Reactive Molecular Precursor for Low Temperature Anion Exchange Reactions in Nanoparticles. *Dalton Trans.* **2013**, *42*, 12596–12599.

(44) Qin, Z.; Sun, H.; Jiang, Z.; Jiao, X.; Chen, D. Synthesis of Metal Sulfide Nanoboxes Based on Kirkendall Effect and Pearson Hardness. *CrystEngComm* **2013**, *15*, 897–902.

(45) Sines, I. T.; Schaak, R. E. Phase-Selective Chemical Extraction of Selenium and Sulfur from Nanoscale Metal Chalcogenides: A General Strategy for Synthesis, Purification, and Phase Targeting. *J. Am. Chem. Soc.* **2011**, *133*, 1294−1297.

(46) Muthuswamy, E.; Brock, S., L. Oxidation Does Not (Always) Kill Reactivity of Transition Metals: Solution-Phase Conversion of Nanoscale Transition Metal Oxides to Phosphides and Sulfides. *J. Am. Chem. Soc.* **2010**, *132*, 15849–15851.

(47) Ha, D.-H.; Moreau, L. M.; Bealing, C. R.; Zhang, H.; Hennig, R. G.; Robinson, R. D. The Structural Evolution and Diffusion during the Chemical Transformation from Cobalt to Cobalt Phosphide Nanoparticles. *J. Mater. Chem.* **2011**, *21*, 11498−11510.

(48) Muthuswamy, E.; Brock, S. L. Solid-state Phase Transformations in Solution: Templated Conversion of Nanoscale Nickel Phosphides. *Chem. Commun.* **2011**, *47*, 12334–12336.

(49) Lukehart, C. M.; Milne, S. B.; Stock, S. R. Formation of Crystalline Nanoclusters of Fe_2P, RuP, Co_2P, Rh_2P, Ni_2P, Pd_5P_2, or PtP_2 in a Silica Xerogel Matrix from Single-Source Molecular Precursors. *Chem. Mater.* **1998**, *10*, 903−908.

(50) Savithra, G. H. L.; Bowker, R. H.; Carrillo, B. A.; Bussell, M. E.; Brock, S. L. Mesoporous Matrix Encapsulation for the Synthesis of Monodisperse Pd_5P_2 Nanoparticle Hydrodesulfurization Catalysts. *ACS Appl. Mater. Interfaces* **2013**, *5*, 5403–5407.

(51) Layan Savithra, G. H.; Bowker, R. H.; Carrillo, B. A.; Bussell, M. E.; Brock, S. L. Rational Design of Nickel Phosphide Hydrodesulfurization Catalysts: Controlling Particle Size and Preventing Sintering. *Chem. Mater.* **2013**, *25*, 825–833.

(52) Yang, Y.; Ochoa-Hernandez, C.; de la Peña O'Shea, V. A.; Coronado, J. M.; Serrano, D. P. Ni_2P/SBA-15 As a Hydrodeoxygenation Catalyst with Enhanced Selectivity for the Conversion of Methyl Oleate Into n-Octadecane. *ACS Catal.* **2012**, *2*, 592−598.

(53) Koranyi, T. I.; Vit, Z.; Poduval, D. G.; Ryoo, R.; Kim, H. S.; Hensen, E. J. M. SBA-15-Supported Nickel Phosphide Hydrotreating Catalysts. *J. Catal.* **2008**, *253*, 119–131.

(54) Wuts, P. G. M.; Greene, T. W. *Greene's Protective Groups in Organic Synthesis*, 4th ed.; John Wiley & Sons: New York, **2006**.

(55) Vela, J.; Smith, J. M.; Yu, Y.; Ketterer, N. A.; Flaschenriem, C. J.; Lachicotte, R. J.; Holland, P. L. Synthesis and Reactivity of Low-Coordinate Iron(II) Fluoride Complexes and Their Use in the Catalytic Hydrodefluorination of Fluorocarbons. *J. Am. Chem. Soc.* **2005**, *127*, 7857–7870

(56) Amii, H.; Uneyama, K. C-F Bond Activation in Organic Synthesis. *Chem. Rev.* **2009**, *109*, 2119–2183.

(57) Corey, J. Y. Reactions of Hydrosilanes with Transition Metal Complexes and Characterization of the Products. *Chem. Rev.* **2011**, *111*, 863–1071.

(58) Luo, Y.-R.; Cheng, J.-P. Bond Dissociation Energies. In *CRC Handbook of Chemistry and Physics*, 95th ed.; Haynes, W. M., Ed.; Taylor and Francis: Boca Raton, FL, **2014**; Internet Version, 9-65− 9-96.

(59) Wang, X.; Song, J.; Gao, L., Jin, J.; Zheng, H.; Zhang, Z. Optical and Electrochemical Properties of Nanosized NiO via Thermal Decomposition of Nickel Oxalate Nanofibres. *Nanotechnology* **2005**, *16*, 37−39.

(60) Nelson, N. C.; Ruberu, T. P. A.; Reichert, M. D.; Vela, J. Templated Synthesis and Chemical Behavior of Nickel Nanoparticles within High Aspect Ratio Silica Capsules. *J. Phys. Chem. C* **2013**, *117*, 25826−25836.

(61) Shim, J. H.; Nam, K. M.; Seo, W. S.; Song, H.; Park, J. T. The role of water for the phase-selective preparation of hexagonal and cubic cobalt oxide nanoparticles. *Chem. Asian J.* **2011**, *6*, 1575−1581.

(62) Luisetto, I.; Pepe, F.; Bemporad, E. Preparation and Characterization of Nano Cobalt Oxide. *J. Nanopart. Res.* **2008**, *10*, 59–67.

(63) Lin, C.-C.; Guo, Y.; Vela, J. Microstructure Effects on the Water Oxidation Activity of Co_3O_4/Porous Silica Nanocomposites. *ACS Catal.* **2015**, *5*, 1037−1044.

(64) Wang, W. S.; Dahl, M.; Yin, Y. D. Hollow Nanocrystals through the Nanoscale Kirkendall Effect. *Chem. Mater.* **2013**, *25*, 1179– 1189.

(65) Fan, H. J.; Knez, M; Scholz, R.; Hesse, D.; Nielsch, K.; Zacharias, M.; Gösele, U. Influence of Surface Diffusion on the Formation of Hollow Nanostructures Induced by the Kirkendall Effect: The Basic Concept. *Nano Lett.* **2007**, *7*, 993–997.

(66) Cabot, A.; Ibáñez, M.; Guardia, P.; Alivisatos, P. A. Reaction Regimes on the Synthesis of Hollow Particles by the Kirkendall Effect. *J. Am. Chem. Soc.* **2009**, *131*, 11326–11328.

(67) Yin, Y.; Riouz, R. M.; Erdonmez, C. K.; Hughes, S.; Somorjai, G. A.; Alivisatos, P. A. Formation of Hollow Nanocrystals Through the Nanoscale Kirkendall Effect. *Science* **2004**, *304*, 711–714.

(68) Dzugutov, M. A Universsal Scaling Law for Atomic Diffusion in Condensed Matter. *Nature* **1996**, *381*, 137−139.

(69) Reichert, M. D.; Lin, C.-C.; Vela, J. How Robust are Semiconductor Nanorods? Investigating the Stability and Chemical Decomposition Pathways of Photoactive Nanocrystals. *Chem. Mater.* **2014**, *26*, 3900–3908.

(70) Corey, J. Y. Reactions of Hydrosilanes with Transition Metal Complexes and Characterization of the Products. *Chem. Rev.* 2011, *111*, 863–1071.

(71) Rödl, C.; Fuchs, F.; Furthmüller, J.; Bechstedt, F. Quasiparticle Band Structures of the Antiferromagnetic Transition-Metal Oxides MnO, FeO, CoO, and NiO. *Phys. Rev. B* 2009, *79*, 235114-1–235114-8.

(72) Xu, R.; Zeng, H. C. Self-Generation of Tiered Surfactant Superstructures for One-Pot Synthesis of Co_3O_4 Nanocubes and Their Close and Non-Close-Packed Organizations. *Langmuir* 2004, *20*, 9780–9790.

(73) Cui, B.; Lin, H.; Liu, Y. Z.; Li, J. B.; Sun, P.; Zhao, X. C.; Liu, C. J. Photophysical and Photocatalytic Properties of Core-Ring Structured $NiCo_2O_4$ Nanoplatelets. *J. Phys. Chem. C* 2009, *113*, 14083–14087.

CHAPTER 4.

MULTISHELL Au/Ag/SiO_2 NANORODS WITH TUNABLE OPTICAL PROPERTIES AS SINGLE PARTICLE ORIENTATION AND ROTATIONAL TRACKING PROBES

Modified from a published paper on *Anal. Chem*. **2015**, *87*, 4096–4099.

Kuangcai Chen,[‡†] Chia-Cheng Lin,[‡¶] Javier Vela,[*] Ning Fang[*]

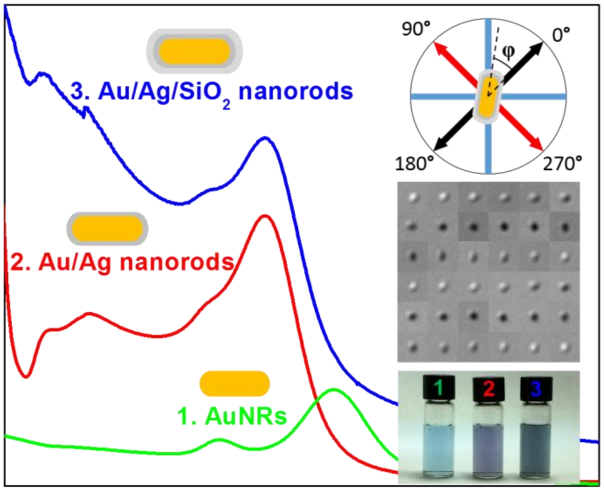

Abstract

We present the synthesis and exploitation of three-layer core-shell plasmonic nanorods (Au/Ag/SiO_2-NRs), which consist of a gold nanorod (AuNR) core, a thin silver shell and third thin silica layer, as optical imaging probes under a differential interference contrast (DIC) microscopes for single particle orientation and rotational tracking (SPORT). After the addition of the silver shell, the localized surface plasmon resonance (LSPR) modes were enhanced by a factor of three, compared to those of the bare gold nanorods, while the

---

[‡] Primary researcher and author
[†] Contributed to the SPORT experiments and data analysis
[¶] Contributed to the preparation and characterization of the Au/Ag/SiO_2 nanocomposites
[*] Author for correspondence

anisotropic optical properties of gold nanorods were maintained. The surrounding silica coating enables further surface modification with functional silanes through coupling reactions and provides enhanced colloidal stability and biocompatibility. Due to the longitudinal LSPR enhancement, the orientation and rotational information of the hybrid nanorods on synthetic lipid bilayers and live cell membranes was obtained with a temporal resolution in the millisecond range by using a scientific complementary metal-oxide-semiconductor (CMOS) camera under a DIC microscope. The preliminary results suggest that sensitivity improvement and good biocompatibility for SPORT experiments are achieved and these nanorod composites can serve as the imaging probes for further investigation in biological systems.

Introduction

Single particle tracking (SPT) is a powerful tool to study the dynamics of cellular and molecular processes, such as membrane dynamics,[1, 2] viral infection,[3] and intracellular transport.[4, 5] A large collection of imaging probes, including fluorescent molecules,[6, 7] quantum dots,[8, 9] and plasmonic nanocrystals,[5, 10-15] have been visualized with the aid of various optical microscopy techniques. While it has become a routine practice in SPT experiments to identify the trajectory of an imaging probe, it is more difficult to resolve the dipole orientation of the probe in real time, which may be essential in understanding the underlying biological functions. Recently, considerable efforts have been taken to overcome this challenge. Techniques such as fluorescence polarization microscopy,[6-8] dark field polarization scattering,[12] defocused orientation and position imaging,[9, 13] photothermal imaging,[14] correlation spectroscopy,[10, 11] total internal reflection scattering microscopy,[15, 16] and differential interference contrast (DIC) microscopy[17, 18] have been developed for *single particle orientation and rotational tracking*, which was coined as SPORT.[18, 19]

Gold nanorods (AuNRs) have been used extensively in SPORT experiments owing to their high photostability, good biocompatibility, and most importantly, anisotropic optical properties arising from their localized surface plasmon resonance (LSPR). Great success has been achieved on the AuNR synthesis using seed-mediated methods to fabricate a variety of AuNRs with different sizes, aspect ratios, and thus tunable extinction spectra across a wide spectral range.[20, 21] Compared with gold nanocrystals of similar size, silver nanocrystals exhibit stronger LSPR responses with more intense electric field enhancement and stronger absorption and scattering. However, the synthesis of anisotropic silver nanorods (AgNRs), especially for the smaller sizes (< 100 nm in length) that are better suited for biological studies, is more difficult than that of AuNRs in terms of size and shape uniformity control.[22, 23] Since silver shares the same face centered cubic crystal structure with gold and their lattice mismatch is as small as 0.27 %, AuNRs are suitable templates for epitaxial silver growth to form Au/Ag core-shell nanorods (Au/AgNRs).[24-29] The optical properties of Au/AgNRs can be finely tuned by controlling the aspect ratio of the AuNR cores and the amount of silver grown on the gold surface.[27] Moreover, the formation of Au/AgNRs induces multiple plasmonic bands that differ from single-component nanocrystals.

In view of the intrinsic cytotoxicity and instable nature of the silver shells in aqueous solution,[22, 30, 31] encapsulation of Au/AgNRs within a thin silica layer to form a three-layer core-shell nanorod structure, which will be referred to as Au/Ag/SiO_2-NR in this letter, can provide the necessary protection in biological imaging applications. The silica coating also improves the colloidal stability of Au/AgNRs, maintains the rod shape, and enables further surface functionalization with silane coupling agents for potential bioconjugation.[32, 33] Surface modification of the silica shell usually involves covalent attachment; therefore, this avoids cysteine residue replacement of thiol ligands as is often used in gold or silver surface functionalization.[34]

In the present study, Au/Ag/SiO_2-NRs were synthesized and tested for SPORT experiments. Millisecond/sub-millisecond temporal resolution was achieved in imaging the fast dynamics of Au/Ag/SiO_2-NRs rotating on synthetic lipid membranes and live cell membranes. To the best of our knowledge, this study demonstrates for the first time the development and application of hybrid core-shell nanorods as a new type of rotational probes.

Results and discussion

The core AuNRs used in the preparation of the Au/Ag/SO_2 nanocomposites were synthesized by following a modified seed-mediated growth method. In this seed-mediated method, the growth of the AuNRs took place when preformed gold nanocrystal seeds were rapidly injected to an aqueous growth solution consisting of cetyltrimethylammonium bromide (CTAB), chloroauric acid ($HAuCl_4$), silver nitrate ($AgNO_3$), and ascorbic acid ($C_6H_8O_6$), and the growth process took 24 hours.[20] Figure 1a shows a representative TEM image of as-synthesized AuNRs with an average diameter of 22.8 ± 3.2 nm, an average length of 52.6 ± 7.2 nm and an aspect ratio (defined as the ratio between length and diameter) of 2.3 ± 0.2. AuNRs typically have two distinct absorption peaks corresponding to the transverse LSPR (at shorter wavelengths) and longitudinal LSPR (at longer wavelengths). The longitudinal LSPR is related to the aspect ratio of the nanorods, i.e. longitudinal LSPR red-shifts as the aspect ratio increases, and *vice versa*. Figure 2 (black curve) reveals the absorption spectrum of the AuNRs, which consists of the transverse LSPR at 517 nm and the longitudinal LSPR at 632 nm.

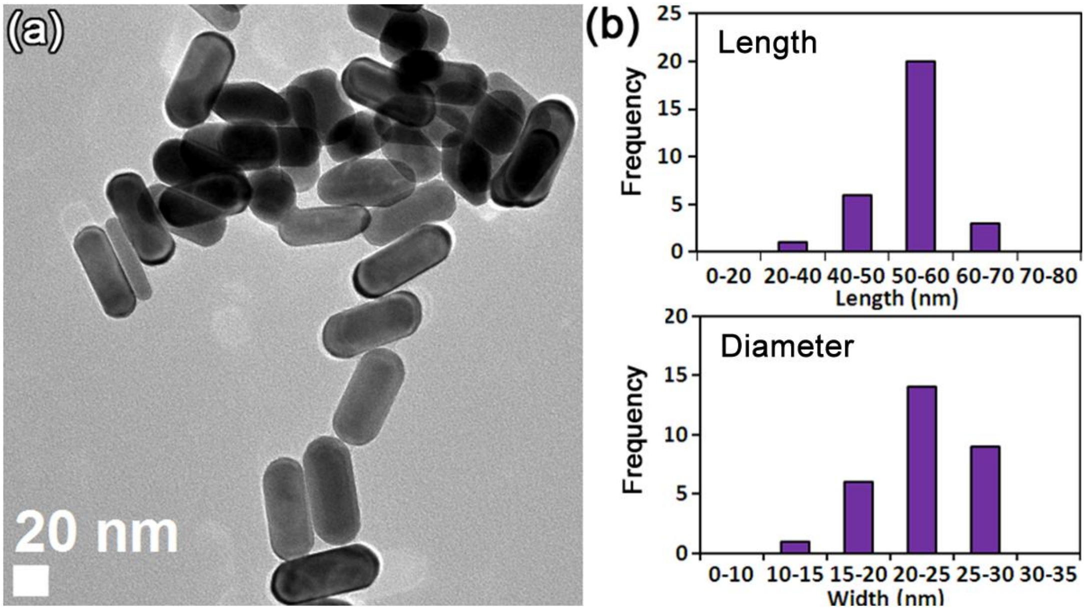

Figure 1. A representative TEM image of AuNRs (a) and histograms for size distribution (b).

Silver nanocrystals have a stronger LSPR phenomenon than that of gold nanocrystals, and the lattice mismatch between gold and silver is only 0.27 %. Taking advantage of the above two properties to obtain the LSPR enhancement, we thus performed the epitaxial deposition of silver layers on the surface of gold with a previously reported procedure with minor modification.[24] The as-synthesized AuNRs were separated from the solution to remove excess CTAB, followed by transfer into an aqueous solution containing polyvinylpyrrolidone (PVP), $AgNO_3$ and ascorbic acid. The silver growth process was triggered by the addition of $NaOH_{(aq)}$. Figure 2 shows the UV-Vis absorption spectra of the original AuNRs and several Au/AgNRs with different silver shell thicknesses. As the amount of silver increases, the longitudinal LSPR peaks blue-shift. The characteristic absorption feature of AuNRs also changes along with silver addition. Initially, the two concrete peaks correspond to the transverse and longitudinal LSPR of anisotropic AuNRs. When more silver was added, the two LSPR absorptions blue-shifted and became closer and eventually merged. The blue-shift and merge of the LSPR absorptions suggest the loss of the anisotropy and, eventually, the increased dominance of silver. Figure 2 also reveals that the working range of the AuAgNRs is tunable from 630 nm all the way to 400 nm. It is reported that the LSPR of silver spheres appears around 390 nm. TEM reveals the morphologies of AuAg574 and AuAg498 nanorods (Figure 3, the numbers represent the λ_{Max} of the longitudinal LSPR). The morphology of AuAg574 is maintained (cylindrical/ellipsoidal) while that of AuAg498 becomes more spherical, due to the preferential growth of silver along the lateral direction.

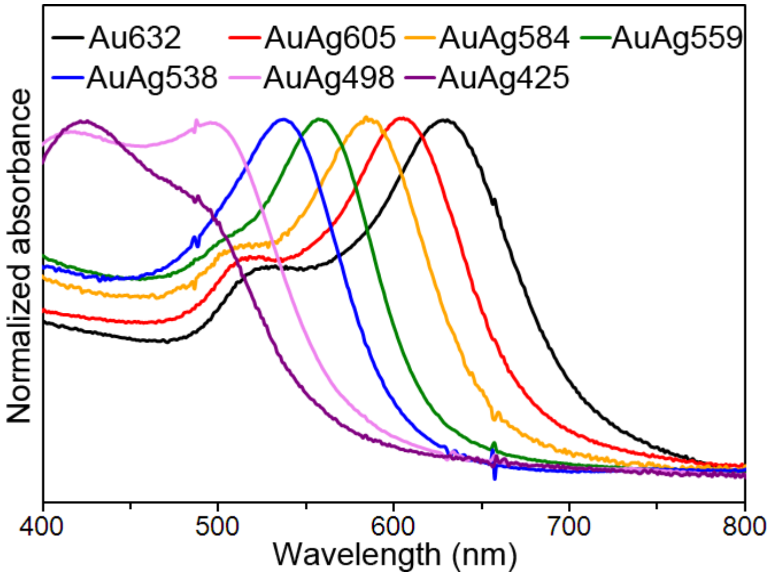

Figure 2. UV-Vis absorption spectra of AuNRs and Au/AgNRs with different silver shell thickness. The numbers indicate the longitudinal absorption peak postion.

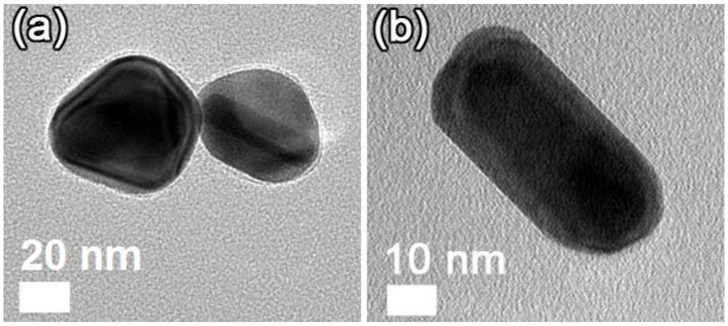

Figure 3. Representative TEM images of AuAg498 (a) and AuAg574 (b).

To further select suitable Au/AgNRs which have the appropriate LSPR modes, giving highest quantum yields in the optical window of the DIC instrument, we performed another series of syntheses of Au/AgNRs. Figure 4 illustrates the UV-Vis absorption spectra of AuNRs and Au/AgNRs with three different Ag/Au molar ratios of 0.11, 0.22, and 0.34. As the Ag/Au ratio increases, the silver shell becomes thicker and the longitudinal LSPR wavelength is blue-shifted from 632 nm to 575, 537, and 503 nm, respectively. As shown in Figure 4, the extinction coefficients of the Au/AgNRs increased as more Ag was added, which agrees with the assertion that Ag has high LSPR than Au. These plasmonic band blue-shifts can be used to estimate the Ag shell thickness, as well as to direct further syntheses.[26, 28, 29] The Au/AgNRs with the Ag/Au ratio of 0.11 maintain the cylindrical/ellipsoidal shape, and two extra plasmonic bands at 339 and 400 nm are believed to be the octupolar plasmonic modes while the peaks at 506 nm and 575 nm are correspond to the transverse and longitudinal dipolar plasmonic modes.[24-26] Since Au/AgNRs with higher Ag/Au ratios become irregular and spherical (though they have more intense LSPR modes), only the rod-shaped Au/AgNRs Ag/Au ratio of 0.11 were used to progress the following synthesis and imaging experiments.

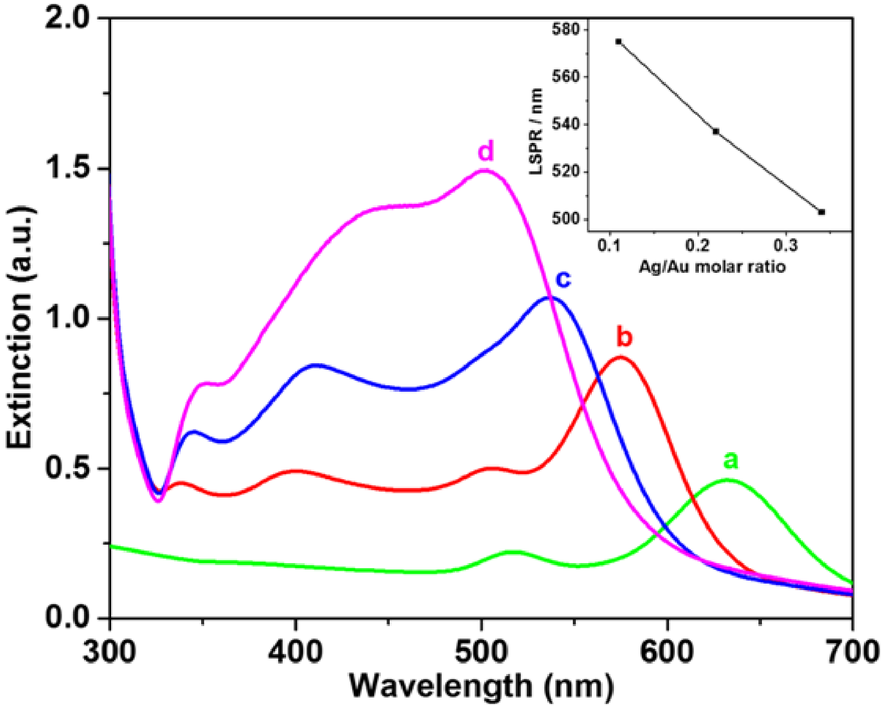

Figure 4. UV-Vis extinction spectra of synthesized nanoparticles. (a) AuNRs and the Au/Ag core-shell nanoparticles with Ag/Au molar ratios of (b) 0.11, (c) 0.22, (d) 0.34. As shown in the inserted figure, the longitudinal LSPR of AuNRs shifted from 632 nm to 575 nm, 537 nm and 503 nm after the addition of silver layer.

A solid silica layer was then deposited upon the AuAgNRs in order to improve the colloidal stability and biocompatibility because of the intrinsic toxicity of silver. To avoid incorporating CTAB into the silica layer, which will result in porosity, a two-step method was employed to complete the silica coating. Mercaptotrimethoxysilane (MPS) was used to replace the surface-attached CTAB, followed by the addition of sodium silicate as the silica source. Figure 5 shows the UV-Vis absorption spectra of AuNRs, Au/AgNRs, and Au/Ag/SiO_2-NRs, while the inset shows a representative TEM image of a core-shell Au/Ag/SiO_2 with dimensions of 64 nm × 46 nm. The preferential growth of Ag along the lateral direction over the tips leads to the reduction of aspect ratio. The aspect ratio reduction accompanying the addition of silver resulted in the blue-shift of the LSPR modes by 40 nm. Considering their relative extinction intensities, the longitudinal dipolar plasmonic mode increases by roughly a factor of 3 in Au/AgNRs compared to that of the original AuNRs and this enhanced LSPR absorption can reduced the required exposure time in SPOR experiments. The baseline in the UV-Vis absorption spectrum of the Au/Ag/SiO_2-NR solution is slightly elevated because of scattering caused by silica, as reported previously by others.[32] The LSPR λ_{Max} of the Au/Ag/SiO_2NRs slightly shifted due to the dielectric environment change.

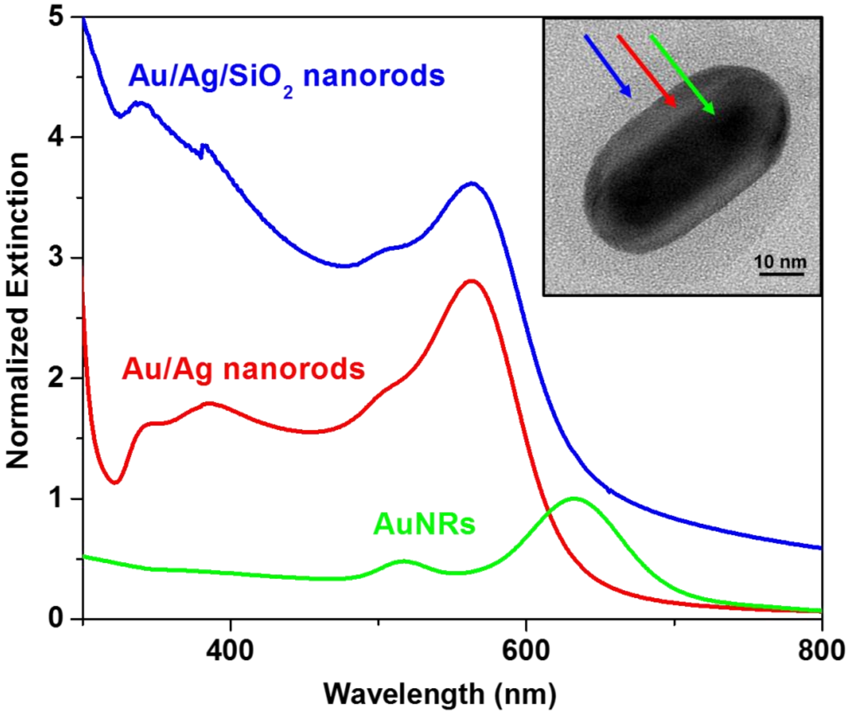

Figure 5. UV-Vis optical absorption spectra of AuNRs (green curve), Au/AgNRs (red curve) and Au/Ag/SiO_2-NRs (blue curve) in water. All the spectra are normalized to the absorbance of AuNRs at 632 nm while the concentrations are kept the same. The inset shows a representative TEM image of three-layered Au/Ag/SiO_2-NR.

Following the synthesis, the Au/Ag/SiO_2-NRs were imaged under a DIC microscope equipped with a Hamamatsu ORCA-Flash 2.8 scientific CMOS camera, which allows imaging at millisecond or sub-millisecond temporal resolution. In addition to the enhanced LSPR response from the silver coating, the blue-shift of the LSPR wavelength from 632 nm (AuNRs) to 563 nm (Au/Ag/SiO_2-NRs) provides another noticeable gain in the camera’s quantum efficiency and therefore sensitivity.

In the previous studies, the DIC contrasts, which are defined as the difference between the brightest and the darkest intensities divided by the average local background intensity, of nanoparticles showed wavelength dependence; the longitudinal LSPR was even more sensitive to the environment than the transverse LSPR.[17, 35] Here, the DIC contrast of an immobilized, randomly oriented Au/Ag/SiO_2-NR is plotted as a function of excitation wavelength (Figure 6). The highest DIC contrast for this particle appears when a 585 ± 29 nm filter was used for illumination, which agrees with the longitudinal dipolar plasmonic band.

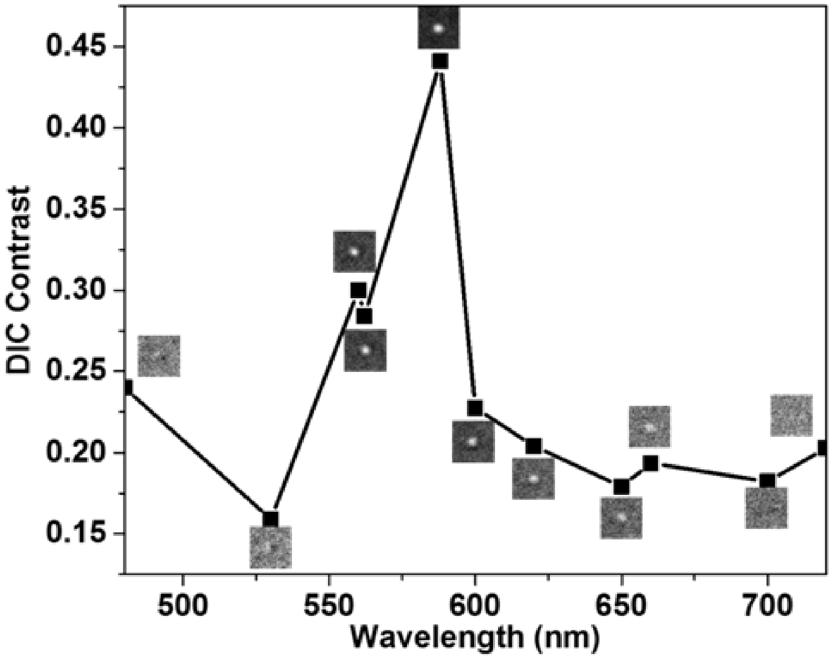

Figure 6. DIC contrast spectrum of an immobilized and randomly oriented Au/Ag/SiO_2-NR on a glass slide. Data points were determined by the availability of band pass filters. Each DIC image corresponding to the closest data point in the plot and the image contrast are normalized to their local maximum and minimum intensities. The edge length of each square is 1.45 µm.

DIC images of two immobilized Au/Ag/SiO_2-NRs on glass slides were recorded at different exposure times and stitched together to make Movie S1 in the Supporting Information, which is played at 30 frames per second (fps). These two particles in the movie were nearly perpendicular to each other as their DIC images showed the totally-bright and totally-dark patterns. During these measurements, the light source was kept at the maximum output power (100 Watts), and the overall intensity decreased linearly as expected when shorter exposure time was used (Figure 7). The relative bright and dark intensity measurement errors were increased from ~1% at 50 ms to ~5% at 0.5 ms for both nanorods

(Table 1). Because of the LSPR enhancement resulting from the silver coating, the core-shell hybrid nanorods were detectable at a temporal resolution as fast as 0.5 ms, which is about an order of magnitude faster than the previously reported fastest temporal resolution of 2 - 5 ms by AuNRs.[5, 18]

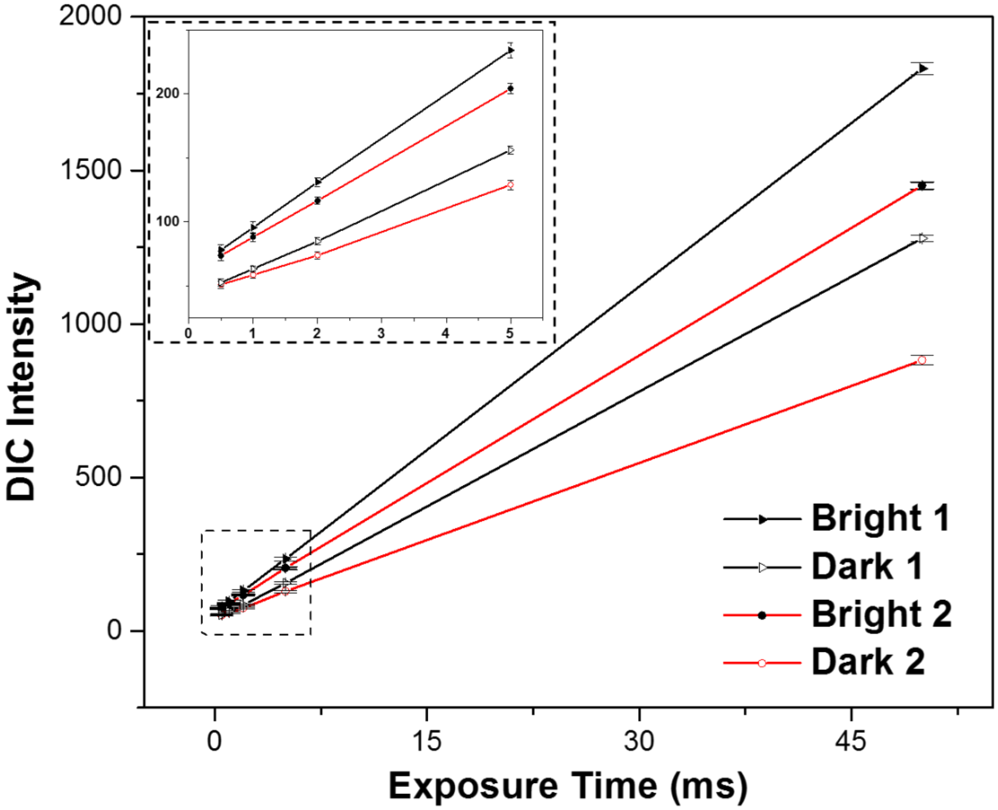

Figure 7. DIC intensity changes upon changing the exposure time. Bright 1 and Dark 1 correspond to the nanoparticle on the left in movie S1 and Bright 2 and Dark 2 are for the nanoparticle on the right. The inset shows the highlighted area on the low exposure part of the main plot.

Table 1. Relative bright and dark intensity measurement errors of the both Au/Ag/SiO_2-NRs in movie 1. Bright 1 and Dark 1 corresponding to the nanoparticle on the left in movie 1 and Bright 2 and Dark 2 are for the particle on the right.

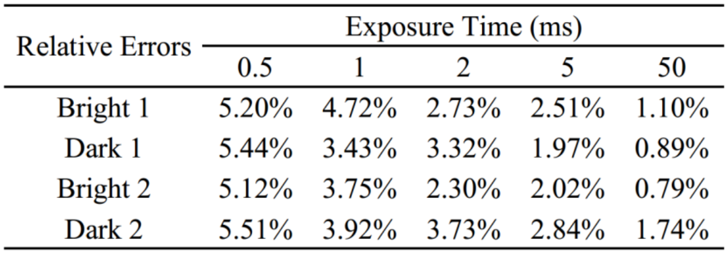

Relative Errors	Exposure Time (ms)				
	0.5	1	2	5	50
Bright 1	5.20%	4.72%	2.73%	2.51%	1.10%
Dark 1	5.44%	3.43%	3.32%	1.97%	0.89%
Bright 2	5.12%	3.75%	2.30%	2.02%	0.79%
Dark 2	5.51%	3.92%	3.73%	2.84%	1.74%

A 360° rotation study of the Au/Ag/SiO_2-NRs was performed by rotating the sample stage with 10° increments to position the nanorods in different orientations while exciting at the longitudinal LSPR wavelength of 563 nm. The orientation angle φ was defined as the angle between the long axis of the nanorod and the “bright” polarization direction of the DIC microscope (Figure 8). The “bright” polarization direction is named after the fact that a completely bright DIC image is obtained when the nanorod’s long axis aligns with this polarization direction ($\varphi = 0$), while the “dark” polarization direction corresponds to a completely dark DIC image. Figure 8 shows the complete rotation set of disproportionate bright and dark DIC image patterns. The DIC images change periodically as the nanorod long axis rotates against the polarization directions, which is in good agreement with the polarization-dependent rotation behaviors of plasmonic nanoparticles we have extensively investigated on gold nanorods and nanowires. In view of the periodic changes, an anti-correlation between the bright and dark intensity traces is observed: the intensity of the dark part decreases as the intensity of the bright part increases, and *vice versa*. This orientation/polarization dependence is the foundation for the use of Au/Ag/SiO_2-NRs as SPORT probes.

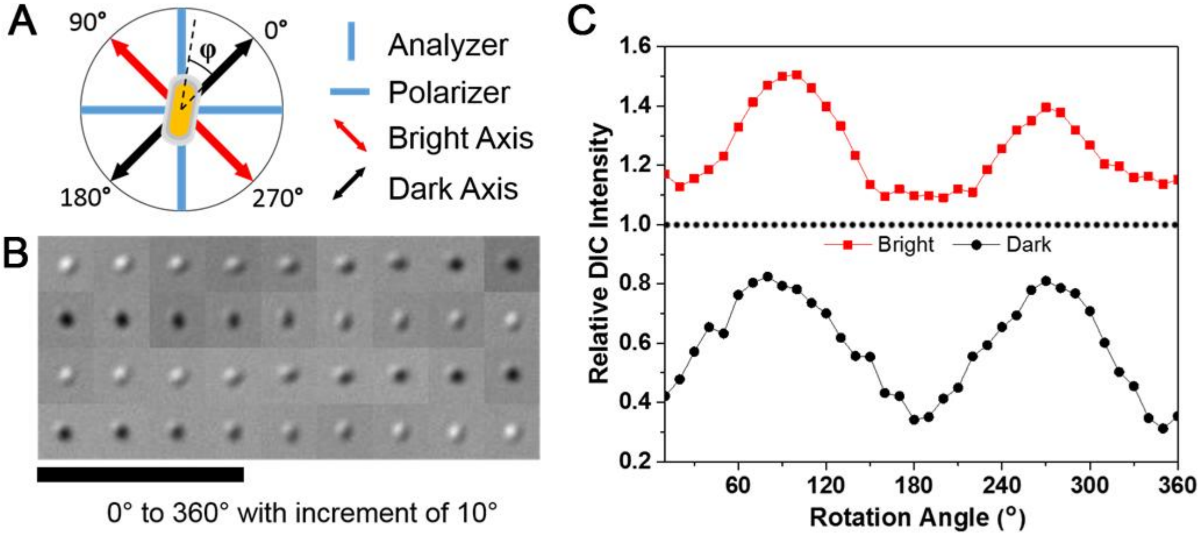

Figure 8. 360° rotation of Au/Ag/SiO_2-NR immobilized on a glass slide. (A) Definition of orientation angle φ with respect to the polarizer and analyzer positions in Nikon Eclipse 80i microscope setup. (B) 36 DIC images of Au/Ag/SiO_2-NR during 360° rotation from 0° to 360° with an interval of 10°. Scale represents 5 µm. (C) Relative DIC intensity traces of the bright and dark signals in (B).

Dynamic tracking of the Au/Ag/SiO_2-NRs was carried out on synthetic lipid bilayers. The nanorods were introduced onto the synthetic lipid bilayers in a chamber and bound to the membrane through non-specific interactions. Movies were recorded at a temporal resolution of 1 ms under 588 ± 29 nm illumination. Figure 9 shows the DIC intensity traces extracted from a representative 4-s (4000 frames) movie. The autocorrelation analysis of the DIC bright and dark traces[18] reveals that the nanorod's rotation speed fluctuates constantly. Representative examples of slow and fast rotation are given in Figure 2. The mean relaxation times of these two cases are 0.59 s (slow) and 0.024 s (fast).

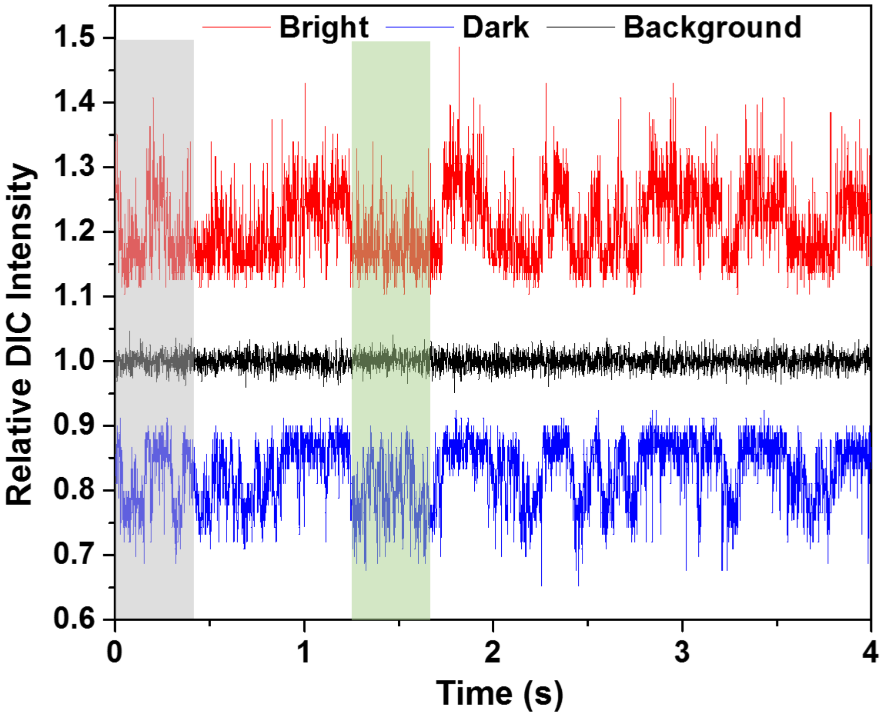

Figure 9. Relative DIC intensity traces of Au/Ag/SiO_2-NR rotating on synthetic lipid bilayer surface and recorded at 1 ms temporal resolution for 4000 frames.

In live cell experiments, A549 human lung cancer cells were used as a model system, which provided a dynamic surface for rotational studies. Despite the much more complex cellular environments, the wavelength dependent properties of these SPORT probes are easily distinguishable from other cellular features by using different band pass filters. Three band pass filters (480 ± 40 nm, 588 ± 29 nm, and 700 ± 13 nm) were used to identify the nanorods. As shown in Figure 10, using the 588 ± 29 nm filter, which covers the longitudinal LSPR band, results in a high-contrast DIC image of Au/Ag/SiO_2-NRs that is distinct from the background. With either 480 ± 40 nm or 700 ± 13 nm band pass filters, the Au/Ag/SiO_2-NRs disappear into the background due to the low contrast acquired at these wavelengths, which are far away from the LSPR bands.

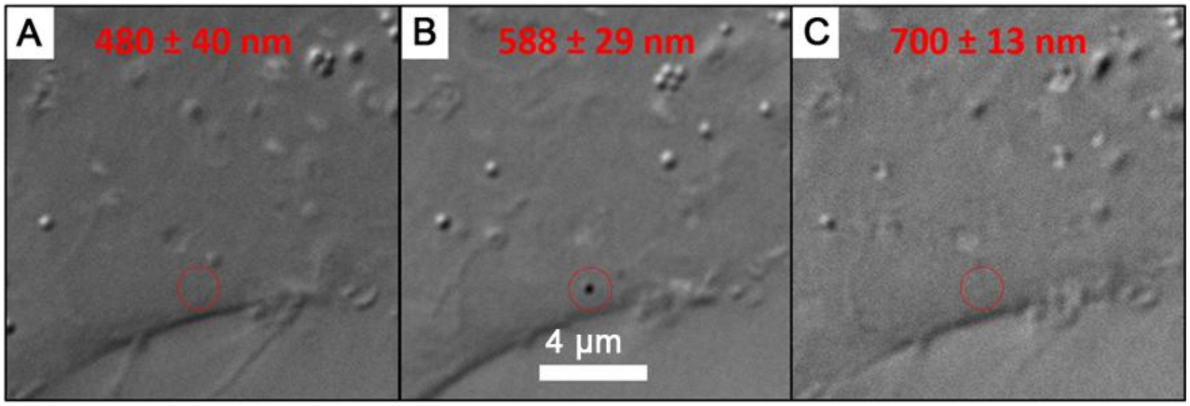

Figure 10. Differentiation of the Au/Ag/SiO_2-NRs (highlighted in the red circles) from other cellular features using three filters, (A) 480 ± 40 nm, (B) 588 ± 29 nm, and (C) 700 ± 13 nm. Scale bar is 4 µm. These images were taken sequentially. The nanorod and many cellular features changed their location and/or morphology during the imaging time.

In the live-cell imaging experiments, the Au/Ag/SiO_2-NRs were added into a chamber with A549 cells attached on the coverslip. Movies of the dynamic rotation of these nanorods were recorded at different exposure times of 1 ms, 5 ms, and 50 ms. The DIC intensity traces and the corresponding sets of consecutive DIC images were plotted in Figure 11. The autocorrelation analysis of the DIC bright and dark traces gives mean relaxation times of 11 ms at the temporal resolution of 1 ms, 23 ms at 5 ms, and 115 ms at 50 ms. Higher temporal resolution helps to unveil fast rotational dynamics, even though the overall intensity inevitably decreases as the single-frame exposure time decreases.

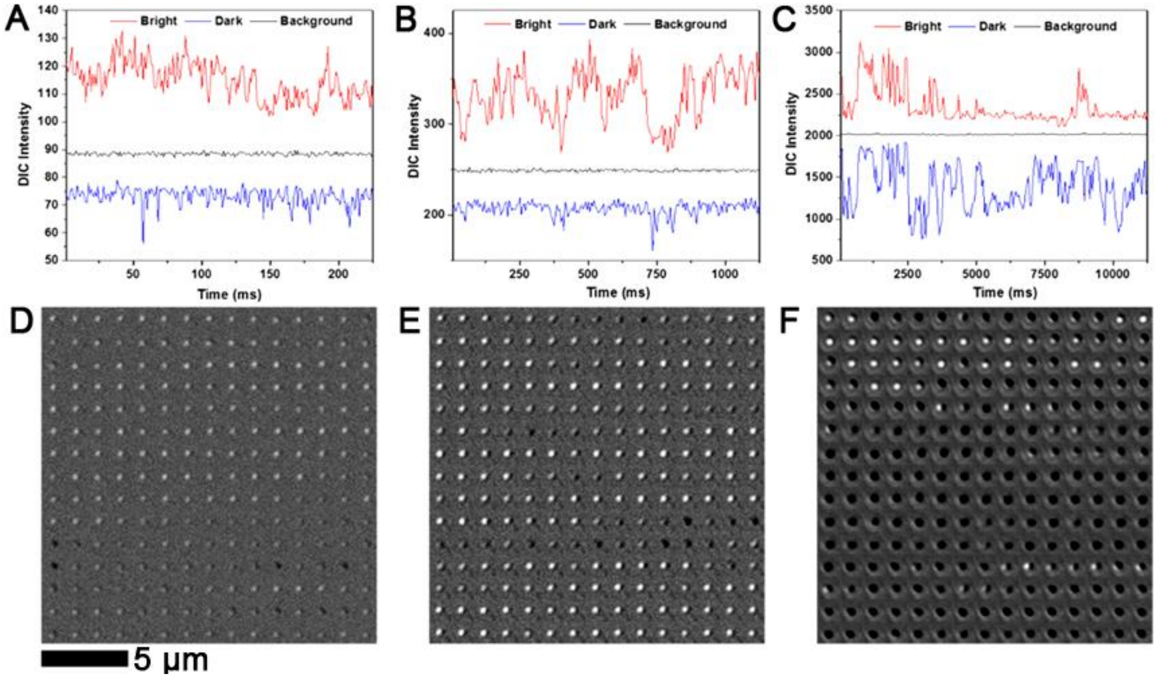

Figure 11. DIC intensity traces of Au/Ag/SiO_2-NRs rotating on cell membrane and recorded at (A) 1 ms, (B) 5 ms, and (C) 50 ms and their corresponding consecutive DIC images (D), (E) and (F). Scale bar is 5 µm.

Conclusions

In summary, we have successfully synthesized Au/Ag/SiO_2-NRs with well-controlled size and shape for SPORT. These optically anisotropic hybrid plasmonic nanorods exhibit orientation/polarization and wavelength dependent behavior in DIC microscopy. With the enhancement of the longitudinal dipolar LSPR after silver coating, these nanorods provide sufficient sensitivity for detection at millisecond temporal resolution on both synthetic lipid bilayers and live cell membranes. Surface modification of the silica layer of the hybrid nanorods will enable versatile applications in SPORT.

Experimental section

Synthesis

Nanorod Synthesis and Characterization. AuNRs were prepared according to a modified literature procedure.[21] The gold nanoparticle seeds were prepared first. Typically, 5 mL of 0.20 M CTAB (aq) (Sigma-Aldrich) was mixed with 50 µL of 0.02 M $HAuCl_4$ (aq) ($HAuCl_4 \cdot xH_2O$, 49 % Au, Strem Chemicals) followed by the addition of 0.3 mL of ice-cold 0.01 M $NaBH_4$ (aq) (Acros Organics). The seed solution was kept stirring for 2 h prior to injection to the growth solution. The growth solution was prepared by mixing 50 mL of 0.10 M CTAB (aq), 1.25 mL of 0.02 M of $HAuCl_4$ (aq), 0.32 mL of 0.01 M $AgNO_3$ (aq) (Strem Chemicals) and 0.36 mL of 0.10 M ascorbic acid (ACS grade, Alfa Aesar) aqueous solution in a sequential order. After the growth solution turned colorless, 60 µL of the seed solution was injected into the growth solution and kept static for 24 h at 30 ℃. The silver-coated AuNRs were prepared according to a reported method.[25, 36] 4 mL of the gold nanorod solution was centrifuged and re-dispersed in 0.8 mL of 0.10 M CTAB followed by dilution to 4 mL with 1 wt % polyvinylpyrrolidone (PVP, M.W. 3,500, Acros Organics) aqueous solution. 24 µL of 0.01 M $AgNO_3$ (aq), 0.30 mL of 0.10 M ascorbic acid (aq) and 0.45 mL of 0.1 M NaOH (aq) (Fisher Scientific) were added in order and reacted for 2 h. For the thin silica coating, a reported two-step silica coating method was employed.[34] To a 2 mL of silver-coated gold nanorod solution, 20 µL of 2 v/v % ethanolic 3-mercaptopropyltrimethoxysilane (MPS) (Gelest) solution was added, and the mixture was kept stirring for 45 min. 40 µL of 0.54 % sodium silicate ($Na_2O(SiO_2)_x \cdot xH_2O$, 27 %, Sigma-Aldrich) solution was then added, and the solution was kept stirring for 4 days. Excess reactants were separated by centrifugation, and the silica-coated nanorods were re-dispersed in deionized water for further use.

Characterization

Transmission Electron Microscopy (TEM) was measured on an FEI Tecnai G2 F20 field emission scanning transmission electron microscope (S/TEM) at 200 kV (point-to-point resolution < 0.25 nm, line-to-line resolution < 0.10 nm). UV-Vis extinction spectra were collected with a photodiode-array Agilent 8453 UV−Vis spectrophotometer.

Synthetic Lipid Bilayer Preparation and Cell Cultures.

The phospholipid 1-palmitoyl-2-oleoyl-sn-glycero-3-phosphocholine (POPC, Avanti Polar Lipids) solution in chloroform was gently dried by nitrogen and vacuum drying at least 3 h at room temperature to remove the residual chloroform and stored in a -20 ℃ freezer. The final POPC concentration was brought to 0.5 mg/mL by adding appropriate amount of phosphate buffered saline (1x PBS, pH 7.4). After rehydrating in PBS for 30 min with vortexing, cloudy multilamellar vesicles suspension solution was obtained. The suspension solution was extruded through a polycarbonate membrane (100 nm pore size) at least 21 times to form the large unilamellar vesicles solution by a mini-extruder (Avanti Polar Lipids, Alabaster, AL). The resulted solution was kept in a 4℃ fridge.After incubating the unilamellar vesicle solution in a chamber, made by a cleaned glass slide, two double-sided tapes and a clean coverslip, for 10 min, the planar bilayer was formed. Then, the excess lipids were removed from the chamber by using PBS.

A549 human lung cancer cells (ATCC, CCL-185) were cultured on 22 mm × 22 mm glass coverslips in Petri dishes with F-12K Medium (Kaighn's Modification of Ham's F-12 Medium, ATCC, 30-2004) supplemented with 10 % fetal bovine serum. The cell culture was incubated at 37°C under 5% CO_2 to an appropriate confluence. Before imaging, the coverslip with cells was rinsed with 10 mM phosphate buffered saline (PBS) at pH 7.4 and put on a chamber made by two pieces of double-sided tape.

Imaging System.

An upright Nikon Eclipse 80i microscope was used in this study. The DIC mode used a pair of 100×II-R Nomarski prisms, a 100× Plan Apo/1.40 oil-immersion objective, a NA 1.40 oil condenser and a halogen lamp as light source with maximum output power of 100 Watts. Appropriate filters were inserted in the light path. In order to facilitate single particle characterization and to minimize inter-particle SPR coupling, the concentration of nanoparticles on the glass surface was controlled to an appropriate scope. The images and movies were taken by a Hamamatsu ORCA-Flash 2.8 CMOS camera and analyzed using MATLAB and NIH ImageJ.

Supporting information

For the movie S1, please go to http://pubs.acs.org/doi/suppl/10.1021/acs.analchem.5b00604.

Acknowledgement

The authors thank Michelle Thompson for assistance.

References

(1) Saxton, M. J.; Jacobson, K. *Annu. Rev. Biophys. Biomol. Struct.* **1997**, *26*, 373–399.

(2) Fujiwara, T.; Ritchie, K.; Murakoshi, H.; Jacobson, K.; Kusumi, A. *J. Cell Biol.* **2002**, *157*, 1071–1081.

(3) Lakadamyali, M.; Rust, M. J.; Babcock, H. P.; Zhuang, X. *Proc. Natl. Acad. Sci. USA* **2003**, *100*, 9280–9285.

(4) Yezhelyev, M. V.; Qi, L.; O'Regan, R. M.; Nie, S.; Gao, X. *J. Am. Chem. Soc.* **2008**, *130*, 9006–9012.

(5) Gu, Y.; Sun, W.; Wang, G.; Jeftinija, K.; Jeftinija, S.; Fang, N. *Nat. Commun.* **2012**, *3*, 1030.

(6) Greeson, J. N.; Raphael, R. M. *J. Biomed. Opt.* **2007**, *12*, 021002-021002–9.

(7) Beausang, J. F.; Sun, Y.; Quinlan, M. E.; Forkey, J. N.; Goldman, Y. E. *Cold Spring Harb. Protoc.* **2012**, *2012*, 535–545.

(8) Chung, I.; Shimizu, K. T.; Bawendi, M. G. *Proc. Natl. Acad. Sci. USA* **2003**, *100*, 405–408.

(9) Toprak, E.; Enderlein, J.; Syed, S.; McKinney, S. A.; Petschek, R. G.; Ha, T.; Goldman, Y. E.; Selvin, P. R. *Proc. Natl. Acad. Sci. USA* **2006**, *103*, 6495–6499.

(10) Sönnichsen, C.; Alivisatos, A. P. *Nano Lett.* **2004**, *5*, 301–304.

(11) Chang, W.-S.; Ha, J. W.; Slaughter, L. S.; Link, S. *Proc. Natl. Acad. Sci. USA* **2010**, *107*, 2781–2786.

(12) Tcherniak, A.; Dominguez-Medina, S.; Chang, W.-S.; Swanglap, P.; Slaughter, L. S.; Landes, C. F.; Link, S. *J. Phys. Chem. C* **2011**, *115*, 15938–15949.

(13) Li, T.; Li, Q.; Xu, Y.; Chen, X. J.; Dai, Q. F.; Liu, H.; Lan, S.; Tie, S.; Wu, L. J. *ACS Nano* **2012**, *6*, 1268–77.

(14) Zhang, B.; Lan, T.; Huang, X.; Dong, C.; Ren, J. *Anal. Chem.* **2013**, *85*, 9433–9438.

(15) Marchuk, K.; Ha, J. W.; Fang, N. *Nano Lett.* **2013**, *13*, 1245–1250.

(16) Stender, A. S.; Marchuk, K.; Liu, C.; Sander, S.; Meyer, M. W.; Smith, E. A.; Neupane, B.; Wang, G.; Li, J.; Cheng, J.-X.; Huang, B.; Fang, N. *Chem. Rev.* **2013**, *113*, 2469–2527.

(17) Ha, J. W.; Marchuk, K.; Fang, N. *Nano Lett.* **2012**, *12*, 4282–4288.

(18) Wang, G.; Sun, W.; Luo, Y.; Fang, N. *J. Am. Chem. Soc.* **2010**, *132*, 16417–16422.

(19) Gu, Y.; Sun, W.; Wang, G.; Fang, N. *J. Am. Chem. Soc.* **2011**, *133*, 5720–5723.

(20) Gu, Y.; Ha, J. W.; Augspurger, A. E.; Chen, K.; Zhu, S.; Fang, N. *Nanoscale* **2013**, *5*, 10753–10764.

(21) Nikoobakht, B.; El-Sayed, M. A. *Chem. Mater.* **2003**, *15*, 1957–1962.

(22) Gole, A.; Murphy, C. J. *Chem. Mater.* **2004**, *16*, 3633–3640.

(23) Jana, N. R.; Gearheart, L.; Murphy, C. J. *Chem. Commun.* **2001**, 617–618.

(24) Pietrobon, B.; McEachran, M.; Kitaev, V. *ACS Nano* **2008**, *3*, 21–26.

(25) Liu, M.; Guyot-Sionnest, P. *J. Phys. Chem. B* **2004**, *108*, 5882–5888.

(26) Xiang, Y.; Wu, X.; Liu, D.; Li, Z.; Chu, W.; Feng, L.; Zhang, K.; Zhou, W.; Xie, S. *Langmuir* **2008**, *24*, 3465–3470.

(27) Park, K.; Drummy, L. F.; Vaia, R. A. *J. Mater. Chem.* **2011**, *21*, 15608–15618.

(28) Jiang, R.; Chen, H.; Shao, L.; Li, Q.; Wang, J. *Adv. Mater.* **2012**, *24*, OP200–OP207.

(29) Hou, S.; Hu, X.; Wen, T.; Liu, W.; Wu, X. *Adv. Mater.* **2013**, *25*, 3857–3862.

(30) Zhu, J.; Zhang, F.; Li, J.-J.; Zhao, J.-W. *Gold Bull.* **2014**, *47*, 47–55.

(31) Damm, C.; Segets, D.; Yang, G.; Vieweg, B. F.; Spiecker, E.; Peukert, W. *Small* **2011**, *7*, 147–156.

(32) Cheng, X.; Zhang, W.; Ji, Y.; Meng, J.; Guo, H.; Liu, J.; Wu, X.; Xu, H. *RSC Adv.* **2013**, *3*, 2296–2305.

(33) Kobayashi, Y.; Katakami, H.; Mine, E.; Nagao, D.; Konno, M.; Liz-Marzán, L. M. *J. Colloid Interface Sci.* **2005**, *283*, 392–396.

(34) Sendroiu, I. E.; Warner, M. E.; Corn, R. M. *Langmuir* **2009**, *25*, 11282–11284.

(35) Aryal, S.; B.K.C, R.; Dharmaraj, N.; Bhattarai, N.; Kim, C. H.; Kim, H. Y. *Spectrochim. Acta A Mol. Biomol. Spectrosc.* **2006**, *63*, 160–163.

(36) Khalavka, Y.; Becker, J.; Sonnichsen, C. *J. Am. Chem. Soc.* **2009**, *131*, 1871–1875.

(37) Ha, J. W.; Sun, W.; Stender, A. S.; Fang, N. *J. Phys. Chem. C.* **2012**, *116*, 2766–2771.

(38) Ha, J. W.; Chen, K.; Fang, N. *Chem. Commun.* **2013**, *49*, 11038–11040.

CHAPTER 5.

GENERAL CONCLUSIONS

We have synthesized several Co_3O_4/porous silica nanocomposites to study the synergetic effects of the catalyst microstructure and local environment on water oxidation catalytic activity. The NMR relaxation measurements of two different probe molecules (EG and Poly600) confirmed the pore accessibility of Co_3O_4/porous-SiO_2 nanoparticles with different shell thicknesses.

The catalytic activity study of Co_3O_4/porous SiO_2 core/shell nanoparticles on oxygen evolution reaction reveals that the catalyst with a 19.8 ± 1.4 nm shell had superior activity than other catalysts likely due to two possible factors: the increased local concentration of $Ru(bpy)_3^{2+}$ near the active Co_3O_4 and/or the reduced reorganization energy due to the lower dielectric constant. However, further increasing shell thicknesses resulted in the deterioration of catalytic activity possibly owing to slower diffusion of reactants.

Among the Co_3O_4/SBA-15 particles, the unmodified sample is more active than the modified ones. This could be due to local surface permittivities of surface-modified composites (e.g., $-SiPh$ and $-SiMe_3$) being lower than those of the unmodified composites. In addition, the loss of possible $Ru(bpy)_3^{2+}$ binding sites and pore blocking after surface modification may cause the loss of reactivity.

A more thorough understanding of the effects of microstructure and permittivity on water oxidation ability will enable the construction of next generation catalysts possessing optimal configuration and better efficiency for water oxidation and water splitting. Also, we can extend the scope of the NMR relaxation measurement: the porous structure can serve as a good size sorting sieve, the relaxation time difference can be a good indication to distinguish multi-component mixture, and further surface modification can enable more specific interaction .

Late transition metal chalcogenides and pnictides are interesting materials because of their unique physical properties and various applications, such as oil-upgrading and hydrogen evolution catalysts. Other than conventional synthetic methods, we have demonstrated a generalized method using trimethylsilyl reagents (TMS_xE) to transform metal oxides (Co_3O_4, CoO, NiO and $NiCo_2O_4$) into metal chalcogenides and pnictides, i.e. Co_9S_8, Co_3Se_4, CoP, Co_2P, Ni_3S_2, NiSe and Ni_2P. The resulting nanocrystals are hollow (vesicle-like) and are surrounded by amorphous silica layers. The nonequivalent diffusion of ions induced the void formation inside the nanocrystals (nanoscale Kirkendall effect); simultaneous decomposition of the TMS_xE produced silica layers serving as protection layers, preventing particle agglomeration and thus increasing both the robustness and thermal stability of the composites. We have also verified the feasibility of the deoxysilylation reaction of metal oxides even with a pre-formed silica layer.

We hypothesize that among the concurrent reactions of the deoxysilylation of Co_3O_4, the impure/intermediate CoO phase originated from the structure rearrangement Co(II) in Co_3O_4 based on the varied temperature experiments and the deoxysilylation of $NiCo_2O_4$. The successful deoxysilylation of the ternary metal oxide ($NiCo_2O_4$) with TMS_2S yielded Co-rich $(Co, Ni)_9S_8$, although the exact phase is not completely resolved.

Solid state ^{29}Si NMR data also show that silica (SiO_2) species are present after the reaction. Surface area and porosity analysis show deteriorated results, which might result from both the increase in the silica content (non-porous) and the mass contribution from residual organic ligands. In the synthetic perspective, one can adapt this method to prepare various transition metal chalcogenides and pnictides and extend it to work with other TMS_x precursors; this can also apply to other ternary metal systems. One can also utilize these high surface area nanocomposites to catalysis and electrochemical applications.

SPORT is one of the single particle tracking techniques that can elucidate the biophysics in biological systems. We have demonstrated the successful fabrication of $Au/Ag/SiO_2$ nanorods with well-controlled size, composition and shape for SPORT study. The epitaxial deposition of silver layer on gold and the sequential silica coating led to the formation of uniform and anisotropic hybrid nanorods possessing unique optical properties, i.e. the orientation/polarization and wavelength dependent behaviors, in a DIC microscopy. Also, with the enhancement of the longitudinal dipolar LSPR due to the secondary silver coating, these nanorods are able to provide sufficient sensitivity for detection at temporal resolution in millisecond range on both synthetic lipid bilayers and live cell membranes. The preliminary results reveal the $AuAgSiO_2$ nanorods are promising SPORT probes. The flexibility of tuning the LSPR positions can avoid either instrumental limitations or narrow optical windows in biological system. Further surface modification enable the versatile prospect applications targeting more specific interactions in biological systems with SPORT, and coupling the nanorods with other fluorophores allows to provide multiple information at once.